VILNIUS UNIVERSITY
CENTER FOR PHYSICAL SCIENCES AND TECHNOLOGY

SKIRMANTĖ BUTKUTĖ

SYNTHESIS AND CHARACTERIZATION OF NOVEL LUMINESCENT MATERIALS: TYPICAL OXIDE PHOSPHORS AND POSSIBLE INERT HOST LATTICES

Doctoral dissertation
Physical sciences, chemistry (03 P)

Vilnius, 2018

The dissertation was carried out from 2012 to 2016 at Vilnius University.

Scientific supervisors:

Prof. Dr. Aldona Beganskienė

Vilnius University, Physical Sciences, Chemistry - 03 P

(From 2012-10-01 to 2015-05-11)

Prof. Habil. Dr. Aivaras Kareiva

Vilnius University, Physical Sciences, Chemistry - 03 P

(From 2015-05-12 to 2016-09-30)

VILNIAUS UNIVERSITETAS
FIZINIŲ IR TECHNOLOGIJOS MOKSLŲ CENTRAS

SKIRMANTĖ BUTKUTĖ

NAUJŲ LIUMINESCENCINIŲ MEDŽIAGŲ SINTEZĖ IR APIBŪDINIMAS: TIPINIAI OKSIDINIAI FOSFORAI IR GALIMOS INERTINĖS MATRICOS

Daktaro disertacija
Fiziniai mokslai, Chemija (03 P)

Vilnius, 2018

Disertacija parengta 2012-2016 metais Vilniaus universitete.

Moksliniai vadovai:

Prof. dr. Aldona Beganskienė

Vilniaus universitetas, fiziniai mokslai, chemija - 03 P

(Nuo 2012-10-01 iki 2015-05-11)

Prof. habil. dr. Aivaras Kareiva

Vilniaus universitetas, fiziniai mokslai, chemija - 03 P

(Nuo 2015-05-12 iki 2016-09-30)

Contents

LIST OF ABBREVIATIONS

a.u.	Arbitrary units
DTA	Differential Thermal analysis
EDX	Energy-Dispersive X-Ray Spectroscopy
FTIR	Furier Transform Infra-Red Spectroscopy
FWHM	Full Width at Half Maximum
ICDD	The International Centre for Diffraction Data
ICP-OES	Inductively Coupled Plasma Optical Emission Spectrometry
IR	Infra-Red (part of light spectrum)
LED	Light Emitting Diode
NIR	Near Infra-Red (part of light spectrum)
PL	Photoluminescence
QE	Quantum Efficiency (of internal Photoluminescence)
SEM	Scanning Electron Microscopy
TG	Thermogravimetry
TRIS	Tris-(hydroxymethyl)-aminomethane
TSFZM	Travelling Solvent Floating Zone Method
XRD	X-Ray Diffractomety

INTRODUCTION

The discovery of new materials and subsequent optimization of their synthesis and envisage a prospect of their properties remains an important step in developing new important technologies. Materials science is well known for being one of the most interdisciplinary science that has led to many exciting discoveries, new materials and new applications. During the past years a rapid development of multicomponent metal-oxide ceramic materials, which are produced from fine-grained synthetic powders, has to a large extent revolutionized both concepts and technology in functional ceramics [1-5]. Multicomponent metal oxides exhibit a variety of outstanding physical and chemical properties, which include electric, magnetic, optical, mechanical, catalytic, and many other different functionalities. In recent years there has been a great deal of interest in the use of molecular species as precursors for the formation of multicomponent metal oxide powders with carefully controlled morphology and composition [6-9]. The specific luminescence, magnetic and electrical properties of multinary oxides are highly sensitive to changes in dopant composition, host stoichiometry, and processing conditions [10]. The sol-gel processing route is a way of manipulating molecular precursors to form bulk oxide materials [11].

Luminescence is a subject that continues to play a major technological role for humankind. Garnets, despite the real or potential industrial applications, mainly are used as phosphor materials employed in solid state lasers or light-emitting diodes [12-19]. Another very efficient phosphor matrix, listed as promising by G. Blasse [20] in 1968, is merwinite structure. While some optical properties have been reported of merwinites, $M_3MgSi_2O_8$, but not much is known about the structural, magnetic and electronic properties of these compounds yet. Structure-property relationships have always been fundamentally important to materials science and engineering [21, 22].

In this doctoral thesis the sol-gel chemistry approach was developed to the mixed-metal garnets containing gallium in tetrahedral and octahedral

positions of garnet crystal structure. The novel compositions of $M_3A_2Ga_3O_{12}$ ($M = Gd^{3+}$, Y^{3+}, Lu^{3+}; $A = Sc^{3+}$, Ga^{3+}) were successfully fabricated using the sol-gel combustion processing. Moreover, these sol-gel derived garnets were doped with Fe^{3+}, Ce^{3+}, Ce^{3+}/Cr^{3+} and Cr^{3+} to develop new phosphors. The attempts to synthesize mixed-metal silicates $Ca_3Mg(SiO_4)_2$ and new $Ba_3Cu(SiO_4)_2$ using this economical and environmentally friendly synthesis processing were also done in this doctoral dissertation.

Thus, this PhD work is devoted to the development of materials with two different crystal structures for optical and optoelectronic applications. This work has two main aims: to synthesize mixed-metal gallium garnets by sol-gel combustion method to meet the requirement of phosphor emitting light in far-red region and to investigate the preparation conditions for the first time for mixed barium copper silicate as inert matrix for light technologies. In order to achieve these aims the following tasks were set:

- To investigate the preparation conditions for mixed-metal $M_3A_2Ga_3O_{12}$ ($M = Gd^{3+}$, Y^{3+}, Lu^{3+}; $A = Sc^{3+}$, Ga^{3+}) garnets by sol-gel combustion method.
- To investigate the doping effects of luminescent centres (Fe^{3+}, Ce^{3+}, Ce^{3+}/Cr^{3+} and Cr^{3+}) on $Gd_3Ga_5O_{12}$ structural and photoluminescent properties.
- To investigate the preparation conditions and optical potential of Cr^{3+} doped mixed-metal garnets as new generation materials for light technologies.
- To investigate $Ca_3Mg(SiO_4)_2$ focusing on effective synthesis processing, the structural and morphological characterization.
- To investigate the preparation conditions and optimum synthesis parameters for the fabrication of new $Ba_3Cu(SiO_4)_2$ compound.

1. LITERATURE OBSERVATION

1.1. Garnet Structure Compounds

Garnets are a chemically diverse group of minerals that are abundant in the Earth's crust and upper mantle [23]. While for many years the garnet structure, originally solved by G. Menzer [24], has been important to the mineralogist, for the physicist, chemists and material scientists the interest appeared much later and it is important till now. In the past the greatest importance to the physicist was in the existence of the ferrimagnetic garnets [25]. Gallium garnets, same like one of the most famous garnet - yttrium aluminium garnet ($Y_3Al_5O_{12}$, YAG), have many properties that are desirable for a laser host matrix [26-28]. YAG is the most important solid-state laser host material, which has been widely used in the areas of industry and medicine since its discovery in 1964 [27]. Besides the ideal spectroscopic properties and good optical properties (high-optical transparency, low-acoustic loss, high threshold for optical damage) of the garnets, they show also good mechanical properties (hardness and general stability against mechanical changes), low-thermal expansion, high thermal conductivity and high chemical stability [26, 27, 29-31]. These excellent properties mostly are dependent on the unique crystal structure of garnets.

1.1.1. Crystal Structure of Garnets

The general formula for the garnet supergroup minerals is $\{X_3\}[Y_2](Z_3)\varphi_{12}$, where X, Y, and Z refer to metal ions in dodecahedral, octahedral, and tetrahedral sites, respectively, and φ is anionic site with O, OH, or F [32] (see Table 1). The most of garnet structure materials belongs to the $Ia\bar{3}d$ space group, no. 230, however two groups of natural garnet minerals, i.e. OH-bearing species (henritermierite and holtstamite), have tetragonal symmetry, space group $I4_1/acd$ (no. 142) [25, 33-35]. With few exceptions, the natural garnets are compositionally complex multicomponent solid solutions [35].

Table 1. A classification of the 32 approved species in the garnet supergroup [32].

Z charge	GROUP or species name	Class	X	Y	Z	φ
0	Katoite	Hydroxide	Ca_3	Al_2	[]	$(OH)_{12}$
3	Cryolithionite	Halide	Na_3	Al_2	Li_3	F_{12}
6	Yafsoanite	Oxide	Ca_3	Te_2^{6+}	Zn_3	O_{12}
8	HENRITERMIERITE	Silicate				
	Holtstamite		Ca_3	Al_2	$Si_2 \mid []$	$O_8(OH)_4$
	Henritermierite		Ca_3	Mn_2^{3+}	$Si_2 \mid []$	$O_8(OH)_4$
9	BITIKLEITE	Oxide				
	Bitikleite		Ca_3	$Sb^{5+}Sn^{4+}$	Al_3	O_{12}
	Usturite		Ca_3	$Sb^{5+}Zr$	Fe_3^{3+}	O_{12}
	Dzhuluite		Ca_3	$Sb^{5+}Sn^{4+}$	Fe_3^{3+}	O_{12}
	Elbrusite		Ca_3	$U_{0.5}^{6+}Zr_{1.5}$	Fe_3^{3+}	O_{12}
10	SCHORLOMITE	Silicate				
	Kimzeyite		Ca_3	Zr_2	$SiAl_2$	O_{12}
	Irinarassite		Ca_3	Sn_2^{4+}	$SiAl_2$	O_{12}
	Schorlomite		Ca_3	Ti_2	$SiFe_2^{3+}$	O_{12}
	Kerimasite		Ca_3	Zr_2	$SiFe_2^{3+}$	O_{12}
	Toturite		Ca_3	Sn_2^{4+}	$SiFe_2^{3+}$	O_{12}
12	GARNET	Silicate				
	Menzerite-(Y)		Y_3Ca	Mg_2	Si_3	O_{12}
	Pyrope		Mg_3	Al_2	Si_3	O_{12}
	Grossular		Ca_3	Al_2	Si_3	O_{12}
	Spessartine		Mn_3^{3+}	Al_2	Si_3	O_{12}
	Almandine		Fe_3^{2+}	Al_2	Si_3	O_{12}
	Eringaite		Ca_3	Sc_2	Si_3	O_{12}
	Goldmanite		Ca_3	V_2^{3+}	Si_3	O_{12}
	Momoiite		Mn_3^{3+}	V_2^{3+}	Si_3	O_{12}
	Knorringite		Mg_3	Cr_2^{3+}	Si_3	O_{12}
	Uvarovite		Ca_3	Cr_2^{3+}	Si_3	O_{12}
	Andradite		Ca_3	Fe_2^{3+}	Si_3	O_{12}
	Calderite		Mn_3^{3+}	Fe_2^{3+}	Si_3	O_{12}
	Majorite		Mg_3	$SiMg$	Si_3	O_{12}
	Morimotoite		Ca_3	$TiFe^{2+}$	Si_3	O_{12}
15	BERZELIITE	Vanadate, arsenate				
	Schäferite		Ca_2Na	Mg_2	V_3^{5+}	O_{12}
	Palenzonaite		Ca_2Na	Mn_2^{2+}	V_3^{5+}	O_{12}
	Berzeliite		Ca_2Na	Mg_2	As_3^{5+}	O_{12}
	Manganberzeliite		Ca_2Na	Mn_2^{2+}	As_3^{5+}	O_{12}

Notes: Formulas are given in the form $\{X_3\}[Y_2](Z_3)\varphi_{12}$. Group names are given in capitals.

The garnet structure is remarkably flexible in a chemical sense: 58 elements were reported in the Inorganic Crystal Structure Database in 2007. Moreover, in the period of 2009 – 2010, 10 new garnets, with constituents such

as Sc, Y, Sn, Sb, and U were approved by the Commission on New Minerals, Nomenclature and Classification (CNMNC) of the International Mineralogical Association (IMA), resulting in a nearly 50% increase in the number of accepted species with the garnet structure. There are four more possible species, bringing to 26 the number of elements essential to defining existing and possible mineral species with the garnet structure. In view of this situation, a new revised nomenclature of garnet structure minerals was approved. It is recommended do not subdivide of the groups into mineral subgroups or mineral series, discouraging the traditional division of the garnet group into the "pyralspite" and "ugrandite" species or series, although there could be some fundamental structural differences that limit solid solution between the two groupings [32]. The garnet supergroup includes all minerals isostructural with garnet regardless of what elements occupy the four atomic sites, i.e., the supergroup includes several chemical classes, not only silicates as it was before. These two statements are the most important changes in new garnet structure nomenclature. After revision there are 32 approved species of natural garnets, with an additional 5 possible species [32]. One optional grouping is suggested, to subdivide the supergroup into groups based on symmetry and total charge at the tetrahedral Z site. All 32 approved species of minerals are listed in Table 1 and suggested subgrouping named in capital letters [32]. In this case 29 species from 32 belong to one of five groups: one tetragonal (henritermierite, charge of Z = 8), and four isometric – bitikleite (Z = 9), schorlomite (Z = 10), garnet (Z = 12), and berzeliite (Z = 15). Rest three species are single representatives of potential groups in which total charge at Z is 0 (katoite), 3 (cryolithionite), and 6 (yafsoanite) [32].

The garnets with space group $Ia\bar{3}d$ have a cubic face-centred lattice (point group $m\bar{3}m$) with 160 atoms [23], formed of eight formula units per unit cell [36, 37]. The cations are all in special positions with no positional degrees of freedom, while the oxygen atoms are in the general positions. More crystallographic data of this garnet structure symmetry are given in Table 2 [25, 32, 33]. The same rules are applied to the rare earth garnets, also to the

rare earth gallium garnets. The RE^{3+} ions reside in an eight-coordinated site while 40% of the lighter host cations (like Ga, Al, Fe and etc.) are in a six-coordinated (octahedral) site. The remaining 60% of lighter ions (possibly the gallium ions) lie in a four coordinated (tetrahedral) site. The six- and four-coordinated sites are rather undistorted while the coordination around the RE^{3+} ions is much further from the ideal dodecahedron [37].

Table 2. Crystallographic description of garnet structure [25].

Point symmetry	222	$\bar{3}$	$\bar{4}$	$\bar{1}$
Space group position	24*c*	16*a*	24*d*	96*h*
Typical ideal formula	$\{Ca_3\}$	$[Al_2]$	(Si_3)	O_{12}
Coordination to oxygen	8	6	4	
Type polyhedron	Dodecahedron (distorted cube)	octahedron	tetrahedron	

The crystal structure visualization of $Gd_3Sc_2Ga_3O_{12}$ garnet is given in a Fig. 1. The unit cell is presented at the left, in orientation [0;1;0] along [h;k;l]. Gd^{3+} atoms in dodecahedron atom sites are presented as grey colour bubbles, Sc^{3+} at octahedron – blue and Ga^{3+} at tetrahedron are green. The smallest – red balls represents O atoms. The middle and right pictures nicely shows polyhedral dislocations of metals in one formula unit, orientations are kept same like in unit cell, [0;1;0].

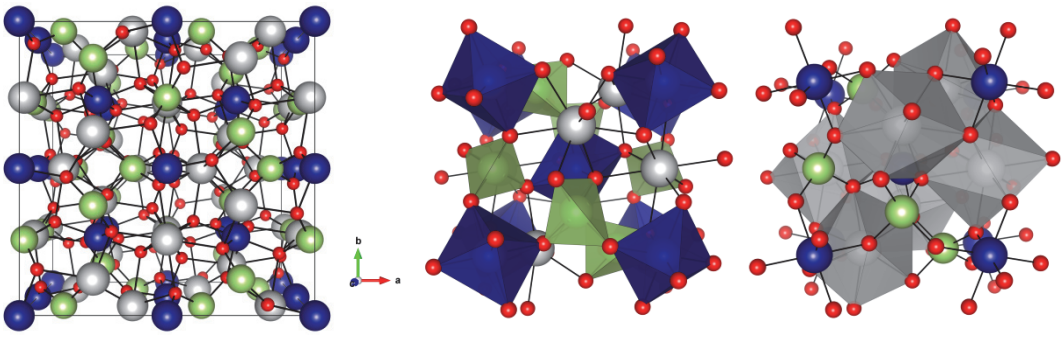

Fig. 1. Crystal structure of $Gd_3Sc_2Ga_3O_{12}$ garnet, from left to right: unit cell; formula unit with Sc^{3+} and Ga^{3+} polyhedrons; formula unit with Gd^{3+} polyhedrons. Pictures are drawn with VESTA program.

As it was mentioned, the garnet structure is extraordinary flexible in a chemical composition. This capacity has an influence for some

crystallographic parameters, like lattice constant, and of course affects their physical properties. The lattice constant *a* for all known garnets vary in the range of 11.91 – 13.10 Å [25]. The lattice constants of some garnets are given in Table 3.

Table 3. Lattice parameters of some garnet structure compounds, $Ia\bar{3}d$ space group.

Natural garnets				Synthetic garnets		
Mineral name	Formula	*a* [Å]	Ref.	Formula	*a* [Å]	Ref.
Pyrope	$Mg_3Al_2Si_3O_{12}$	11.4582(5)	[38]	$Y_3Al_2Al_3O_{12}$	12.0062(5)	[39]
Grossular	$Ca_3Al_2Si_3O_{12}$	11.8504(4)	[38]	$Y_3Fe_2Fe_3O_{12}$	12.375(1)	[40]
Almandine	$Fe_3^{2+}Al_2Si_3O_{12}$	11.525(1)	[41]	$Gd_3Sc_2Ga_3O_{12}$	12.5502	[42]
Uvarovite	$Ca_3Cr_2^{3+}Si_3O_{12}$	12.0205(5)	[43]	$Gd_3Ga_2Ga_3O_{12}$	12.3829(5)	[44]
Knorringite	$Mg_3Cr_2^{3+}Si_2O_{12}$	11.6040	[45]	$Y_3Ga_2Ga_3O_{12}$	12.273(1)	[40]
Cryolithionite	$Na_3Al_2Li_3F_{12}$	12.120(4)	[46]	$Lu_3Ga_2Ga_3O_{12}$	12.18	[47]

The primary importance factor for variation of parameter *a* is relative difference of ionic size of atoms in the unit cell. There are a lot of research done for structure refinement using experimental data, for better understanding site occupation preference of different metal ions in garnet structure. For example, the Ga^{3+} ions show greater preference for the tetrahedral sites in $Y_3Fe_{5-x}Ga_xO_{12}$ than Al^{3+} ions in analogues $Y_3Fe_{5-x}Al_xO_{12}$ system, when x = 2.75. However, if x is bigger the preference of Ga^{3+} ions for tetrahedral sites may be the same as or less than that of Al^{3+} ions [48]. This knowledge is the determinant factor of modelling new garnets for certain applications, like luminescence.

Already in 1962 Espinosa [49] plotted lattice parameter *a* of the Fe garnets vs the atomic number Z_R of the rare-earth elements RE. A double festoon curve was obtained, caused by crystal field effects on the non-spherical RE^{3+} ions. Euler et al. [33] filled this dependence by adding series of Ga and Al garnets (Fig. 2). The obtained results showed that the scale of these effects is different in the Fe and Ga series. But the situation was different with the Al series. Apparently, the higher electron density of the latter resists the compression imposed by the small lattice of the Al-garnets and demands an additional increase of *a* with increasing size of RE.

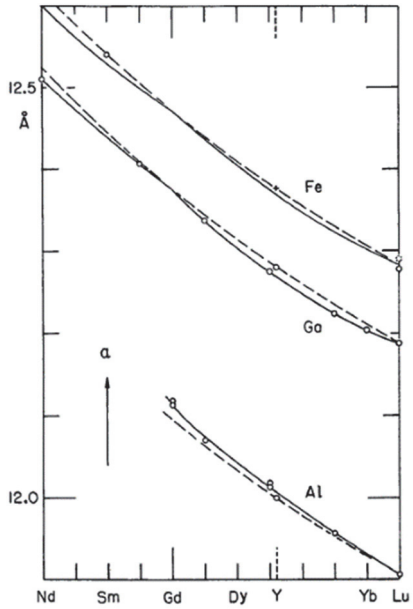

Fig. 2. Lattice constants *a* of rare-earth garnets $RE_3M_5O_{12}$ (M = Al, Ga and Fe) as function of the atomic numbers of the rare earths RE. Circles indicate measurements data. The data on the Fe series were taken from Espinosa (1962) with YIG fitted to the broken curve for spherical electron configurations of RE [33].

The investigations on the elastic and photoelastic properties of the garnet crystals carried out by Kitaeva et al. [36] give some guidelines on the features of the sound propagation in these crystals, the character of the force interaction between ions in the crystal lattice, the regularities of the photon-phonon interaction, and how these properties are changing in the series of garnets. The big experimental work could be concluded be few statements [36]. The elastic isotropy parameter of these crystals does not differ much from unity and slightly changes with the increase of lattice parameter *a* and molecular weight M. The light garnets are anisotropic in their photoelastic properties, the heavier garnets are characterized by smaller anisotropy. The obtained results and given dependences provide sufficiently exact estimation of the mechanical, thermophysical, and photoelastic parameters of the garnets.

The crystal field of a given ion (*Dq*) is another important factor for the optical properties caused by the influence of the host lattice. Two compounds with the same crystal structure and optical centre (Cr^{3+} ion) have different

colour (Cr_2O_3 is green and Al_2O_3:Cr^{3+} (ruby) is red). In ruby the Cr^{3+} ions occupy the smaller Al^{3+} site, so latter feel a stronger crystal field than in Cr_2O_3. Consequently, the optical transitions in ruby are at higher energy than in Cr_2O_3. The spectral position of certain optical transitions is determined by the strength of the crystal field, the transition metal ions being the most well-known and clear example. For latter the optically active d-electron shell is incompletely filled, i.e. their electron configuration is d^n ($0 < n < 10$). The energy levels originating from such configurations have been calculated by Yukito Tanabe and Satoru Sugano [50, 51]. So called Tanabe-Sugano energy-level diagrams illustrate the dependence of energy levels of transition metal ions on the crystal field strength (the crystal field splitting parameter is *10Dq*) [52, 53]. To make calculations possible, Giulio Racah method was employed [54, 55]. These adaptions for equations shortly are called Recah parameters. In addition, the crystal field is responsible for the splitting of certain optical transitions. When optical centre ion is occupying site of larger radii ion in a crystal lattice, the inter-atomic distances increase and the crystal field strength for it is weaker. By altering the ionic radii in certain cation site, it is possible to alter distance and thus vary the strength of the crystal field acting on the ion [52, 56-60]. For example, Cr^{3+} or Mn^{4+} have same electron configuration $3d^3$ and the emission can vary considerably from 600 nm to 775 nm. This remarkable variation in the emission energy is connected with the chemical bonding between ion and host lattice ligand [52]. For some structures and elements this dependency could be expressed like:

$$10 \cdot Dq = \frac{K}{R^n} \qquad \text{(Eq. 1)}$$

here R is bond distance, K is a constant and the exponent n is constant close to 5 [52, 59].

In the garnet structure materials the crystal field strength for the octahedral site ion could be also estimated by Tanabe and Sugano energy level diagrams [53, 61]. The crystal field strength (Dq) and the Racah parameter (B) are carefully calculated for Cr^{3+} ion in $Y_3Ga_5O_{12}$, $Y_3(Sc,Ga)_2Ga_3O_{12}$,

$Gd_3Ga_5O_{12}$, $Gd_3(Sc,Ga)_2Ga_3O_{12}$, and $(La,Lu)_5Ga_3O_{12}$ garnets by following equations:

$$10 \cdot Dq = E_a(^4T_2(t_2^2e)) \quad \text{(Eq. 2)}$$

$$\frac{Dq}{B} = \frac{15(x-8)}{x^2-10x} \quad \text{(Eq. 3)}$$

$$Dq \cdot x = E_a(^4T_1(t_2^2e)) - E_a(^4T_2(t_2^2e)) \quad \text{(Eq. 4)}$$

The crystal field strength equations were also done analogously for other structures or elements [52, 53], but in the most cases to determine the energy levels directly from measurements is very complicated task [61].

The sinterability and microstructural evolution of mixed-metal $Y_3Al_{5-x}Cr_xO_{12}$ (YACRG), $Y_3Al_{5-x}Mn_xO_{12}$ (YAMNG), $Y_3Al_{5-x}Ni_xO_{12}$ (YANIG), $Y_3Al_{5-x}Co_xO_{12}$ (YACOG), $Y_3Al_{5-x}Cu_xO_{12}$ (YACUG) and $Y_3Fe_{5-x}Co_xO_{12}$ (YICOG) ($0 < x < 2.75$) garnets powders, synthesized by an aqueous sol-gel process, were also investigated [62]. It was demonstrated for the first time that the formation of single-phase products proceeded only within a narrow substitutional range. A considerably less substitutional level was observed for the YACUG garnet. On the other hand, the formation of monophasic YICOG garnet did not proceed at the same synthesis conditions. The pure phase of YANIG has also not been obtained. Thus, the formation of a single-phase material depends on the chemical stoichiometry of the reaction system. The garnet phase was destructed with the increase of the introduced amount of M from $x = 0.50$ to $x = 1.25$ in $Y_3Al_{5-x}M_xO_{12}$ (M = Cr, Mn, Ni, Co), presumably due to the characteristic oxidation states of element M and larger ion M radius than ion Al^{3+}. Interestingly, almost linear dependence determined between the limitary radius of garnet structure and the ionic radius of M substituent distributed in the tetrahedral or octahedral sites of an aluminium ion. The calculated limitary radius varied in the range 0.516 – 0.548 Å. The authors found “Protection Effect” of the garnet structure. In exceptional cases, the crystal lattice tried to protect itself from the destruction. However, no additional literature data confirming this assumption was found. For instance, the samarium, europium and gadolinium orthoferrites ($RFeO_3$) were dominant

after heat-treatment of precursor gels at 800 °C (see Fig. 3). By increasing the temperature to 900 °C, $SmFeO_3$ still remained the main crystalline phase in the end product.

Rare earth iron garnets with the composition of $RE_3Fe_5O_{12}$ (RE = Sm, Eu, Gd, Tb, Dy, Ho, Er, Tm, Yb, Lu) were also fabricated by a simple and effective aqueous sol-gel method [9]. It was demonstrated that pure $Sm_3Fe_5O_{12}$ phase was obtained only after annealing the precursor gel at 1000 °C (Fig. 3).

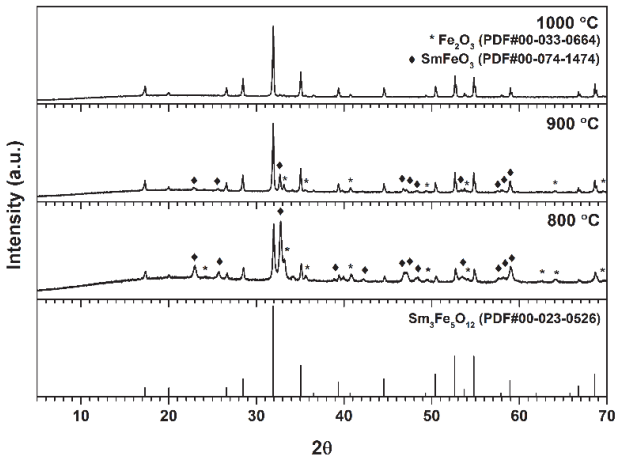

Fig. 3. XRD patterns of Sm–Fe–O gels annealed at 800, 900 and 1000 °C. The vertical lines represent the standard XRD pattern of $Sm_3Fe_5O_{12}$.

The phase purity of $Tb_3Fe_5O_{12}$ and $Dy_3Fe_5O_{12}$ garnets was almost independent on the synthesis temperature in the range of 800 – 1000 °C. However, the purest $Ho_3Fe_5O_{12}$, $Er_3Fe_5O_{12}$ and $Tm_3Fe_5O_{12}$ garnet phases were obtained already at the lowest used synthesis temperature (800 °C). With the increasing synthesis temperature the amount of side perovskite $HoFeO_3$, $ErFeO_3$ and $TmFeO_3$ phases also increased. Interestingly, the monophasic ytterbium and lutetium iron garnets ($Yb_3Fe_5O_{12}$ and $Lu_3Fe_5O_{12}$) were successfully synthesized only at 800 °C (Fig. 4) [9].

The monophasic neodymium-doped and neodymium and europium co-doped $Y_{3-x}Nd_xAl_5O_{12}$:Eu garnets recently were synthesized at 1000 °C using the sol-gel chemistry approach [63]. ^{27}Al NMR spectroscopy was used to investigate structural features. It was demonstrated that with increasing amount of neodymium the less intensive and broader peaks were observed. The

intensity of peaks attributable to the Al-Eu increased proportionally with increasing the doping level of europium.

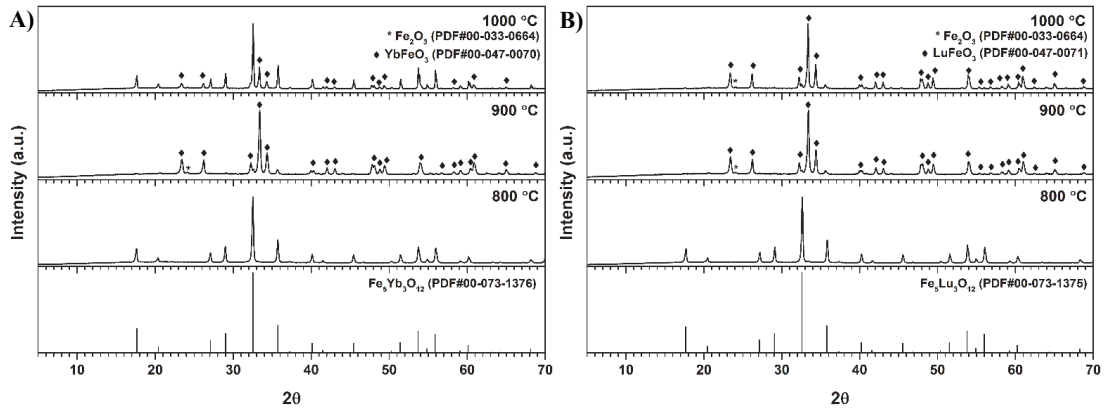

Fig. 4. XRD patterns of Yb–Fe–O (A) and Lu–Fe–O (B) gels annealed at 800, 900 and 1000 °C. The vertical lines represent the standard XRD patterns of $Yb_3Fe_5O_{12}$ and $Lu_3Fe_5O_{12}$, respectively.

1.1.2. Main Application

The garnet family is important in geophysics and planetary science since the garnet is one of the major constituent minerals of the upper mantle and of the transition zone in the earth. But the technological importance of the naturally occurring garnets has been limited to that of mild abrasives. The garnet paper, limited used to smooth wood, because there are better abrasives for this application. Some silicate garnets are semi-precious and are used in jewellery [25]. Attention to the $Y_3Fe_5O_{12}$ (YIG) was increased due to its ferrimagnetic properties [64]. Rare earth iron garnets (REIG) were found to be ferrimagnetic with compensation temperatures, ferromagnetic resonance, linewidths and giant anisotropy peaks. Their unambiguous chemical constitutions in the same crystal structure host facilitated the theoretical interpretation of basic magnetic processes. Furthermore, garnets achieved even greater prominence as in its present role as the leading magnetic bubble domain device material for integrated circuit memory and charged coupled devices, as the next generation of computer memory technology. With the discovery of a uniaxial anisotropy in the rare earth iron garnets the need for

thin films of these materials also increased. For that reason the $Gd_3Ga_5O_{12}$ (GGG) was used as a substrate material for YIG [64-67].

YIG has interesting Faraday rotation properties. Faraday isolators (FIs) are fundamental components used in advanced optical communications systems to prevent harmful back-reflections and to eliminate parasitic oscillations in amplifier systems or frequency instabilities in laser diodes. YIG and Bi doped YIG materials with high transparency in the infrared regions were employed and characterized by a very large Verdet constant. Recently, the quantum based super exchange interaction between Tb^{3+} and other paramagnetic RE^{3+} ions can occur, greatly enhancing the Faraday effect has been determined. The RE^{3+} doped terbium gallium garnet ($Tb_3Ga_5O_{12}$, TGG) single crystals with high concentration of efficient paramagnetic RE^{3+} ions showed excellent magneto-optical properties in UV-VIS region giving the huge possibility to reduce the intensity of the necessary magnetic fields. TGG large size single crystal has more favourable growth characteristics and high transmittance and is a promising magneto-optical material for high-power FIs applications [68, 69].

Demands of high quality laser crystals spurred extensive studies of YAG, which soon became the most important scintillating material. Thus, the synthetic garnets have become a rich field for both scientific and technological exploration. The discovery and development of new phosphors, Light Emitting Diodes (LED) phosphors, significantly increased attention to the garnet structure materials. The main yellow phosphor used in pcLEDs, $Y_3Al_5O_{12}:Ce^{3+}$ (YAG:Ce), was reported in 1967 with its primary use in cathode-ray tubes. Thus, the garnet crystals and polycrystalline bulk materials activated with RE^{3+} ions show very interesting applications in the field of optical materials, such as scintillators for detection of high energy radiation, white LED lighting, classical and quantum information processing and fluorescence thermometry. The scientific literature still abounds with papers on various studies of the garnets and wide range of their luminescent properties [25, 36, 67, 70-72].

The wide scale of material forms used in various industrial applications includes polycrystalline samples, ceramics, single crystals and thin/thick films [73-76]. The availability of garnets with excellent quality and the demand for garnet materials have accelerated and expanded their production. New and innovative preparation methods are being developed to fabricate better quality garnets.

1.1.3. Synthesis Methods of Garnets

Physical state of materials implies their possible applications. In this section of dissertation the short review of possible and most popular synthesis methods for bulk, monocrystalline and thin film garnets is presented. There are thousands of articles about their synthesis, here reference is given to the most detailed articles on the synthesis pathways.

1.1.3.1. Bulk

The most widely used synthesis method for garnet powders is solid-state reaction route. Usually metal oxides or carbonates are used as starting materials. The correct amounts of precursor powder are thoroughly mixed either in the mortar or using ball mill with some acetone or alcohol. The samples might be pressed in to pellets and should undergo repeated heat treatments at high temperatures (1250 – 1650 °C) with intermediate grindings [77-79]. Jian Xu et al. [80] and [81] improved the traditional solid-state synthesis by applying vacuum during the heating procedure obtaining the transparent ceramics of garnets. The correct sintering temperature is the most important parameter of solid-state reaction synthesis method. The disadvantage lies, however, in the contamination of the end products due to incomplete phase formation [64]. The solid-state reaction method does not allow getting nano-sized powders as a product.

As opposed to high temperature solid-state synthesis the first paper of the sol-gel synthesis of YAG was published in 1986 [72]. All synthesis from solutions have general advantages: perfect homogeneity of product, lover

sintering temperatures and possibility to obtain nano-sized particles [72]. The YAG:Ho^{3+}/Yb^{3+} nano-crystalline sample prepared by the co-precipitation method showed interesting up-conversion properties [72]. In the co-precipitation method, the mixed cations are precipitated out of solution by suitable agents - precipitant (usually hydroxides, NH_4HCO_3 or NH_3 aqueous solution) [64, 72]. The starting reagents, metal oxides, are separately dissolved in a HNO_3 and the resulting solutions are mixed and stirred at room temperature. The obtained solution under vigorous stirring is added dropwise in to precipitant solution or the other way round, both way it is advised to keep constant pH = 10. The co-precipitates are filtered under vacuum, washed several times and then oven dried. The product powders are obtained after heat treatment at 500 – 900 °C. In some cases, the heating is repeated with intermediate grinding or ball milling procedures. The disadvantages of this method are the limits placed on the types of cations, the difficulty and inefficiency of the filtration process [64, 82-84].

The sol-gel technique is other method suitable for the synthesis of nano-scaled garnets. The sol-gel method offers the advantage of high purity, uniformity and low temperature processing [67, 85]. By Pechini method the stoichiometric amount of metal chlorides, acetates or nitrates for the corresponding garnet composition have to be dissolved in water and mixed with suitable quantities of citric acid and ethylene glycol [72, 85, 86] or PEG [82]. In the citrate sol-gel process metal nitrates and citric acid is added with a molar ratio of 1:2 [67, 87]. As a complexing agent the ethylene glycol [71], glycerol or some suitable combinations of them could be used [88]. When all components are mixed, the obtained system are stirred for several hours and concentrated by slow evaporation at 70 – 90 °C to form gels. The gels are dried for 12 – 72 h at 90 – 130 °C. Then the amorphous gel samples are heated at 700 – 1200 °C for 6 – 16 h. In some synthesis the preheating is applied (500 – 800 °C) in order to remove the residual nitrates and organic compounds before the final annealing. The sol-gel processing parameters, such as pH of starting solution, concentration and nature of complexing ligand, temperature and

duration of gelation, powder re-homogenization during annealing, duration and temperature of the final heat treatment were found to be the most significant. These parameters are very much responsible for the crystallinity, crystal shape, crystal size, crystal size distribution and phase purity of the resulting powders [6, 67, 71, 72, 82, 85, 87, 88].

The sol-gel combustion synthesis process follows the same path like previously described sol-gel synthesis route, except one intrinsic aspect – auto/self-initiated combustion process, the exothermic reaction between the metal nitrates (oxidizer), used as precursors, and an organic fuel. The complexing agents like citric acid, glycine, carbohydrazide and tris(hydroxymethyl)–aminomethane could play like a fuel at the same time [72, 89-92] or used together with additional fuels, e.g. ethylenediamine or urea [72, 89, 91], mixture of urea and glycine [18]. After evaporation of solvent auto combustion is initiated variously: heated with a Bunsen flame [89], dried gel placed in an preheated oven for a few minutes [90, 91] or raised temperature of hot-plate [92]. After self-combustion very porous fluffy powders remain and after last heating garnets are obtained [89-92]. The use of fuel mixtures facilitated the direct formation of phase pure nano-sized (50 – 90 nm) spherical particles of $Gd_3Ga_5O_{12}$ [91]. The near-infrared to visible up-conversion in nano-crystalline $Gd_3Ga_5O_{12}$ doped with Er^{3+} ions and synthesized at 500 °C was obtained [89].

Eu^{3+}-doped holmium aluminium garnet ($Ho_3Al_5O_{12}$, HoAG) has been synthesized by solvothermal method [93]. Solvothermally synthesized HoAG:Eu^{3+} garnet samples were monophasic compounds (see Fig. 5). Apparently, europium does not affect the formation of garnet structure up to concentration of 5%. No any new peaks or/and any shifted peaks have been determined in the XRD patterns of differently Eu^{3+}-doped holmium aluminium garnets.

The powders can be used as starting materials for single crystal growth or for synthesis of polycrystalline transparent ceramics. The technologies that offer distinct technical advantages and also minimize toxicity in conventional

syntheses are the most likely to be adapted in the demanding fabrication schemes. An aqueous sol-gel technique may provide both of these advantages. As a result, an aqueous sol-gel process is likely to continue attracting the attention of chemists interested in the designing advanced functional nanomaterials [6].

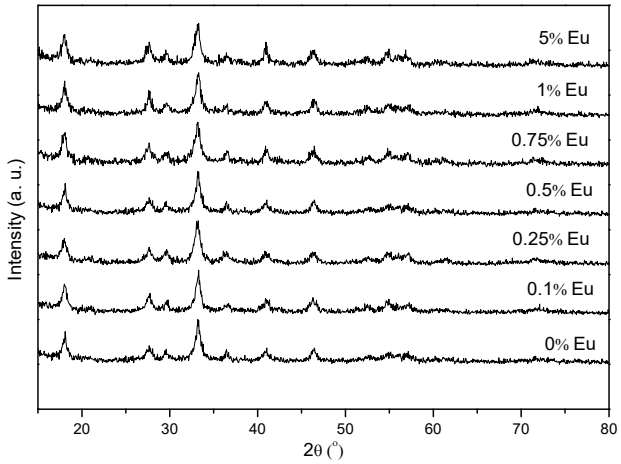

Fig. 5. XRD patterns of HoAG samples doped with different amount of europium ions and synthesized by solvothermal method at 220 °C for 20 h.

1.1.3.2. Monocrystals

For the growth of single crystal garnets, the Czochralski (Cz) method is the most popular. High-purity oxides are mixed according to the designed garnet stoichiometric formula. As was mentioned, the bulk polycrystalline garnet materials could be applied as starting materials for single crystal growth. After the polycrystalline materials are melted and when the melt is homogeneous an appropriate crystal seed, fixed in chosen [h;k;l] orientation, is dipped into the melt. This seed is slowly pulled up initiates the single crystal formation. The pulling and the rotation rates, temperatures of the melt and in the chamber, gas atmosphere have to be optimized and controlled accurately in order to avoid crystal imperfections such as strain, second phase precipitates and voids. The Y, Nd, Sm, Eu, Gd, Tb, Dy, Ho, Er, Tm, Yb, and Lu gallium garnet crystals were synthesized by Cz method [64, 65, 94, 95]. In addition, to the rare earth gallium garnets, solid solution single crystals of $Gd_3Ga_5O_{12}$-$Dy_3Ga_5O_{12}$, $Sm_3Ga_5O_{12}$-$Nd_3Ga_5O_{12}$ and $Sm_3Ga_5O_{12}$-$Gd_3Ga_5O_{12}$ have been also

grown [65]. The obtained distribution coefficients were close to one and only very small variations in the lattice parameter were observed. An Nd^{3+} doped calcium tantalum gallium garnet (CTGG) single crystal was grown by the Cz method with very broad fluorescence bands that might be employed in tunable and ultra-short-pulse lasers [96]. Highly transparent pure $Tb_3Ga_5O_{12}$ (TGG) single crystals and doped with Tm^{3+}, Dy^{3+}, $Er^{3+}$and Ce^{3+} were effective Faraday isolators [68, 69, 97, 98].

The Czochraski method using an iridium crucible for the garnets crystals shows shortcomings, like oxidation of iridium crucible in oxygen atmosphere (melt's pollution) and problematic composition control (volatilization of Ga_2O_3 at high temperature). Around half a century ago Optical Floating Zone (OFZ) growth technique (the Traveling Solvent Floating Zone Method) has been suggested. The TGG single crystal also was grown by the OFZ growth technique [99]. The OFZ method compared with the Cz method covers the following advantages: higher growth rate, no need for a crucible and growth in a high oxygen atmosphere [100]. For the crystal growth by OFZ method the same precursors could be used. The feed and seed rods are prepared by hydrostatically pressed powder placed in a rubber pipe. The obtained rods were sintered at high-temperature (1300 – 1500 °C) for 10 – 20 h. The OFZ furnace for the crystal growth might be equipped with two or four lamps (Halogen or Xenon). The careful control and finely adjust lamp power is very important. Moreover, in order to obtain a high quality crystal the growth rate, atmosphere (gas composition and flow rate), rotation rates of the feed and seed rods should be also carefully controlled. The crystals after the growth are annealed in order to eliminate thermal stress formed during the growth process [16, 99, 100]. The neodymium-doped gadolinium scandium gallium garnet (Nd:GSGG) crystal was recently grown by this comparatively new method. The excellent optical quality Nd:GSGG crystal has been demonstrated [100]. The single phase europium-doped YAG and YGG crystals were grown as well [16]. The obtained crystals showed the luminescence properties which are of interest for challenging biomedical application.

The vertical Bridgman (VB) method is one more crystal growth method for the garnets. The sintered mixture is charged into a large conical shape Pt crucible. The crucible has bottom with the long tail (much thinner than crucible diameter) were crystal seed is placed. The growth experiments are carried out in a vertical Bridgman furnace with three resistance-heating zones. This technique requires stable and suitable temperature gradient control and optimized pulling down rate. The transparent calcium lithium niobium gallium garnet crystals with the size of 25 mm in diameter and 70 mm in length were grown by Xu et al. [101]. The Cr-doped $(Gd_xY_{1-x})_3Ga_5O_{12}$ crystals were grown by Kurosawa et al. [102].

All described crystal growth methods could be used to grow large (centimetres scale) crystals. The flux grow method could be used to obtain only small crystals [77]. The flux growth method uses molten inorganic compounds solvents, the fluxes might be PbO, PbO-PbF_2, PbO-B_2O_3, BaO-B_2O_3, PbO-PbF_2-B_2O_3, PbO-Bi_2O_3, Bi_2O_3-V_2O_5 and other [64, 77]. The advantages of the flux growth method include the rapid rates of crystallization for a solvent-solute system, the large number of suitable inorganic solvents and its special ability to grow incongruently melting crystals. The biggest disadvantage is the introduction of impurities from the solvents. The flux growth method is the only reliable method used for incongruently melting iron garnet crystals growth [64]. The attention has to be put on the flux choice, temperature of melting, soaking time and cooling rate. Interestingly, rather large crystals of YAG and REAG (each crystal ~ 60 g) with optical quality were grown with PbO-PbF_2-B_2O_3 [64].

1.1.3.3. Thin Films

The development of micro-imaging technique strongly demands creation of the new scintillating single crystalline film screens based on the different oxide compounds (garnets, perovskites, orthosilicates) with high absorption ability of X-rays which can effectively emit in the visible or ultraviolet (UV) range. Therefore, the preparation of thin films using different

synthesis techniques is very important task as well [103, 104]. Co^{2+}:GGG epitaxial films have been grown with high structural perfection and good optical quality from super-cooled high temperature solution [103]. The $Lu_3Al_{5-x}Ga_xO_{12}$:Pr single crystalline films were grown by the same technique possessing good optical and structural quality [104].

Thin polycrystalline garnet films can be prepared on different substrates through heat treatment amorphous mixtures of the appropriate metal ions via Radio Frequency Sputtering (RFS), Chemical Vapour Deposition (CVD), Sol-Gel spin (SGSS) or dip (SGSD) coating techniques. The two sputtering techniques, radio frequency diode and magnetron sputtering, from ceramic targets of the constituent oxides, produce the dense amorphous mixtures with compositions and microstructures dependent on the target composition, the sputtering rates of the target constituents and the sputtering parameters. The magnetron sputtering is more widely employed for the higher deposition rates for the films with different composition. RFS deposition in combination with in-situ crystallization allows obtaining compositions which are difficult to obtain by other techniques, but places strict requirements on process control and target fabrication. The conditions during the annealing stage largely implies the grain size and distribution and the microstructure of obtained films [105]. Cr^{3+}-doped YGG thin films (ranged in thickness from 1 μm to 1.3 μm) were sputtered onto YAG substrates (single crystal) by Yamaga et al. [106].

The solution-based sol-gel method is one of the most important techniques for the synthesis of various functional materials. The solutions are typically spin coated or dip coated onto the substrates; the solvent evaporated and the solute decomposed by a heat treatment in air leaving the amorphous oxides. The spin coating/pyrolysis can be repeated until the desired thickness is reached, and then the film is fired to form the garnet phase. The shelf life and stability of the organic solutions is typically better than that of the inorganic solutions. The proper solution rheology for spin coating, the solubility of the solute system and the time and temperature of the decomposition are critical to obtaining high quality films [105]. The thin films of $Gd_{3(1-x)}Ln_{3x}Ga_5O_{12}$ doped

with Eu^{3+}, Tb^{3+} and Er^{3+} were prepared by a Pechini sol-gel process by dip coating technique on a silica glass substrates. The rare earth ions Eu^{3+}, Tb^{3+} and Er^{3+} show their characteristic orange ($^5D_0$–$^7F_1$), green ($^5D_4$–$^7F_5$) and green ($^4S_{3/2}$–$^4I_{15/2}$) emissions in the crystalline GGG films [107].

The successful preparation of polycrystalline thin film composed of a single phase of $Bi_3Fe_5O_{12}$ on a fused silica (amorphous SiO_2) substrate by using the CVD method was also recently developed [108]. Yttrium aluminium garnet thin films deposited on silicon substrates were prepared by an aqueous sol-gel route using metal nitrates [109].

1.1.4. Luminescence Properties of Garnets

The best known garnet is $Y_3Al_5O_{12}$ (YAG), which is widely studied and used as host lattice for the laser materials. However, the gadolinium gallium garnet $Gd_3Ga_5O_{12}$ (GGG) possesses several advantages over the YAG single crystals as its melting temperature is lower, growth rate is faster, and it is possible to obtain crystals with large dimensions, high optical quality and higher concentration of activator ions. Also, GGG has a higher refraction index than YAG, which is beneficial for radiative transitions in RE^{3+} ions. Consequently, the GGG is also very important garnet for magneto-optic applications. The garnets as hosts for luminescent dopants are characterized by many favourable chemical and physical properties, such as stability, relatively easy preparation, low vibrational frequencies and good thermal conductivity [72, 89, 96, 100, 107].

The emission spectra of $Y_3Ga_5O_{12}$ (YGG) nano-powders doped with Dy^{3+} upon excitation at 448 nm showed two bands centred at 485 (blue) and 585 nm (yellow) which corresponds to the $^4F_{9/2}\rightarrow{}^6H_{15/2}$ and $^4F_{9/2}\rightarrow{}^6H_{13/2}$ transitions of Dy^{3+} ion. Integrated yellow to blue (Y/B) emission intensity was found to be increased with increasing the Ga content in the $Y_3Al_{5-x}Ga_xO_{12}$ (YAGG) host [110]. By partially replacing Ga^{3+} by Sc^{3+} in GGG, a new class of garnets ($Gd_3Sc_2Ga_3O_{12}$, GSGG) was formed. It has been demonstrated that the Nd^{3+} distribution coefficient in GSGG is higher than in the Nd:GGG, which

suggests that the existence of Sc^{3+} is favourable for higher Nd^{3+} doping concentration and better optical quality. Additionally, it has been confirmed that GSGG exhibits better radiation resistance than YAG when exposed to ionizing radiation. This means that it has potential applications in a hostile environment. Recently, many rare-earths (such as Nd^{3+}, Yb^{3+} and Er^{3+}) doped crystals with garnet structure containing scandium ($Y_3Sc_2Al_3O_{12}$, $Y_3Sc_2Ga_3O_{12}$, $Lu_3Sc_2Ga_3O_{12}$) have been studied extensively as laser host materials [100].

The first report on frequency up-conversion in nano-crystalline garnet materials was published by Vetrone et al. [89]. The nano-sized GGG doped with Er^{3+} was prepared by solution combustion synthesis approach. The samples upon excitation at 488 nm showed strong room temperature emission in the green, red and IR spectral regions, and upon IR excitation at 800 nm showed efficient anti-Stokes up-conversion emission peaking in the green region around 560 nm. The up-conversion phenomena were reported in nano-crystalline Er^{3+} [89] or Ho^{3+} ions [72] doped GGG, and Er^{3+} [87], Ho^{3+}/Yb^{3+} [87] or $Tm^{3+}/Er^{3+}/Yb^{3+}$ [72] ions doped $Lu_3Ga_5O_{12}$ (LuGG) powders. Laser infrared excitation at 980 nm can also be used to generate white light emission in nano-crystalline garnet based materials [72].

The Cr-doped $(Gd_xY_{1-x})_3Ga_5O_{12}$ crystals as alternative candidates for red/infrared scintillator applications were discussed in [102]. The infrared light scintillators might be used in medicine as the real-time radiation dosimeters applied in medical together with irradiation treatment. Accurate control of intensity of the treatment is desired to reduce or avoid unwanted side effects. Due to the many practical applications, the $3d^3$ ions (e.g. Cr^{3+}, V^{2+}, Mn^{4+}) in octahedral crystal fields have the orbit singlet $^4A_{2g}$ as the electronic ground state. In weak crystal fields, $Dq\ /\ B \leq 2.4$, an orbital triplet, $^4T_{2g}$, formed from the $t_{2g}^2 e_g$ configuration is the lowest lying excited state. Since the e_g orbital points towards the nearby ligand ions, the $^4T_{2g}$ state is strongly coupled to lattice vibrations and the $^4T_{2g} \rightarrow {}^4A_{2g}$ transition emits in a broad band which is Stokes-shifted into the near infra-red region from the corresponding absorption band. In strong crystal fields, $Dq\ /\ B \geq 2.4$, the ^2E_g level, formed from the t^3_{2g}

configuration, lies lower than the $^4T_{2g}$ level. Since ^2E_g is weakly coupled to the phonon spectrum of the crystal the $^2E_g \rightarrow {}^4A_{2g}$ emission occurs mainly in the sharp zero-phonon R-lines and the associated vibronic sidebands [106, 111].

A. Katelnikovas et al. in 2011 demonstrated that the sol-gel preparation of garnet type $Y_{3-x}Lu_xAl_3MgSiO_{12}$ powders garnets, in which Al^{3+}–Al^{3+} pair was replaced by Mg^{2+}–Si^{4+} pair. Single phase target materials were obtained just after sintering the precursor powders at 1600 °C. It was shown that sintered powders do not absorb radiation above 320 nm (Fig. 6) [112].

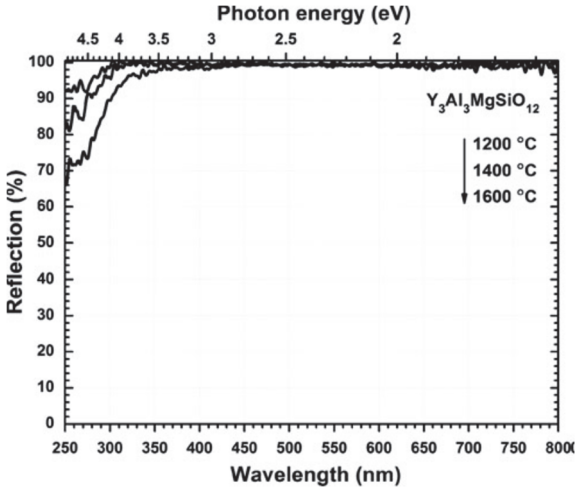

Fig. 6. Reflection spectra of $Y_3Al_3MgSiO_{12}$ powders as a function of sintering temperature.

Therefore, these materials doped with rare earths or other optically active ions were suggested as the potential candidates for solid state lasers, phosphors, and scintillators. Indeed, Ce^{3+}-doped $Y_{3-x}Lu_xAl_3MgSiO_{12}$ samples synthesized by an aqueous sol-gel method possessed red-shifted emission in comparison with commercial YAG:Ce phosphors, enabling to obtain warmer white LED light sources [113].

It was also demonstrated that garnets are suitable host lattices for investigating the impact of crystal field strength, disorder and covalent interaction on the luminescence of an incorporated luminescent centre, as for instance Pr^{3+} [114]. It turned out that changing the composition of the garnets $Lu_3(Ga,Al)_5O_{12}$ and $(Y,Lu)_3(Al,Mg,Si)_5O_{12}$ was a powerful tool to govern the energy flow from the primarily excited state of the $[Xe]4f^2$ or $[Xe]4f^15d^1$

configuration to lower energy levels of the [Xe]$4f^2$ configuration. Therefore, the luminescence spectra of Pr^{3+} doped garnets were adjusted by tuning the host lattice to yield solely UV band emission, visible line emission, or both.

Later it was shown that the luminescent materials with the nominal chemical composition of $CaLu_2Al_4SiO_{12}:Ce^{3+}$ are efficient colour converters for inorganic light emitting diodes [12]. Their emission band position is blue shifted in comparison to $Lu_3Al_5O_{12}:Ce^{3+}$. Besides, the emission properties are very sensitive to variations of the Ce^{3+} concentration. With increasing Ce^{3+} concentration from 0.1 to 3.0 mol% the emission maximum shifts from 520 to 542 nm (see Fig. 7). This is probably caused by re-absorption process (an emitted photon is again absorbed by activator due to overlapping absorption and emission bands).

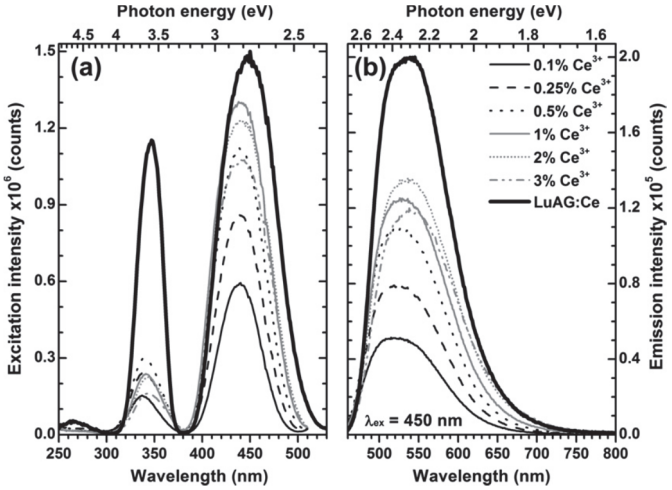

Fig. 7. Excitation (a) and emission (b) spectra of $CaLu_2Al_4SiO_{12}:Ce^{3+}$ powders sintered at 1400 °C as a function of Ce^{3+} concentration.

The $CaY_2Al_4SiO_{12}:Ce^{3+}$ phosphors were found to be efficient colour converters for solid state light sources. The emission band of these Ce^{3+} doped garnets was also blue-shifted in comparison to YAG:Ce [15].

A series of single phase samples of europium comprising YAG–YGG, LuAG–LuGG, YGG–GGG garnets were prepared and characterized [115]. It was demonstrated that under 160 nm excitation the $^5D_0$-$^7F^4$ transitions were dominant (680 – 720 nm wavelength range). It turned out that the intensity ratio $^5D_0$-$^7F_4$/$^5D_0$-^7F_J clearly depends on the chemical composition of the host

matrix. An increase of the average electronegativity (EN) of the trivalent cations, which means a decreasing optical basicity, in the octahedral and tetrahedral sites in the garnet structure caused an increase of the intensity ratio. Therefore, the emission of the $^5D_0$–$^7F_4$ transitions increased with the decrease of electronegativity as it is demonstrated in Fig. 8.

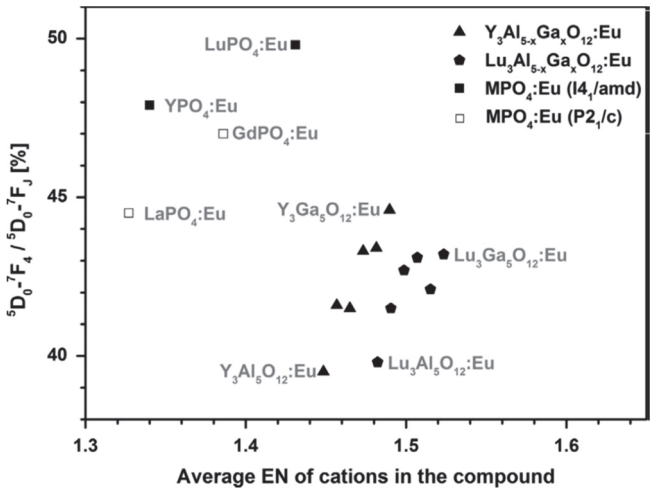

Fig. 8. The ratio of $^5D_0$-$^7F_4$/$^5D_0$-^7F_J as a function of the average EN values of all cations in the host matrix.

Therefore, in order to improve the lumen equivalent of given phosphors, the optical basicity of the compound should be increased by using dopants or solid solutions. The opposite effect thus can be achieved by decreasing the average electronegativity of the cations.

The efficient far-red phosphors are desired for artificial lighting in greenhouses for plant cultivation, which is an important technology since it enables to grow plants during any time of a year at any latitude [116, 117].

1.2. $M_3MgSi_2O_8$ Compounds

$M_3MgSi_2O_8$ (M = Ba, Sr and Ca) compounds have attracted attention of scientists as promising host materials for Eu^{2+}-doped blue phosphors. The improvement of intensity and chromaticity has been investigated by deeper analysis and understanding of emission mechanism [118]. The first known and the most famous member of this group is merwinite, $Ca_3MgSi_2O_8$, described by Larsen and Foshag in 1921. As an important and persistent phase in

petrological systems it was crucial to mantle and crustal chemistry and to the cement and blast furnace industries [119]. After G. Blasse et al. [20] listed $M_3MgSi_2O_8$ compounds as very efficient host materials for the Eu^{2+} ions under UV excitation, the studies of $M_3MgSi_2O_8$ mainly been focussed on their luminesce properties. Despite the great importance of merwinite and the many articles on the subject, the crystal structure of these compounds were indexed and published with some mistakes much later, which were recently solved [118, 120-123]. As the luminescence properties of Eu^{2+} are highly sensitive to its local environment, the establishment of $M_3MgSi_2O_8$ correct crystal structures is essential [124].

1.2.1. Crystal Structures of $M_3MgSi_2O_8$ Compounds

Despite numerous studies on crystal structures of materials with a chemical formula $M_3MgSi_2O_8$, including merwinite, there are erroneous in various details published up to date. Larsen and Foshag were first described merwinite, $Ca_3Mg(SiO_4)_2$, in 1921, as a major component of a high grade metamorphic contact rock from the famous quarries at Crestmore, near Riverside, California. Notwithstanding the great attention to merwinite type materials P. B. Moore and T. Araki correctly indexed crystal structure just on 1972 [119]. The merwinite, with unit formula $Ca_3MgSi_2O_8$ belongs to monoclinic crystal system, which has space group - $P2_1/c$ (no. = 14) (Fig. 9). Crystal cell parameters *a*, *b* and *c* are respectively 9.328 Å, 5.293 Å and 13.254 Å, $\alpha = \gamma = 90°$ and $\beta = 91.9°$.

The atomic arrangement possesses a substructure of pseudo-hexagonal character, whose axes are parallel to [010], [011], and $[01\bar{1}]$. Crystals are often highly distorted with frequent prismatic development along [011] or $[01\bar{1}]$. The atomic structure is an extreme example of dense-packing, where both O^{2-} and Ca^{2+} ions comprise the dense-packed layers. The $[MgO_6]$ octahedra are linked at every corner by $[SiO_4]$ tetrahedra, defining a "pinwheel" of $\bar{3}$m, point pseudosymmetry. These polyhedra share only corners with each other so that the violent cation-cation repulsion effects are minimized. Most exciting is

Nature's way of increasing coordination number of cations without sacrificing crystallographic dense-packing. In merwinite, this is achieved by mixing of cations and anions in the dense packed layers. Structures of this kind tend to appear in abundance at high pressures [119]. A Fig. 9 presents merwinite's, $Ca_3MgSi_2O_8$, crystal structure, where O^{2-} ions are red balls, Si^{4+} - blue, Mg^{2+} - orange and Ca^{2+} ions in dislocations Ca(I), Ca(II) and Ca(III) - cyan, purple and wine respectively.

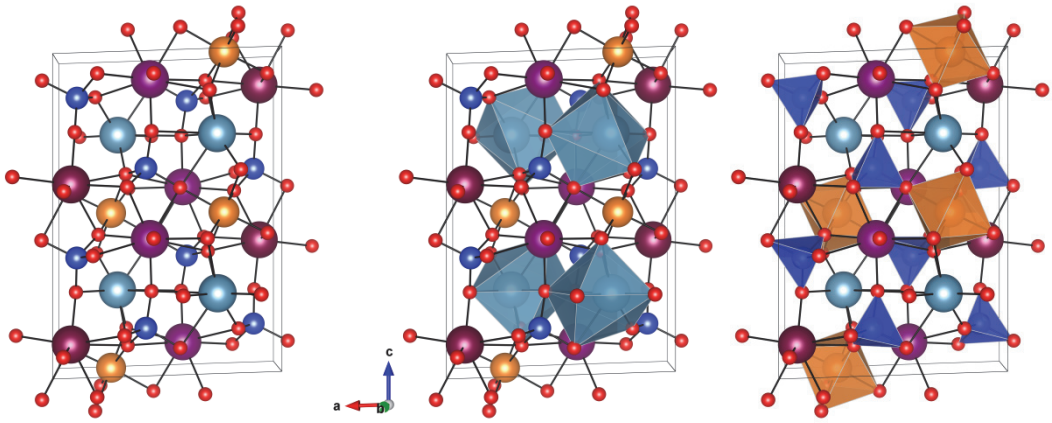

Fig. 9. Crystal structure of merwinite, $Ca_3MgSi_2O_8$, unit cells are oriented same. Polyhedrons of Ca^{2+} at Ca(I) dislocation (interlayer) presented in the centre picture and right picture presents Mg^{2+} octahedrons and Si^{4+} tetrahedrons. Pictures are drawn with VESTA program.

The geometrically idealized merwinite arrangement includes Ca(I) in 12-coordination by O^{2-} anions (A-site) defining a polyhedron with point pseudo-symmetry $\bar{3}$m, Ca(II) and Ca(III) each in l0-coordination (B-site) whose polyhedra have point pseudo-symmetry 3m. All prismatic crystals rotated about the prism axis revealed a triclinic "pseudo-orthohexagonal" geometry. This prism axis corresponds to either the [011] or the [01$\bar{1}$] directions of the true merwinite cell. Its idealized arrangement is the glaserite type structure [119].

As promising host materials for transition-metal activated phosphors $M_3MgSi_2O_8$ (M: Ba^{2+}, Sr^{2+} and Ca^{2+}) orthosilicates have attracted much attention. After T. L. Barry [125, 126] and G. Blasse et al. [20] in 1968 reported great luminescence properties of this type phosphors, especially Eu^{2+}-

doped $Ba_3MgSi_2O_8$, studies increased extensively [118, 122, 127]. For a long time (over 40 years) the emission properties were discussed on the assumption that all $M_3MgSi_2O_8$ compounds had merwinite type ($Ca_3MgSi_2O_8$) structure with monoclinic symmetry [125, 128-134]. However, a variation of the crystal structure appears by the change of M^{2+} ions in the compounds. In addition, just very recently crystal structures of all variations $(Ca^{2+}/Sr^{2+}/Ba^{2+})_3Mg(SiO_4)_2$ were correctly indexed and published [118, 120, 122-124, 135]. The space group of $M_3MgSi_2O_8$ changes depending on the average size of cations at A-site (like Ca(I) in merwinite). Also it has been reported that B-site cations (in merwinite Ca(II) and Ca(III)) also cause layer deformation associated with SiO_4 twisting around threefold rotation axis [122-124], see Fig. 10. In a Table 4 there are summarized space groups and cell parameters of $M_3MgSi_2O_8$ ($M^{2+} = Ca^{2+}/Sr^{2+}/Ba^{2+}$) compounds corresponding to the change of M^{2+} cations.

Table 4. $M_3MgSi_2O_8$ ($M^{2+} = Ca^{2+}/Sr^{2+}/Ba^{2+}$) compounds space groups and cell parameters.

M_3^{2+}	x =	Space group (no.)	Cell parameters					Ref.
			a (Å)	b (Å)	c (Å)	β (°)	V (Å^3)	
Ca_3		$P2_1/c$ (14)	13.254(21); 13.296(3)	5.293(9); 5.308(12)	9.328(17); 9.346(2)	91.90(15); 92.047(14)	659.3(3)	[118, 119]
$Ca_{3-x}Sr_x$	1	A2 (5)	13.415(2)	5.349(10)	9.345(17)	90.00668(9)	679.6(2)	[118]
Sr_3		C2 (5)	9.449(3)	5.453(1)	13.871(4)	90.153(2)	714.9(3)	[123]
$Ca_{3-x}Ba_x$	1	$P\bar{3}$ (147)	5.4265(7); 5.42708(5)	-	6.79455(7); 6.8005(6)	-	173.310(4); 173.42(3)	[122, 124]
Ba_3		$P\bar{3}$ (147)	9.7180(7)	-	7.2715(4)	-	594.72(7)	[123, 135]
$Ba_{3-x}Sr_x$	$0.5 \leq x$	$P\bar{3}$ (147)	9.7180(7) - 9.666(2)	-	7.2715(4) - 7.2076(9)	-	594.72(7) - 583.2(2)	[118, 122, 123]
	$0.5 < x < 2.5$	$P\bar{3}m1$ (164)	5.573(1) - 5.4840(8)	-	7.1909(9) - 6.9806(8)	-	193.46(5) - 181.81(4)	
	$2.5 \leq x$	C2 (5)	9.485(1) - 9.449(3)	5.4765(6) - 5.453(1)	13.931(1) - 13.871(4)	90.011(6) - 90.153(2)	723.7(1) - 714.9(3)	
$BaCa_{2-x}Sr_x$	$0 \leq x < 1$	$P\bar{3}$ (147)	5.4265(1) - 5.4585(9)	-	6.8005(6) - 6.8972(8)	-	173.42(3) - 177.97(5)	[118, 121, 122]
	$1 \leq x \leq 2$	$P\bar{3}m1$ (164)	5.4585(9) - 5.4942(6)	-	6.8972(8) - 7.0115(6)	-	177.97(5) - 183.29(3)	

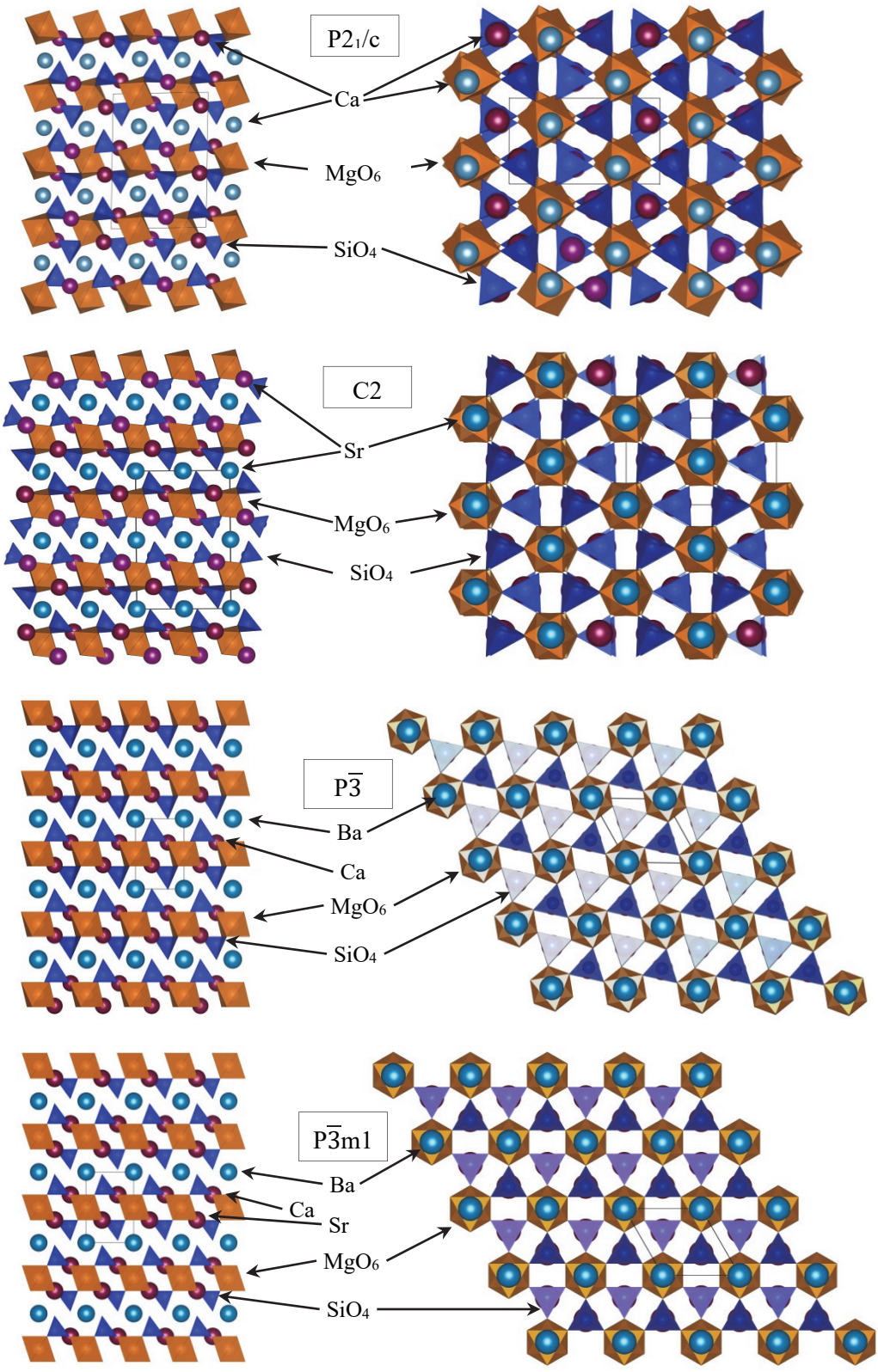

Fig. 10. Structural views of $Ca_3MgSi_2O_8$ (space group (s. g.) $P2_1/c$), $Sr_3MgSi_2O_8$ (s. g. C2), $BaCa_2MgSi_2O_8$ (s.g. $P\bar{3}$) and $BaCaSrMgSi_2O_8$ (s.g. $P\bar{3}m1$). The solid line frames indicate the unit cells of each structure. Pictures are drawn with VESTA program.

Depending on the molar ratio of Ba^{2+}, Sr^{2+} and Ca^{2+} in M^{2+} of the $M_3MgSi_2O_8$ several crystal structures (monoclinic $P2_1/c$, C2 and trigonal $P\bar{3}$, $P\bar{3}m1$) are confirmed by referees given at Table 4. Theses crystal structures were successfully refined using glaserite-type structure models, nevertheless classical XRD Rietveld refinement method was not accurate enough, so was combined with neutron diffraction and Raman spectroscopy [120, 123, 124]. All these structures belong to glaserite-type and have layered structures (Fig. 10). The structural pictures placed one next to another, however, highlights some differences. Here orange octahedrons present [MgO_6] and blue tetrahedrons – [SiO_4], cyan, purple and wine circles represents M^{2+} cations.

There are two distinct crystallographic sites for alkali earth metal atoms, the interlayer site (A-site, cyan atoms in Fig. 10) sandwiched in between two triangular faces of MgO_6 octahedra and the layer-embedded site (B-site, purple and wine circles in Fig. 10) surrounded by three MgO_6 octahedra and four SiO_4 tetrahedra [127]. They create a SiO_4 tilting caused by size mismatch between alkali-earth cations and their site spaces. The A-site is preferentially occupied by Ba^{2+} ion while B-site by Sr^{2+}/Ca^{2+} ions. The substitution of Sr leads to the average-size enlargement of B-site cations and causes layer deformation, consequently crystal structure changes not directly to $P\bar{3}$, but through $P\bar{3}m1$ [122]. As an important aspect is that for the limiting case of Sr^{2+} cation ($Sr_3MgSi_2O_8$), structure model C2 refinement's parameter R_{wp} is still large and considering the Raman spectra, $Sr_3MgSi_2O_8$ may have a lower-symmetry structure [123].

Hence, $M_3MgSi_2O_8$ compounds were revised several times already, but still some corrections may appear in the future. Since these compounds are widely used as phosphors the precise structure analyses are required in order to understand the spectroscopic character of luminescent centres, which are strongly affected by the crystal-field strength and site symmetry [123, 136].

1.2.2. Main and Possible Application

The fluorescence of Eu^{2+}-activated binary and ternary silicates has been studied for years, because alkaline earth silicates are appropriate luminescent hosts with stable crystal structure, high physical and chemical stability [128]. Consequently, silicates are very suitable for the solid-state lighting (SSL). They find application in fluorescent lamps, cathode ray tubes, plasma displays and as scintillators. $M_3MgSi_2O_8$ (M: Ba, Sr, Ca) phosphors have been established basically as host materials for Eu^{2+}-activated blue-emitting phosphors [137].

The Eu^{2+}-activated $M_3MgSi_2O_8$ (M: Ba, Sr, Ca) were marked from the list of other silicates as most efficient blue phosphor by G. Blasse and co-workers [20, 138]. Their studies on the photoluminescence (PL) properties of these compounds leaded to the hypothesis that a systematic decrease of peak emission wavelength depending on the M cation size. In the same year T. L. Barry published [125, 126] on mixtures of Eu^{2+}-activated $Ba_3MgSi_2O_8$, $Sr_3MgSi_2O_8$ and $Ca_3MgSi_2O_8$, that $Ba_3MgSi_2O_8$ has the highest PL emission intensity and shortest emission wavelength (437 nm) and $Ca_3MgSi_2O_8$ - the lowest intensity and longest peak emission wavelength (475 nm), $Sr_3MgSi_2O_8$ falling in between those two (458 nm). T. L. Barry outlined an interesting potential application at that time that these phosphors co-activated with manganese might be used for plant cultivation lighting. Such phosphors produce two distinct emission bands, which conform fairly well to the action spectra of chlorophyll synthesis and photosynthesis. Either T. L. Barry published that $Sr_3MgSi_2O_8$ forms ideal solid solutions with both $Ba_3MgSi_2O_8$ and $Ca_3MgSi_2O_8$, but $Ba_3MgSi_2O_8$ and $Ca_3MgSi_2O_8$ does not, leading to an intermediate compound, $BaCa_2Si_2O_8$. However, the correct crystal structures of possible mixtures of $M_3MgSi_2O_8$ (M: Ba, Sr, Ca) were indexed and published elsewhere much later and discussed in previous section.

Many other scientific groups were analysing luminescent properties of different combinations of Eu^{2+}-activated $M_3MgSi_2O_8$ (M: Ba, Sr, and Ca) [121, 122, 130, 134, 139-141]. In summary, the peak wavelength of the emission

originated in 5d–4f electron transition strongly depends on the crystal-field experienced by Eu^{2+} ions, so the crucial aspect for PL of these compounds is peculiarities of crystal structure. Under vacuum-UV-light excitation (146 nm) $Sr_{2.98}MgSi_2O_8:0.02Eu^{2+}$ and $Sr_{2.48}Ba_{0.5}MgSi_2O_8:0.02Eu^{2+}$ photoluminescence peak intensities are over 90 and 75%, respectively, as high as commercially used $BaMgAl_{10}O_{17}:Eu^{2+}$ (BAM). Moreover, thermal luminescence degradation and the brightness after annealing at 500 °C are much smaller of $(Sr/Ba)_3MgSi_2O_8:Eu^{2+}$ than BAM. The thermal degradation of luminescence is mainly attributed to the thermal oxidation of Eu^{2+} to Eu^{3+}. Ba substitution in $Sr_3MgSi_2O_8$ compounds plays an important role for suppressing the oxidation. With the increase of Ba content in the composition, the emission spectrum was blue-shifted, indicating a central wavelength-tunable blue phosphor. The optimized composition for highly luminous phosphor is $Ca_{0.9}Sr_{0.45}Ba_{1.65}MgSi_2O_8:Eu^{2+}$, which has about 170% enhancement in the integrated emission intensity compared with the $Sr_3MgSi_2O_8:Eu^{2+}$ phosphor. The latest research on $Ba_{2.98}Eu_{0.02}MgSi_2O_8$ successfully explained phenomena of the emission colour switching between blue and purple by laser irradiation. From the experiments on the samples prepared under different reducing conditions, surprisingly it has been found that the amount of the red emission centre was not dependent on the Eu^{2+}-amount [142].

The red (620 nm), green (505 nm) and blue (442 nm) emissions were simultaneously observed from Eu^{2+} and Mn^{2+} co-activated $Ba_3MgSi_2O_8$, which led to a single-phase full-colour (RGB) phosphor [143]. However, the green light originated by $Ba_2SiO_4:Eu^{2+}$ which appeared as an impurity phase [134, 137]. The $Ba_3MgSi_2O_8:Eu^{2+}$, Mn^{2+} should emit in purple, because the blue emission from Eu^{2+} ions mixes with the red emission from Mn^{2+} ions. It is explained that a part of excitation energy resonantly transferred from Eu^{2+} to Mn^{2+} ions, leading to its red emission. Consequently $(Ba, Ca, Sr)_3MgSi_2O_8:Eu^{2+}, Mn^{2+}$ phosphors, emitting blue, red and even far-red light, combined with a near-ultraviolet LED chip might be successively used for plant cultivation. Importantly, light quality (the emission spectra:

broad blue-emission band (450 – 485 nm), red-emission band (620 – 703 nm) and quantum efficiencies (between 45 – 70%)), could be adjusted by tuning the elemental composition of these phosphors. That enables to tailor the optimal spectrum requirements for different species of plants [133, 137, 144, 145].

Nevertheless, it was found that Tb^{3+}, Eu^{2+} and Mn^{2+} co-activated $Ba_3MgSi_2O_8$ exhibits tri-band (red, green and blue) emission due to the dopant ions. The obtained light is a cool white light and the solubility of Tb^{3+} limits to get warmer colour. These phosphors have a big potential as full-colour phosphors for applications in solid-state white lighting devices, but the quantum yield and temperature-stability should be improved [146]. Y. Chen et al. [147] published that $Sr_3MgSi_2O_8:Ce^{3+},Tb^{3+}$ has potential as near ultraviolet region based wavelength-tunable single-phase phosphor for white LEDs. $Sr_{2.75}MgSi_2O_8:0.01Ce^{3+}$, $0.015Tb^{3+}$ under ultraviolet light (330 nm) excitation presents blue emission, as the luminous colour shifted from bluish violet ($Sr_3MgSi_2O_8:Ce^{3+}$). According Y. Yonesaki el al. [148] Mn^{2+} ions doped into $M_2BaMgSi_2O_8$ show bright red emission if Ce^{3+} ions are added together. The increase of intensity is obtained because of structural distortion around Mn^{2+} ions caused by Ba-addition. The Förster resonance energy transfer from Ce^{3+} to Mn^{2+} plays an important role for the Mn^{2+} emission. As Ce^{3+}-derived emission is almost invisible to the naked eye, emission from Ce^{3+}, Mn^{2+}-doped $M_2BaMgSi_2O_8$ appears totally red.

The $M_3MgSi_2O_8$ co-activated with Eu^{2+} and Dy^{3+} attracted attention as long lasting phosphors (LLP). LLP materials can be widely used in areas such as safety indication and emergency lighting. Y. Lin et al. [149] detected long afterglow (over 5 h in the limit of the light perception of the dark-adapted human eye) of $Ca_3MgSi_2O_8:Eu^{2+}, Dy^{3+}$ phosphor with high brightness. Y. H. Lin et al. [128] found that $Sr_3MgSi_2O_8$ phosphor has better afterglow properties than the other $M_3MgSi_2O_8:Eu^{2+}, Dy^{3+}$ (M: Ca, Sr, Ba) phosphors. A. A. S. Alvani et al [129] after systematic studies of concentration effect to afterglow suggested luminescent mechanism in $Sr_3MgSi_2O_8:Eu^{2+}, Dy^{3+}$ phosphor. In the class of $M_3MgSi_2O_8$, Sr has a superior position among

alkaline earth metals. The synthesized phosphors have two broad excitation bands cantered at 356 and 395 nm. The main emission peak is seen at 482 nm (typical emission of Eu^{2+} ascribed to the $4f^7 \rightarrow 4f^6 5d^1$ transition), its afterglow lasts for more than 10 h.

It was presented to use the LLPs in radiation detection, sensors for structural damage, fracture of materials, and temperature. They are called the third generation LLPs. The alkaline silicates are superior to aluminates as host materials for such applications. As the colours of the commercial LLPs are still limited to blue ($CaAl_2O_4:Eu^{2+}$, Nd^{3+}) and yellow–green ($SrAl_2O_4:Eu^{2+}$, Dy^{3+}), the red-light LLPs is missing for the tricolour. Consequently Y. Gong el al. [150] suggest to use $Sr_3MgSi_2O_8:Eu^{2+}$, Mn^{2+}, Dy^{3+}. They demonstrated that the weak red emission resulting from the forbidden transition of Mn^{2+} could be enhanced by the energy transfer from Eu^{2+} and the emission duration can be prolonged to more than 2 h. The thermo-luminescence spectra were used to characterize the ability of the trap to trapping the carriers. By the analysis of the ionization potentials, the roles of Mn^{2+} and Dy^{3+} in the afterglow process were discussed [150].

Among the crystals containing BX_4 (SO_4, SeO_4, CrO_4) tetrahedrons, described by the formulas A_2BX_4, $ACBX_4$, and $A_3C(BX_4)_2$, where A, C = Li, Na, K, Rb, Cs, NH_4 there is a large group of materials that show an interesting sequence of phase transitions and the appearance of ferroic phases as a consequence of spatial ordering of BX_4 groups. Glaserite-type oxides fall into this list, e.g. $K_3Na(CrO_4)_2$ exhibits a ferroelastic phase transition at about 239 K [151]. $K_3Na(SeO_4)_2$, and $K_3Na(MoO_4)_2$, have been intensively studied as well because their ferroelastic character closely relates to the structural symmetry [123, 152].

Bulk crystals are inherently three-dimensional, however, they may comprise magnetic ions whose spins interact only along a certain crystallographic planes. Such compounds are called two-dimensional (2D) magnets. For small spin values, for example, S = 1/2 (as in Cu^{2+} or (low spin) Co^{2+}) or S = 1 (as in Ni^{2+}), quantum effects play a prominent role [153].

Researchers [154] reported the first truly 2D magnet made of a compound called chromium triiodide. The discovery could eventually lead to new data-storage devices and designs for quantum computers. For now, the 2D magnets will enable physicists to perform previously impossible experiments and test fundamental theories of magnetism [153]. In a crystalline electric field of such low symmetry, the orbitally degenerated $3d^9$ level of a free Cu^{2+} ion splits into four sublevels. The orbital $e_g(dx^2\text{-}y^2)$, which experiences the maximum electrostatic repulsion from the surrounding ligand ions, constitutes the highest energy level with exactly one electron per orbital, which results in a S = 1/2 chain parallel to the crystallographic axis (e.g. c-axis). The absence of intervening oxygen ions or the presence of buffer layers of magnetically inactive atoms (like Sr^{2+}) along other axes (e.g. a-axis and b-axis) secures magnetic isolation and hence the magnetic 1D nature of the compound [155]. If compounds based on $M_3MgSi_2O_8$ structures could serve as model for new materials, in which the doped triangular lattice could be studied, that would be a major breakthrough. A wide range of different lattice geometries and dimensionalities is available for further study. In combination with the large number of experimental probes for spins, this enables us to enter the world of exotic phases of strongly interacting quantum particles such as the Bose-Einstein condensation (BEC) in various dimensions, Luttinger-liquid physics, commensurate solids with a fractional number of bosons per unit cell and supersolids combining superfluidity with a broken translational symmetry [156].

Another layered structure silicate $BaCuSi_2O_6$ is known as Han purple, a pigment already used by Chinese artistes centuries ago. $BaCuSi_2O_6$ is a quasi-two-dimensional spin dimer system and a model material for studying BEC of magnons in high magnetic fields. Studies have shown that it is a quasi-two-dimensional spin dimer system. The crystal structure of $BaCuSi_2O_6$ at room temperature is tetragonal ($I4_1/acd$) and launches CuO_4 layers, which are retained on their edges with SiO_4 tetrahedra. The layers are linked in pairs, that the distance between two Cu atoms is only 2.75 Å. These bilayers form

well-defined structural and magnetic dimers and are separated from each other through Ba^{2+} cations. Each spin 1/2 Cu^{2+} ion interacts with the four Cu^{2+} ions of the next layer. The interlayer coupling of the bilayers is antiferromagnetic (below 1 K), and a perfect frustration may be realized [157, 158].

These phenomenal studies require of advanced experimental methods, like neutron scattering and high-precision magnetometry and calorimetry. However, they are very limited, because of difficulties to produce large quantities of high-quality samples (single crystals). The success of this approach is standing on advances in growth techniques, present state of knowledge and a collective effort across several areas of expertise, including materials science and chemistry, which may enable us to study in the future.

1.2.3. Synthesis Methods of $M_3MgSi_2O_8$

The choice of good synthesis pathways and correct, optimized fabrication conditions is the ultimate step to prepare single-phase material. For example, wrong synthesis produced wrong hypothesis and explanation that $Ba_3MgSi_2O_8:Eu^{2+}$, Mn^{2+} emits blue, red and green light, showing a perspective for applications in full colour white light LED. However, the synthesis conditions were not optimal and appeared impurity Ba_2SiO_4 causing green emission [134]. The most of published research on $M_3MgSi_2O_8$ compound were done on the samples prepared by solid-state reactions. Other synthesis methods, like sol-gel, sol-gel combustion, spray pyrolysis and mixed/combined methods were also used for the improvement of quality of powdered samples.

Conventional solid-state reaction was employed for the preparation of samples of batch compositions $M_3MgSi_2O_8$ (M: Ca, Sr and Ba) and doped with Eu^{2+}, Mn^{2+}, Dy^{3+} and etc. Alkaline-earth carbonates ($CaCO_3$, $SrCO_3$ and $BaCO_3$), magnesium oxides (MgO) or carbonate hydroxide ($4MgCO_3{\cdot}Mg(OH)_2{\cdot}5H_2O$) and silica ($SiO_2$) or silica gel starting materials used in the synthesis are most common. Prior to use pieces of SiO_2 it has to be ground into a fine powder. Eu_2O_3, Dy_2O_3, $Mn(CH_3COO)_2{\cdot}6H_2O$ or MnO_2 and $Ce(OH)_4$ are used as raw materials for doping the matrixes. A small amount of

NH_4Cl (about 2 wt%) or H_3BO_3 (about 5 mol%) are often used as fluxes. Stoichiometric amounts of the reagents and the flux are ground and mixed by ball milling with zirconia beads for 4 – 6 h or using agate mortar in 2-propanol or ethanol. The mixed powder are heated at 1100 – 1350 °C for 3 – 15 h in air or if it is necessary in the reducing atmosphere (the mixture of 5% H_2 and 95% N_2), sometimes with an intermediate regrinding [118, 121, 123, 124, 127-129, 134, 139, 148, 150].

The single phase $Ba_3MgSi_2O_8$ powders were obtained only using $LiBO_2$, Li_2CO_3 and Na_2CO_3 as fluxes [120]. P. Zhang et al. [141] discussed the role of flux on phase formation and luminescence for a series of $M_3MgSi_2O_8:Eu^{2+}$ (M: Ca, Sr, Ba) phosphors synthesized by conventional solid-state reaction method. They found that the best flux for the synthesis of $Sr_3MgSi_2O_8:Eu^{2+}$ is NH_4Cl (~7.5 wt%), an alternative choice is AlF_3 (~5.0 wt%) and the fluxes NaCl or KBr almost do not affect the luminescence. However, H_3BO_3 has a negative effect on luminescence, especially when doping concentrations are high.

In order to reduce synthesis temperature, to control particle size and morphology the sol-gel, sol-gel combustion and microwave-assisted sol-gel syntheses are employed. The microwave-assisted sol-gel method have been used in order to get $Ba_3Mg_{1-x}Li_xSi_2O_8$:Eu,Tb single phase samples [146]. In to a solution formed of water and ethanol (pH = 2 – 3 reached by addition of glacial acetic acid) a citric acid was added. Then, stoichiometric amounts of $BaCO_3$, $Mg(NO_3)_2{\cdot}6H_2O$, tetraethoxysilane (TEOS), $Tb(NO_3)_3{\cdot}5H_2O$, $Eu(NO_3)_3{\cdot}5H_2O$, $MnCO_3$ and Li_2CO_3 were dissolved. The obtained solution was evaporated and transparent gel was formed. This gel was dried and finely ground. The samples were heated at 400 °C for 4 h and then at 650 °C for 6 h. The final product is obtained after heat-treatment in a microwave setup. The authors claim that a rapid microwave heating prevents formation of impurity phases in comparison with conventional furnace heating.

$M_3MgSi_2O_8$:Eu, Mn (M: Ba, Ca, Sr) phosphors were synthesized also via combustion synthesis [137]. Metal nitrides and fumed SiO_2 were used as

starting materials for the synthesis and carbohydrazide (CH_6N_4O) was used as the fuel. After final heating for 6 h at 1200 °C in a reductive atmosphere microcrystalline powders were obtained, the particle size is in the range of 0.3 – 1 μm. However, the secondary phases formed in the preparation of $Ba_3MgSi_2O_8$:Eu, Mn.

An interesting combination of solid-state and sol-gel combustion syntheses were described by W. Ahn el al. [159]. The process was significantly shortened compared with a sol-gel method. In order to get a single-phase $(Sr, Ba)_3MgSi_2O_8$:Eu using this sol-gel combustion hybrid process they used highly soluble strontium and barium acetates, colloidal silica and TEOS. Acetic acid was used as catalyst for the combustion reaction and NH_4Cl was used as a flux. The NH_4Cl was mixed with the black powders obtained after combustion process and calcined at 1000 °C for 3 h, then ground and fired at 1300 °C for 5 h under reductive atmosphere. The addition of flux resulted in the formation of a single phase product.

The last reviewed method is spray-pyrolysis which is used to produce $M_3MgSi_2O_8$:Eu, Mn phosphor. The metal nitrates were dissolved in water with addition of $C_4H_6MnO_4 \cdot 4H_2O$ and TEOS. The final solution was sprayed by an atomizer to obtain xerogel particles. The xerogels are heated in a tube furnace for ~3 h or in a tubular reactor at 1200 – 1400 °C under a reducing atmosphere [140, 144]. L. Wang et al. [160] reported the newly observed evolution and control of morphology of the compound fabricated by spray-pyrolysis synthesis procedure with using instant microwave firing hollow xerogel particles. Authors produced cage-like morphology of $(Ba,Sr)_3MgSi_2O_8:Eu^{2+},Mn^{2+}$ powders. The particles with cage-like morphology could be used to construct the multi-scale, one-component phosphor particles in meso-, nano- and submicro- meter to achieve the photoluminescence enhancement.

2. EXPERIMENTAL PART

2.1. Reagents

Tris-(hydroxymethyl)-aminomethane (TRIS) ($NH_2C(CH_2OH)_3$; 99.9%; Carl Roth) and 1,2-ethanediol ($C_2H_6O_2$; 99.5%; Scharlau and 99.8%; Sigma-Aldrich) were used as complexing agents in the sol-gel processing. Metal oxides were dissolved in concentrated nitric acid (HNO_3; 65%; Reachem and 70%; Sigma-Aldrich). Ammonium chloride (NH_4Cl; 99.999%; Carl-Roth) was used as a flux in soli-state reaction syntheses. Gadolinium (III) oxide (Gd_2O_3; 99.99%; Treibacher Industrie AG), gadolinium nitrate x-hydrate ($Gd(NO_3)_3 \cdot xH_2O$ ($x \approx 6$; 99.9%; Alfa Aesar), scandium oxide (Sc_2O_3; 99.99%; Treibacher Industrie AG), gallium oxide (Ga_2O_3; 99.99%; Alfa Aesar), yttrium oxide (Y_2O_3; 99.99%; Alfa Aesar), lutetium oxide (Lu_2O_3; 99.99%; Treibacher Industrie AG), iron (III) nitrate nonahytrate ($Fe(NO_3)_3 \cdot 9H_2O$; 99.9%; Sigma-Aldrich), chromium (III) nitrate nonahydrate ($Cr(NO_3)_3 \cdot 9H_2O$; 99%; Sigma-Aldrich), diammonium cerium (IV) nitrate ($(NH_4)_2Ce(NO_3)_6$; 99.9%; Carl Roth), calcium carbonate ($CaCO_3$; 99.999%; Sigma-Aldrich), barium carbonate ($BaCO_3$; 99.999%; CERAO), barium peroxide (BaO_2; 99%; 80 mesh; CERAO), copper (II) oxide (CuO; 99.999%; CERAO), dicopper carbonate dihydroxide ($Cu_2(OH)_2CO_3$; ≥95%; Carl Roth), magnesium nitrate hexahydrate ($Mg(NO_3)_2 \cdot 6H_2O$; 99.999%; Sigma-Aldrich), magnesium carbonate dihydroxide heptahydrate ($4MgCO_3 \cdot Mg(OH)_2 \cdot 5H_2O$; 98%; Carl Roth), silicon dioxide nanopowders (SiO_2 np.; particle size 10 – 20 nm; 99.5%; Sigma-Aldrich) and silica (SiO_2; 99.9%; grain 0.2 – 0.7mm; BALZERS) were used as starting materials.

2.2. Synthesis Methods of Garnets

In the sol-gel processing of $Gd_3Sc_2Ga_3O_{12}$ (GSGG) garnet three slightly different synthesis routes were used. In the syntheses I and II, the 1,2-ethanediol has been selected as complexing agent, while TRIS was used in the synthesis III. The molar ratio of complexing agents to all metal ions was ~1:2 for both the glycolate gels and gels with TRIS. For the preparation of

GSGG in the synthesis I gadolinium nitrate, scandium and gallium oxides were used as starting materials. Firstly, the stoichiometric amounts of Sc_2O_3 and Ga_2O_3 were dissolved in boiling concentrated nitric acid. The acidity of these solutions was reduced by evaporating them and diluting with distilled water for 3 times. Secondly, the obtained $Ga(NO_3)_3$ and $Sc(NO_3)_3$ solutions were mixed with the appropriate amount of $Gd(NO_3)_3 \cdot 6H_2O$ dissolved in distilled water. The amount of water of crystallization in $Gd(NO_3)_3 \cdot 6H_2O$ was estimated by employing TG analysis. Finally, the complexing agent 1,2-ethanediol was added to the above solution containing Gd^{3+}, Sc^{3+} and Ga^{3+} ions. The obtained solution was continuously mixed for 1 h using a magnetic stirrer at 65 – 70 °C. When transparent sol has formed the solvent was slowly evaporated and viscous Gd-Sc-Ga-O gel has formed. The dried gel was thoroughly ground in agate mortar and heated at 800 °C for 5 h using the heating rate of 1 °C/min. The obtained powders after repeated grinding were additionally heated for 10 h at 1000 °C using the heating rate of 3 °C/min.

In the synthesis II all three metal oxides were used as starting materials. Stoichiometric amounts of Gd_2O_3, Sc_2O_3 and Ga_2O_3 were separately dissolved in a boiling concentrated HNO_3 till solutions became completely transparent. The following synthetic procedures were the same as in synthesis I. Metal oxides as starting materials were also used in the synthesis III. Gadolinium, scandium and gallium nitrate solutions were prepared in the same way like in the synthesis II. Three solutions were mixed together and TRIS instead of 1,2-ethanediol was added to the above solution of metals. TRIS was used as complexing agent and also as initiator of self-burning process (combustion) of the gel when the Gd-Sc-Ga-O gel was completely dried. After self-initiated combustion very crumbly ash-like powders have formed. The further heat treatment of obtained powders was performed as in syntheses I and II.

The synthesis III were chosen as the best, hence rest of garnet samples presented in this dissertation work were synthesized following this route. In the preparation of metal-doped (Fe^{3+}, Ce^{3+}, Ce^{3+}/Cr^{3+} and Cr^{3+}) garnets the

appropriate amount of dopant metal nitrate were dissolved in distilled water and obtained solution was added before adding the complexing agent.

Synthesis temperature influence to the luminescence properties were analysed of the best mixed-metal gallium garnet doped with Cr^{3+} samples. Consequently, the particular samples were heat treated at 1300, 1400 and 1500 °C instead of 1000 °C temperature.

2.3. Synthesis Methods of $M_3XSi_2O_8$

Glaserite-type structure compounds $Ca_3MgSi_2O_8$ (CMSO), $Ba_3CuSi_2O_8$ (BCSO), $Ca_3Mg_{1-x}Cu_xSi_2O_8$ (CMCSO) and $Ba_{3-x}Ca_xCuSi_2O_8$ (BCCSO)), with empirical formula $M_3XSi_2O_8$ (M = Ca^{2+}, Ba^{2+}; X = Mg^{2+}, Cu^{2+}) were synthesized by aqueous sol-gel, conventional solid-state reaction and Travelling Solvent Floating Zone (TSFZ) methods.

2.3.1. Sol-Gel Method

The precursor gels for CMSO, BCSO and CMCSO were prepared by using stoichiometric amounts of analytical grade metal oxides, nitrates or carbonates and SiO_2 nanopowders as starting materials. In the sol-gel process, the metal oxides and carbonates were first dissolved in required amount of diluted HNO_3 under heating (~70 °C) and stirring in a beaker covered with a watch glass till the clear solution was obtained. Secondly, to the mixture of metal nitrate solution the required amount of SiO_2 np. and the complexing agent (1,2-ethanediol or TRIS) were added. The resulting mixture was stirred for ~2 h at 60 – 70 °C. The molar ratio of complexing agents to all metal ions was ~1:2 for the glycolate gels and ~1:1 for TRIS gels. Next, the solution was concentrated by evaporation under stirring at the same temperature and obtained gels were dried in the oven for 24 h at ~100 °C. The brownish gel powders were heated up on the hot-plate (~200 °C) for self-burn reaction initiation. The obtained powders were homogenized by grinding in an agate mortar. The different heating procedures are given in the results and discussion section 3.2.

2.3.2. Solid-State Method

The CMSO, BCSO, CMCSO, BCCSO, Ba_2SiO_4, $BaSiO_3$, $CaSiO_3$ and $BaCuO_2$ compounds were synthesized by conventional solid-state reaction method using stoichiometric amounts of analytical grade metal carbonates, oxides, peroxides, hydroxide carbonate and SiO_2 as starting materials. The starting materials grounded, heated and continuously homogenized for several times. In the case of synthesis of CMSO, CMCSO, $CaSiO_3$ and $BaSiO_3$, a flux (~2 wt% NH_4Cl) was mixed with starting materials. The ball-mill with agate beads and 2-propanol as solvent were used to homogenize the starting materials for 5 h during preparation of CMSO and CMCSO, and 1.5 h preparing BCCSO. After mixing the solvent was evaporated on hot-plate and remaining emulsion was dried overnight in the oven at ~100 °C. For the preparation of Ba_2SiO_4, $CaSiO_3$, $BaSiO_3$, $BaCuO_2$ and BCCSO compounds the starting materials were mixed and homogenized in agate mortar. The different heating procedures are given in the results and discussion section 3.2.

2.3.3. Traveling Solvent Floating Zone Method

In the Travelling Solvent Floating Zone (TSFZ) method the precursor powders for BCSO were prepared from stoichiometric mixtures of BaO_2, SiO_2 and $BaCuO_2$ or together with CuO. The precursor powders for first (1I-BCSO) and second (2I-BCSO) processes were mixed following stoichiometry of reaction (1) and for the third (3I-BCSO) according to the reaction (2).

$$10BaO_2 + 8SiO_2 + 2CuO + 2BaCuO_2 \rightarrow 4Ba_3CuSi_2O_8 + 5O_2 \quad (1)$$

$$2BaO_2 + 2SiO_2 + BaCuO_2 \rightarrow Ba_3CuSi_2O_8 + O_2 \quad (2)$$

These oxides were accurately weighed, mixed and ball-milled for 2 h. The mixture was ground and loaded into a rubber tube to fabricate the feed and seed rods. These tubes filled with precursor powders were hydrostatically pressed to about 35 – 42 MPa. The obtained rods had a diameter of ~8 mm and a length of 50 – 60 mm. Prepared rod were densified by heating before crystal growth process. Rods for 1I-BCSO and 2I-BCSO were preheated in air at 900 °C for 12 h and placed in to hot furnace for 1 h, respectively. Preheating

temperature for rods of 3I-BCSO process were chosen 750 °C (12 h). The rods for 3I-BCSO were again densified by fast preheating at TSFZ furnace, the translation speed 30 mm/h. The crystal was grown in an optical floating-zone furnace (CYBERSTAR Mirror furnace) equipped with two 2 kW Halogen lamps reaching a maximum temperature of 2400 °C and working pressure up to 1 MPa. The growth processes were performed in 20% of O_2 and 80% of Ar atmosphere, working pressure 0.5 – 0.8 MPa. The growth translation rate was in the range of ~13 mm/h and rotation rates of the feed rod and seed rod were ~25 rpm in opposite directions. The processing example is given at Fig. 11.

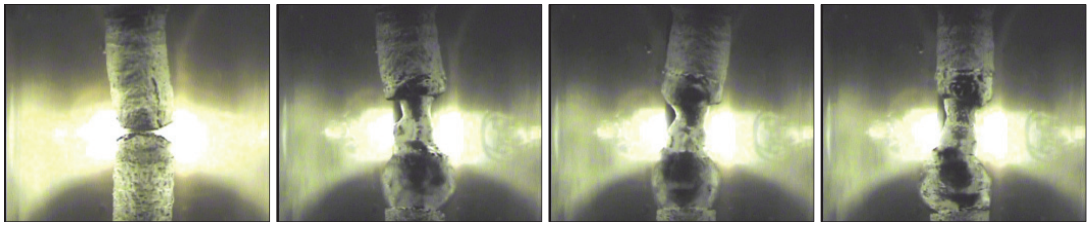

Fig. 11. The processing of 3I-BCSO in an optical floating zone furnace.

2.4. Characterization

2.4.1. Powder X-ray Diffraction Analysis

Powder X-Ray diffraction (XRD) measurements of samples discussed in this dissertation work were performed at room temperature on three diffractometers: (a) *Rigaku MiniFlex II* diffractometer working in Bragg-Brentano (θ/2θ) geometry, data were collected at a step of 0.02° and speed 1 s/step using Cu K_α radiation. This diffractometer was employed for the analysis of pure GSGG, GGG, YGG and LuGG garnets and Fe^{3+}, Ce^{3+}, Ce^{3+}/Cr^{3+} and Cr^{3+} doped garnet samples; (b) *Bruker D8 Advanced* diffractometer, data were collected at a step of 0.0102271° and speed of 1.03 s/step using Cu K_α radiation. This diffractometer was employed for the analysis of powders synthesized at high temperatures (1300 °C, 1400 °C and 1500 °C) and GGG:Ce samples. The intensity data sets of $Gd_{3-x}Ce_xGa_5O_{12}$ (x = 0.5, 1 and 3 mol%) were refined using Rietveld method by JANA2006 [162] software; (c) *PHILIPS PW1830* diffractometer working in Bragg-Brentano (θ/2θ) geometry, detector is a PW1820. Data were collected at a step of 0.02°

and speed 1 s/step using Cu K_α not mono-chromatized for Cu $K_{\alpha 2}$ radiation, wavelength Cu $K_{\alpha 1}$ = 1.5006 Å, Cu $K_{\alpha 2}$ = 1.5444 Å, ratio = 0.500. This diffractometer was used for the analysis of glaserite-type compounds.

2.4.2. FTIR Spectroscopy

The infrared spectra were recorded on Perkin-Elmer ATR-FTIR spectrometer equipped with a liquid nitrogen cooled MCT detector.

2.4.3. Thermal Analysis

The thermal decomposition of the precursors, gels and amorphous powders after self-combustion reaction was analysed through thermogravimetry and differential scanning calorimetry (TG-DSC) analysis using Perkin Elmer STA 6000 Simultaneous Thermal Analyzer. Dried samples of about 5 – 10 mg were heated from 25 to 950 °C at a heating rate of 10 °C/min in a dry flowing air (20 mL/min). The thermal behaviour of the samples for preparation glaserite-type compounds were analysed through simultaneous thermogravimetry and differential thermal analysis (TGA-DTA) using SETARAM Instrumentation TAG-1750 (High Performance Symmetrical TGA System (ambient / 1750 °C)) using Al_2O_3 as a reference. The samples of about 40 – 45 mg were heated from 50 to 1100 – 1450 °C temperature at a heating rate of 5 °C/min in a flowing (0.6 l/h) 20% O_2 and 80% Ar atmosphere.

2.4.4. SEM-EDX Analysis

The samples morphology and elemental composition on surface was characterized by three scanning electron microscopes equipped with energy-dispersive X-ray spectrometers: (a) Hitachi Tabletop Microscope TM3000, detector is a semiconductor BSE, 15.0 kV accelerating voltage for EDX measurements; (b) Hitachi SU-70, X-Max Extreme Silicon Drift Detector (SDD), 15.0 kV accelerating voltage for EDX measurements; (c) LEO 438VTP electron microscope coupled to a Noran Pioneer X-Ray detector, 20.0 kV accelerating voltage for EDS measurements.

2.4.5. ICP-OES Analysis

For the determination of element ratio in the synthesized GSGG:Cr and YGG:Cr samples inductively coupled plasma optical emission spectrometry was employed using Perkin-Elmer Optima 7000 DV spectrometer. For this analysis were used Gd, Sc, Ga, Y and Cr ICP single element standard solutions (1000 mg/l, Roth). Garnet samples were dissolved in diluted (volume ratio 1:1 with deionized water) nitric acid (HNO_3; 65%, Reachem). All solutions were prepared using deionized water.

2.4.6. UV/VIS Spectroscopy

Diffuse reflection spectra were measured using a spectrometer with an integrating sphere (Perkin Elmer Lambda 950, Spectralon white standard). The excitation and emission measurements were performed using a fluorescence spectrometer (Perkin Elmer LS55). Photoluminescence QE was measured using an integrating sphere (Sphere Optics, Spectralon white standard) and a spectrometer (Hamamatsu PMA-12). An incandescent lamp and a monochromator set at 440 nm were used for the excitation. A detailed explanation of the measurements of QE is given in [161], using the spectral data, the value of QE is calculated. These luminescent measurements were performed in the Institute of photonics and nanotechnology, Faculty of Physics, Vilnius University. Luminescence properties as well were measured using Edinburgh Instruments FLS980 spectrometer equipped 450WXe arc lamp, a cooled (-20 °C) single-photon counting photomultiplier (Hamamatsu R928) and mirror optics for powder samples. The photoluminescence emission spectra were corrected by a correction file obtained from a tungsten incandescent lamp certified by the NPL (National Physic Laboratory, UK). Photoluminescence lifetimes were measured with the Edinburgh Instruments FSL920 spectrometer equipped with the μF900 flash lamp and a Hamamatsu extended red sensitivity photomultiplier tube. Data were acquired in a gated single photon counting (MCS) mode.

3. RESULTS AND DISCUSSIONS

3.1. Sol-Gel Synthesis and Characterization of Mixed-Metal Garnets

3.1.1. Synthesis of $Gd_3Sc_2Ga_3O_{12}$: Optimization of Parameters

The XRD patterns of GSGG samples prepared using slightly different three synthesis ways [LIST OF AUTHOR'S PUBLICTIONS; Articles in journals; 2. S. Butkute et al., Journal of Sol-Gel Science and Technology, 76 (2015) 210-219] are shown in Fig. 12. As seen, the X-ray diffraction patterns of prepared GSGG samples are very similar. It is hard to see any difference in the measured diffractograms, which have perfect fit with standard data of GSGG phase, (ICDD) 04-006-8283. The single-phase gadolinium scandium gallium garnet powders were obtained during all three synthesis routes.

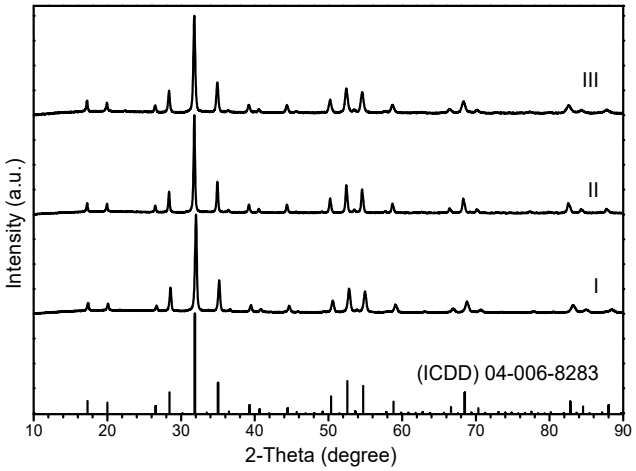

Fig. 12. XRD patterns of GSGG synthesized by syntheses I, II and III. Vertical lines represent standard XRD data of GSGG, (ICDD) 04-006-8283.

FTIR spectroscopy was used as additional tool for the characterization of obtained materials. The FTIR spectra of GSGG samples, obtained after the calcinations of Gd-Sc-Ga-O precursor gels at 1000 °C are shown in Fig. 13. The FTIR spectra show several intense broad bands. Strong absorption bands arising from O-H stretching and bending vibration of water due to the exposure of the sample to the atmosphere occur at 3438 and 1640 cm^{-1}, respectively [163]. The broad band in this range is more intensive of sample synthesized

following synthesis III. This can be caused by bigger surface, porosity or smaller obtained particles of the sample. Importantly, FTIR spectra also show that broad absorption bands in the region 800 – 400 cm^{-1} are well resolved into several narrow absorption bands. According to the literature data, this pattern corresponds to the metal-oxygen vibrations in the tetrahedral dislocation of garnet structure [62]. Therefore, the IR results support the conclusions made on grounds of the XRD measurements.

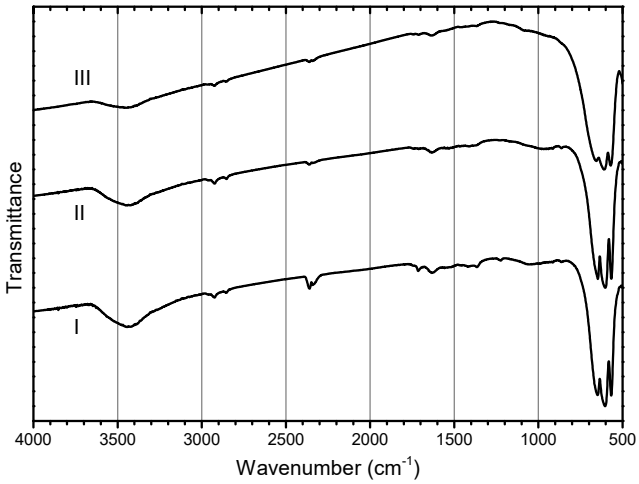

Fig. 13. FTIR spectra of GSGG samples synthesized by syntheses I, II and III after 1000 °C.

The morphology of the synthesized GSGG powders was studied using scanning electron microscopy (SEM). Interestingly, the results of SEM analysis showed that the nature of complexing agent used in the sol-gel processing has considerable impact on the morphological features of GSGG. The GSGG solids obtained during the syntheses I and II showed almost identical morphology. The micrographs of GSGG samples fabricated using syntheses I and II are presented in Fig. 14, (a) and (b) respectively.

As seen, the GSGG solids composed of differently shaped particles with wide particle size distribution. Some of particles have formed in nanometre size (less than 100 nm). However, the rest GSGG particles show variation in size from 1 to 25 μm. The SEM micrographs of GSGG samples prepared using synthesis III are shown in Fig. 14 (c) and (d). The SEM images clearly demonstrate that blocky angular shape particles were not formed in this case.

Moreover, the abundance of very small particles decreased in comparison to syntheses I and II. The obtained powders mostly consist of irregular shape sub-micron particles 1 – 5 μm in size. However, larger agglomerates (10 – 30 μm) having porous microstructure have formed as well.

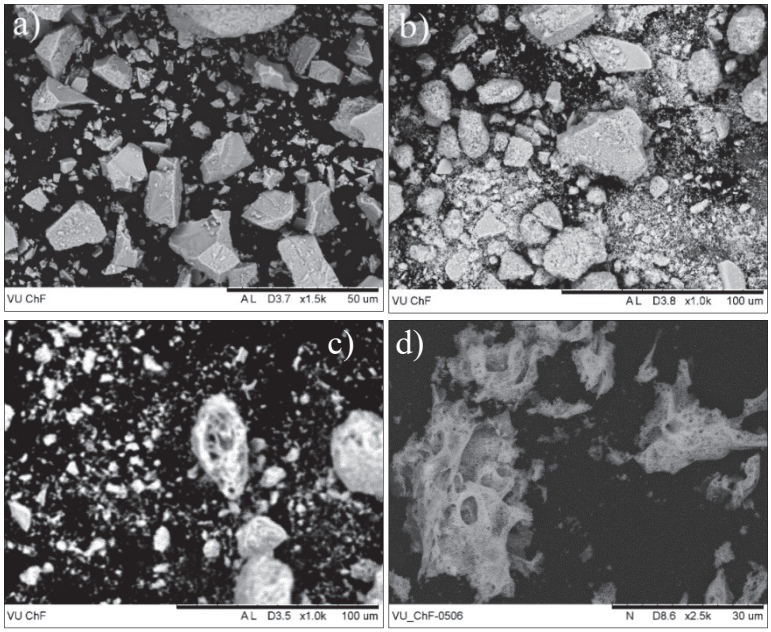

Fig. 14. SEM micrographs of GSGG synthesized by syntheses I (a), II (b) and III (c, d).

In conclusion, all three synthesis routes were suitable for the synthesis of single phase $Gd_3Sc_2Ga_3O_{12}$. Since application of TRIS in the sol-gel processing ensure receipt of GSGG particles with narrow particle size distribution, the synthesis III was chosen for the preparation of the rest garnet specimens in this study.

3.1.2. Investigation Fe^{3+}, Ce^{3+}, Ce^{3+}/Cr^{3+} and Cr^{3+} Doping Effects in $Gd_3Ga_5O_{12}$

The $Gd_3Ga_5O_{12}$ samples discussed in this chapter were synthesized following synthesis III route (Table 5).

Pure GGG was obtained after calcination of Gd-Ga-O TRIS precursor gel at 1000 °C. As it is seen from XRD diffraction pattern (Fig. 15) no other phases are formed during synthesis. The formation of single-phase GGG is confirmed by standard XRD data for this garnet phase (ICDD) 04-006-1592.

The X-ray diffraction patterns of the iron-doped GGG:Fe samples with different molar part of iron (0.25; 0.5; 1; 3; 5 and 10 mol%) in the compounds and sintered also at 1000 °C are shown in Fig. 16.

Table 5. The $Gd_3Ga_5O_{12}$ samples synthesized following synthesis III route.

Amount of dopant	$Gd_3Ga_5O_{12}$ (GGG)			
	Fe^{3+}	Ce^{3+}	Ce^{3+}/Cr^{3+}	Cr^{3+}
0.25 mol%	GGG:Fe0.25	GGG:Ce0.25	GGG:Ce,Cr0.25	GGG:Cr0.25
0.5 mol%	GGG:Fe0.5	GGG:Ce0.5	GGG:Ce,Cr0.5	GGG:Cr0.5
1 mol%	GGG:Fe1	GGG:Ce1	GGG:Ce,Cr1	GGG:Cr1
3 mol%	GGG:Fe3	GGG:Ce3	GGG:Ce,Cr3	GGG:Cr3
5 mol%	GGG:Fe5	GGG:Ce5	GGG:Ce,Cr5	GGG:Cr5
10 mol%	GGG:Fe10	GGG:Ce10	GGG:Ce,Cr10	GGG:Cr10

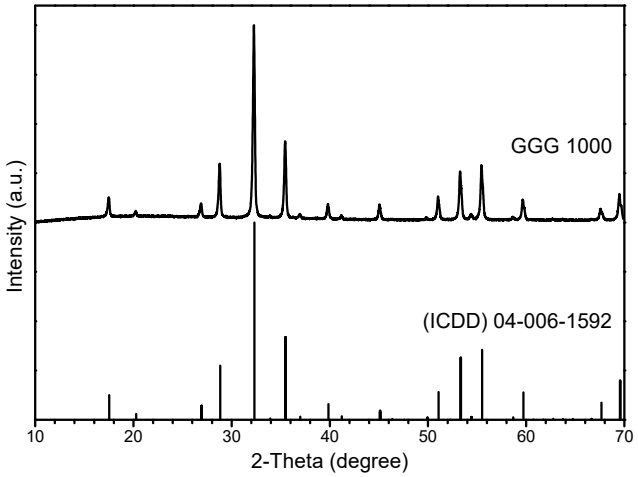

Fig. 15. XRD pattern of GGG synthesized using synthesis III approach. Vertical lines represent standard XRD data of GGG, (ICDD) 04-006-1592.

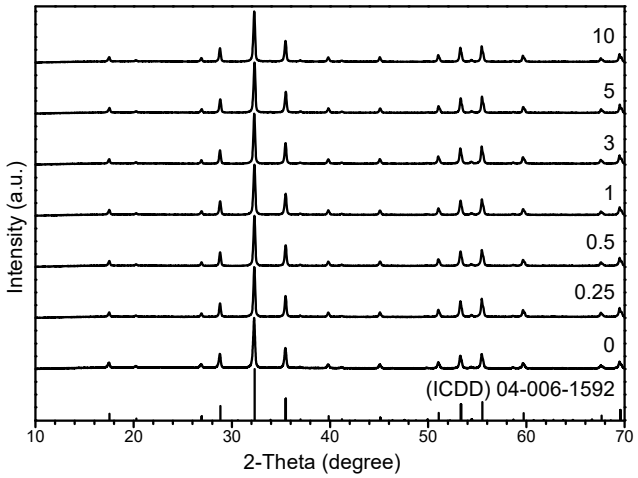

Fig. 16. XRD patterns of doped GGG:Fe (Fe = 0; 0.25; 0.5; 1; 3; 5 and 10 mol%) samples. Vertical lines represent standard XRD data of GGG.

As seen, the single phase products were obtained within the studied substitution range. When the molar part of iron is Fe = 0.25 – 10, the XRD patterns of GGG:Fe are analogous to the XRD patterns of un-doped garnets. All high intensity peaks are identified and could be attributed to the characteristic cubic garnet lattice.

The FTIR spectra of GGG:Fe samples obtained after the calcinations of Gd-Sc-Ga-Fe-O precursor gels at 1000 °C, are shown in Fig. 17. Notably, the characteristic narrow absorption bands in the region 800 – 400 cm^{-1} are well pronounced. Absorption bands of O-H stretching and bending vibration of water at 3438 and 1640 cm^{-1} are not seen because of small relative intensity and high scale in the graph.

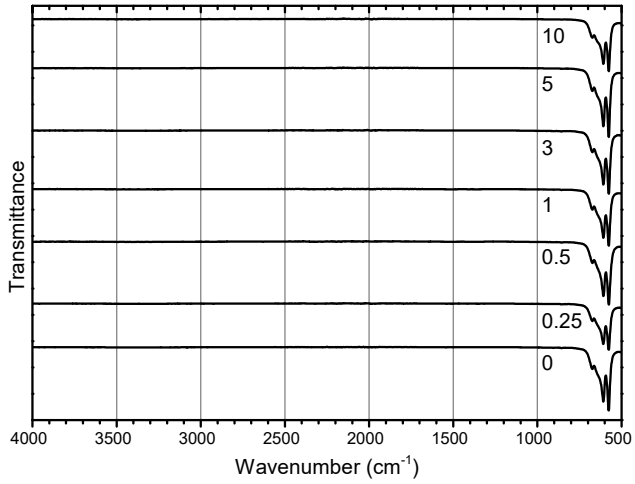

Fig. 17. FTIR spectra of GGG samples doped with different concentrations of Fe^{3+}.

It was demonstrated previously that different iron-doped compounds exhibit NIR luminescence [164-167]. Moreover, the mechanism of excitation of Er ions through Fe nanoclusters was suggested [168]. The luminescence properties of Fe^{3+} doped GGG powders were measured at ambient temperature. The excitation (λ_{em} = 730 nm) spectrum of GGG and emission spectra (λ_{ex} = 460 nm) of Fe^{3+} doped (0 – 10 mol%) GGG samples are given at Fig. 18. The excitation spectrum of GGG exhibit broad bands at 450 and 550 nm. As there are no activator ions in the phosphor matrix these bands might be attributed to small amount of impurities or defects in the lattice.

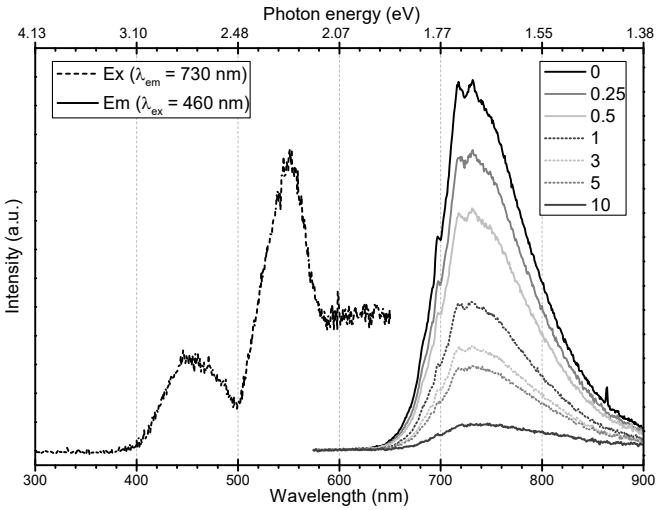

Fig. 18. Excitation spectrum of GGG and emission spectra of GGG:Fe.

The emission spectra of Fe^{3+} doped GGG samples has broad band at around 730 nm. One can see that undoped GGG garnet exhibits highest intensity of the emission. Interestingly the intensity of emission decreases monotonically with increasing the content of iron showing well resolved quenching effect of iron on the luminescence of GGG matrix. The broad bands observed in the 650 – 900 nm range also become more broaden probably due to non-equivalent Fe^{3+} and Gd^{3+} sites in the compounds. Thus, the results obtained illustrate the great iron quenching effect on the possible lanthanide-ion emission in the garnet matrixes. This observed iron based quenching of luminescence in GGG could be successfully applied for the development of method of analytical determination of transition metal ions in different objects or establishment of nitrogen storage systems [169, 170].

The cerium-doped GGG:Ce (Ce = 0.25; 0.5; 1; 3; 5 and 10 mol%) and cerium/chromium-co-doped GGG:Ce,Cr (Ce + Cr = 0.25; 0.5; 1; 3; 5 and 10 mol%; with equimolar molar amounts of cerium and chromium each) samples were also obtained at 1000 °C using the same sol-gel chemistry processing route. The X-ray diffraction patterns are shown in Fig. 19 of the cerium-doped GGG:Ce (A) and cerium/chromium-co-doped GGG:Ce,Cr (B). Evidently, the single phase products were obtained within the studied substitution range in all of the cases proving the high reproducibility of the suggested synthesis method. The XRD patterns of GGG:Ce and GGG:Ce,Cr

samples fit very well with the standardized XRD patterns of un-doped gadolinium gallium garnet.

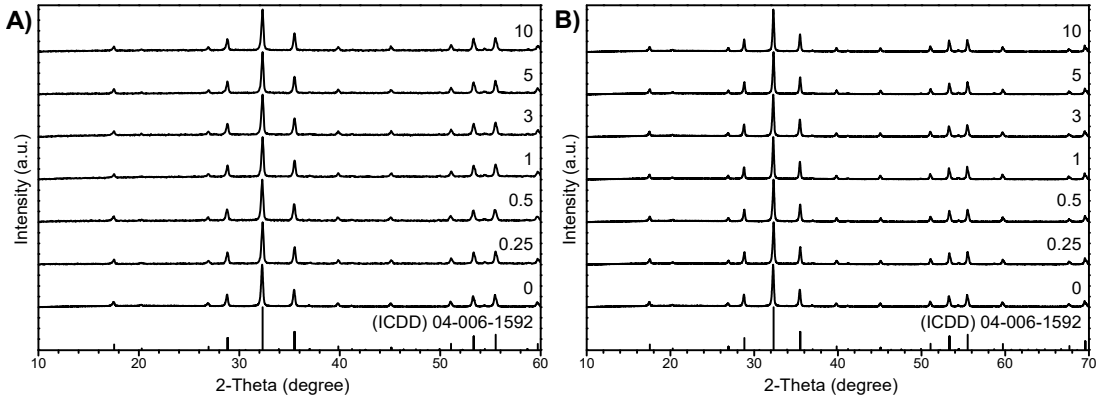

Fig. 19. XRD patterns of doped GGG:Ce (A) and co-doped GGG:Ce,Cr (B) samples. Vertical lines represent standard XRD data of GGG.

The excitation spectrum of GGG monitored for 730 nm emission and emission spectra of cerium-doped GGG (excited with 460 nm light) is depicted in Fig. 20, graph (A). The intensity of emission peak with the maximum at around 730 nm of the GGG doped with Ce^{3+} decreases with increasing amount of cerium. To conclude, the increase of cerium amount in garnet matrix has led to weaker emission, however, the decrease is not monotonous. These results clearly show that optical properties of GGG:Ce are quite different from the Ce-doped yttrium aluminium garnet samples [171, 172].

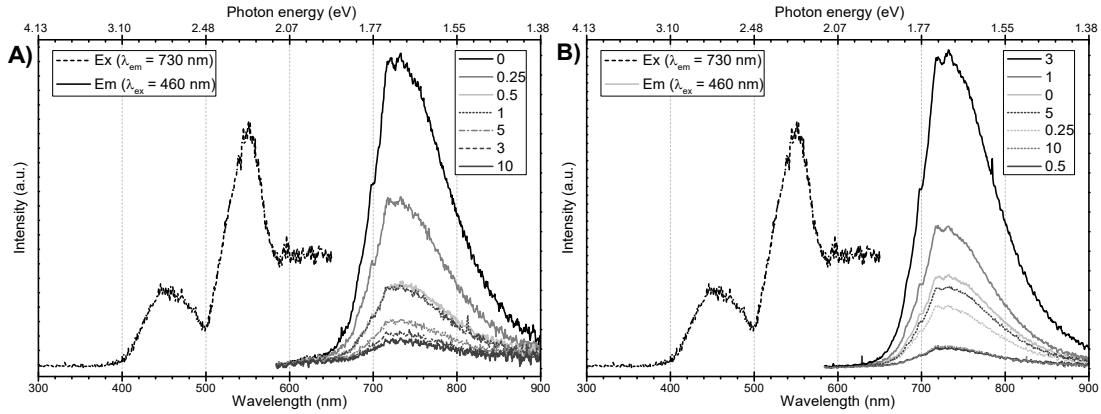

Fig. 20. Excitation spectrum of GGG and emission spectra of GGG:Ce (A) and GGG:Ce,Cr (B).

GGG:Ce^{3+},Cr^{3+} phosphors already exhibit ordinary luminescence properties for cerium/chromium co-doped garnet structure compounds

(Fig. 20, (B)). The highest intensity of the emission broad band at ~730 nm was observed for the GGG:Ce,Cr samples containing 3 mol% of dopants (1.5 mol% Ce^{3+} and 1.5 mol% Cr^{3+}). However, the emission decreases with the further increase of cerium and chromium concentration in the compound. To conclude, the emission of GGG samples is enhanced with the chromium content upsurge caused by the increased number of active luminescent centres.

The series of chromium doped (Cr^{3+} = 0.25; 0.5; 1; 3; 5 and 10 mol%) GGG were synthesized as well. The X-ray diffraction patterns of GGG:Cr samples are presented in Fig. 21. All the diffraction peaks match very well the standard XRD data of pure GGG (ICDD 04-006-1592). Fig. 22 presents the excitation (λ_{em} = 730 nm) spectrum of GGG and emission spectra (λ_{ex} = 460 nm) of chromium doped GGG samples. As is seen from emission spectra, GGG:Cr5 exhibit the strongest emission with a maximum in the red region (~ 730 nm) due to the $^7T_2 \rightarrow {}^4A_2$ transition [173]. For comparison and evaluation of the photoluminescence properties of sintered GGG doped with different metal ions (Fe^{3+}, Ce^{3+}, Ce^{3+}/Cr^{3+} and Cr^{3+}) the values of internal quantum yield (QE) are presented in Table 6.

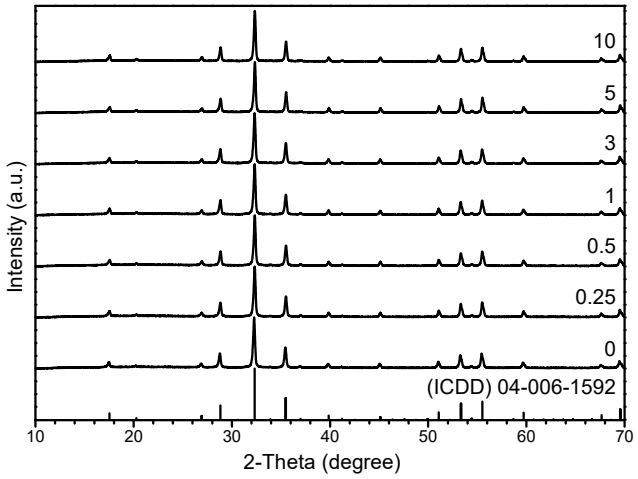

Fig. 21. XRD patterns of GGG:Cr (Cr^{3+} = 0.25; 0.5; 1; 3; 5 and 10 mol%) samples. Vertical lines represent standard XRD data of GGG.

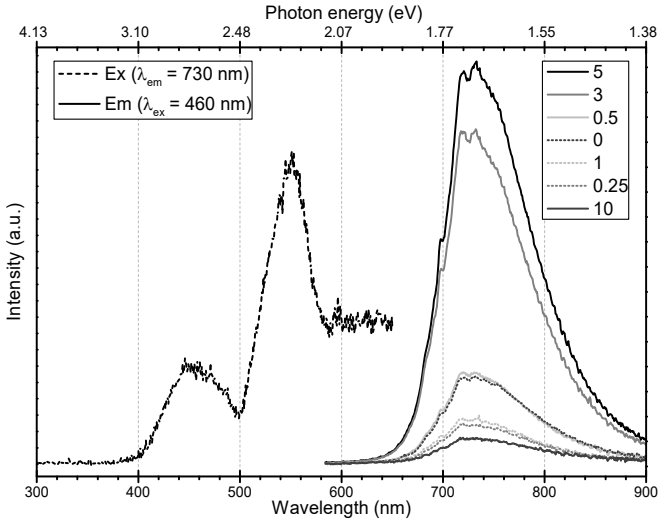

Fig. 22. Excitation spectrum of GGG and emission spectra of GGG:Cr.

Table 6. Values of the QE (%) of the GGG:M powders.

Doped mol%	GGG:Fe	GGG:Ce	GGG:Ce,Cr	GGG:Cr
0.00	2.9071	2.9071	2.9071	2.9071
0.25	**5.3438**	0.9140	2.3386	3.4666
0.5	2.7738	0.3365	2.5832	3.0815
1.0	1.7413	1.0444	2.5774	4.4041
3.0	1.6318	0.1237	**3.6494**	7.3711
5.0	0.4819	0.0818	1.4390	**7.9046**
10.0	0.2967	0.1408	1.4644	2.4647

The photoluminescence QE were calculated from measurements made in an integrated sphere following recommendations in the article of J. C. Mello [161]. The values of QE of cerium doped GGG samples are notably smaller than for un-doped GGG. Surprisingly, the value of QE of GGG:Fe0.25 is also very in comparison with other samples. Evidently, chromium doped samples show the best photoluminescence properties and the values of QE reaches 7.9% (GGG:Cr5).

In order to analyse the influence of sintering/annealing temperature to the photoluminescence properties the GGG:Cr5 were heated for 10 h at 1300, 1400 and 1500 °C temperatures instead of 1000 °C.

The XRD patterns of GGG:Cr5 samples synthesized at different temperatures (1000, 1300, 1400 and 1500 °C) are presented in Fig. 23.

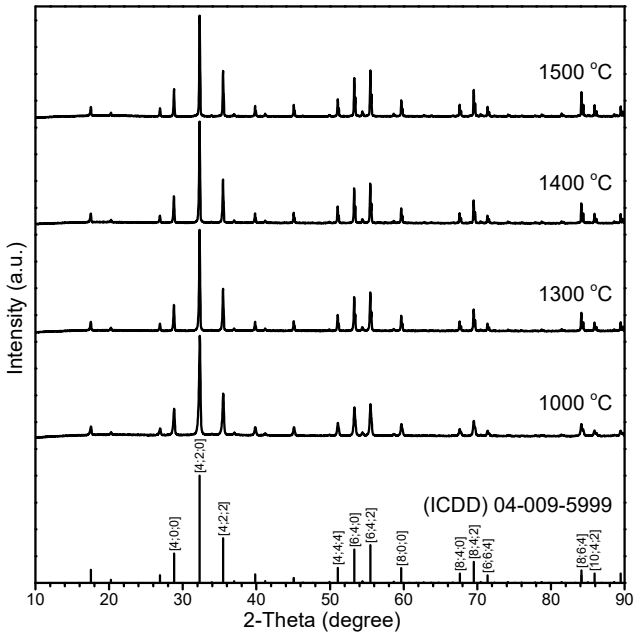

Fig. 23. XRD patterns of GGG:Cr5 samples sintered at 1000 – 1500 °C temperatures. Vertical lines represent standard XRD data of GGG.

Obviously, the cubic garnet (space group no. 230) as crystalline phase is determined in all these powder samples. However, the crystallinity increases by increase of annealing temperature. It is known that Bragg peak broadening may be caused by the average crystallite size decrease or existence of microstrains [174]. As it is hard to see the difference in peaks width by eye the Table 7 presents Full Weight at Half Maximum (FWHM) for most intensive XRD diffractograms peaks for correspondent [h; k; l] plane reflections of sintered GGG:Cr5 powder. It is determined, that the values of FWHM of Bragg's peak are largest calculated from the XRD pattern of powder annealed at 1000 °C and the values monotonically decreases by the increase of sintering temperature. This means that the crystallinity of the samples annealed at higher temperatures increases.

The SEM micrographs presented in Fig. 24 confirm and supplements the obtained results. It is clearly seen that temperature influences powder morphology significantly. The particle size increases with increasing synthesis temperature. The average size of particles annealed at 1300 °C is ~1.01 μm, at 1400 °C – ~1.75 μm and at 1500 °C – ~3.81 μm. After heating at higher temperatures (1400 and 1500 °C) the highly agglomerated network of particles

has formed instead of smoothly rounded shapes obtained at lower temperatures (1000 and 1300 °C).

Table 7. Counted FWHM for most intensive XRD peaks of sintered GGG:Cr5 powder samples.

(ICDD) 04-009-5999		FWHM			
2-Theta (degree)	[h;k;l]	1000 °C	1300 °C	1400 °C	1500 °C
28.82	[4;0;0]	0.083	0.0472	0.0482	0.0455
32.3	[4;2;0]	0.0849	0.0481	0.0483	0.0462
35.48	[4;2;2]	0.0861	0.0489	0.0481	0.0462
51.06	[4;4;4]	0.1003	0.0535	0.0505	0.0472
53.3	[6;4;0]	0.1044	0.0537	0.0506	0.0475
55.48	[6;4;2]	0.1071	0.0543	0.0517	0.0486
59.68	[8;0;0]	0.1099	0.0562	0.0524	0.0501
67.62	[8;4;0]	0.1189	0.0586	0.0555	0.0507
69.52	[8;4;2]	0.1256	0.0597	0.0579	0.0539
71.4	[6;6;4]	0.1235	0.0595	0.0545	0.0528
84.14	[8;6;4]	0.1504	0.0656	0.0603	0.0562
85.92	[10;4;2]	0.1023	0.0658	0.0614	0.0614

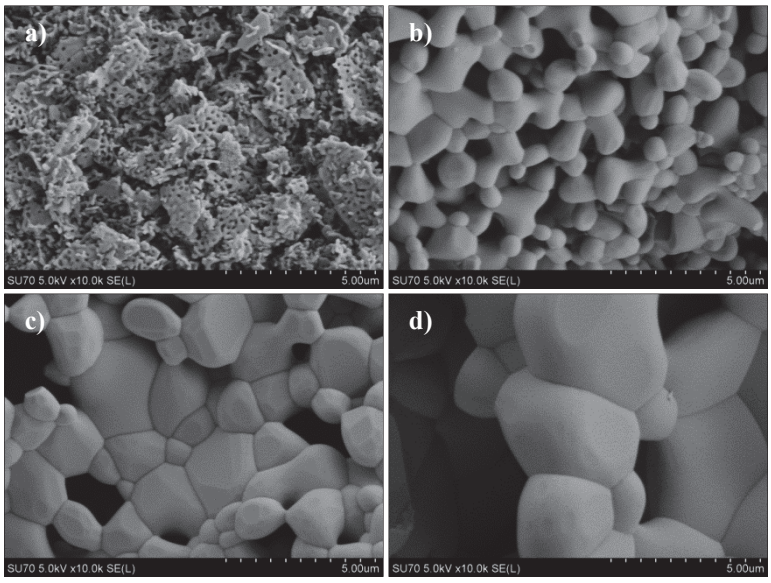

Fig. 24. SEM micrographs of GGG:Cr5 powders heated at 1000 °C (a), 1300 °C (b), 1400 °C (c) and 1500 °C (d).

Photoluminescence properties of GGG:Cr5 were investigated again. Excitation and emission spectra of GGG:Cr5 heated at higher temperatures are presented in Fig. 25. The prominent bands at 450 nm and smaller bands at

630 nm are visible in excitation spectra. It is seen that the intensities of excitation and emission spectra's increases with increasing synthesis temperature. More uniform crystallites with a better lattice quality are, probably, obtained at higher temperatures.

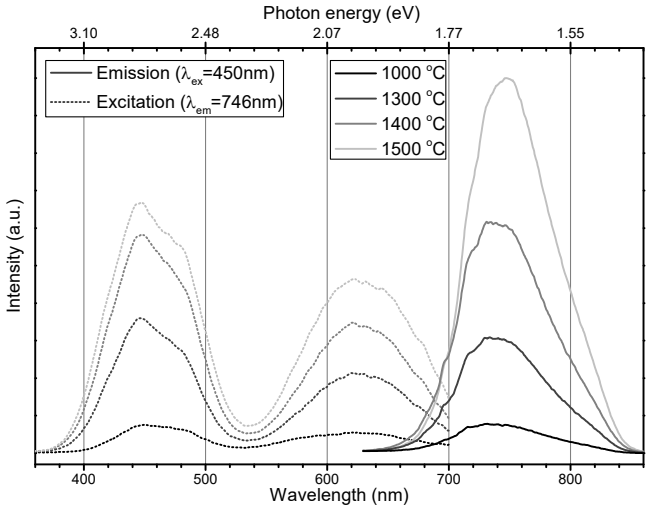

Fig. 25. Excitation and emission spectra of GGG:Cr5 powders synthesized at 1000, 1300, 1400 and 1500 °C temperatures.

The values of QE along with the band maximums of excitation and emission spectra of measured samples are presented in Table 8.

Table 8. Optical properties of the GGG:Cr5 powder samples.

GGG:Cr5	1000 °C	1300 °C	1400 °C	1500 °C
Internal QE (%), λ_{ex} = 445 nm	8	24	30	28
λ_{ex}, nm	447	446	447	446.5
λ_{em}, nm	717	717.5	716.5	716

It is seen that the values of QE of GGG:Cr5 for different heating temperatures correlate with photoluminescence intensity in the temperature range of 1000 – 1400 °C. The emission intensity is almost twice as high for the sample obtained at 1500 °C as for 1400 °C. However, the values of QE are very similar (28% and 30%, respectively). The reason is that GGG:Cr5 annealed at 1500 °C has stronger absorption.

3.1.3. Structure and Charge Density of $Gd_3Ga_5O_{12}:Ce^{3+}$ Garnets

Effects of Ce^{3+} doping on the band gap energy and electron density distributions for the $Gd_3Ga_5O_{12}$ have been studied by means of diffuse reflectance spectroscopy, X-ray diffraction technique and the maximum entropy method (MEM). The information on the refined structure from Rietveld refinement [175] has been utilized for the evaluation of electron density distribution. MEM refinements [176] were used to explicate the electron density distribution in GGG doped with Ce^{3+} (0.5, 1 and 3 mol%) heated at 1000 °C.

The Rietveld method is employed by JANA2006 [162] software. The enlarged view of a prominent peak shows the diffraction angular shifting towards lower angles with respect to Ce concentration. This angular shifting leads to increase the cell parameters summarized in Table 9. A standard software package formulated by Holland et al. [177] was used to refine the cell parameters. The intensity of X-ray datasets is in decreasing trend with Ce concentration due to lower atomic number of dopant atoms than the host atom. This evidence reveals that the dopant concentration is incorporated into the lattice as substitutional defects.

Table 9. Refined structural parameters of $Gd_3Ga_5O_{12}:Ce$

Refined parameters	Composition of Ce (mol%)		
	0.5	1	3
a = b = c (Å)	12.413(25)	12.434(14)	12.460(21)
α = β = γ (°)	90°	90°	90°
V (Å^3)	1912.96	1922.74	1934.58
R_p (%)	3.52	3.76	3.60
$_wR_p$ (%)	4.48	4.79	4.56
R_{obs} (%)	4.97	6.21	3.99
$_wR_{obs}$ (%)	4.79	4.52	3.64

The refined cell parameter increases with Ce concentration due to larger ionic radius than host atom (r_i = 1.034 Å for Ce^{3+} and r_i = 0.938 Å for Gd^{3+}). It infers that incorporation of cerium certainly increases the lattice parameters of

$Gd_3Ga_5O_{12}$ which is significant for the optical properties of non-linear optical material.

The maximum entropy method (MEM) is a versatile tool to study the electron density distribution. It is probability based statistical approached theory and it gives positive electron density distribution. The MEM method provides actual electron density rather than the normalized one and no phase information is required for constructing the electron density distribution. The nature of the bonding behaviour and the distribution of electrons in the bonding region can be clearly analysed by this technique. The uniform prior density was used in all the cases by dividing the total number of electrons by the volume of the unit cell. The software PRIMA was used for the MEM computations. The mid-bond positions and the calculated numerical values of the MEM mid-bond densities between the pair of different atoms of Ce (0.5, 1 and 3 mol%) doped GGG obtained from 1D electron density profiles are presented in Table 10.

Table 10. MEM mid-bond densities between different atoms of GGG:Ce obtained from 1D electron density profiles.

Bonding atom pair	Composition of Ce (mol%)					
	0.5		1		3	
	Position (Å)	Mid-bond electron density (e/Å^3)	Position (Å)	Mid-bond electron density (e/Å^3)	Position (Å)	Mid-bond electron density (e/Å^3)
Gd–Gd	3.4724	0.6402	3.4724	0.5217	3.4724	0.5931
Gd–Ga(2)	1.7470	0.5925	1.5529	0.5217	1.7470	0.5654
O–O	2.0702	1.2202	2.0702	0.4989	2.0702	1.0105
Ga(1)–O	1.0710	0.7808	0.9857	0.8868	1.0220	0.6504
Gd–O	1.4727	0.2962	1.5758	0.6355	1.5307	0.5043
Ga(2)–O	0.9732	0.8327	1.0606	0.7289	1.0156	0.5480
Gd–Ga(1)	1.5192	0.2742	1.7362	0.2825	1.6277	0.3865
Ga(1)–Ga(2)	1.5130	0.3124	1.7291	0.3353	1.7291	0.4997

Listed values in general show that the mid-bond electron densities between Gd–Gd, Gd–Ga(2) and O–O decreases with the increase of the nominal concentration of Ce up to 1% and then increases for 3%. The

mid-bond electron density between Gd–O and Ga(1)–O increases with the increase of nominal concentration of Ce up to 1% and then decreases for 3%. These values show typically the bonding to be covalent with the increasing electron density at the mid-bond position with the increasing concentration of the Ce. The mid-bond electron density between Ga(2)–O decreases with the increase of the nominal concentration of Ce up to 3%. The mid-bond electron density between Gd–Ga(1) and Ga(1)–Ga(2) increases with the increase of the nominal concentration of Ce up to 3%. The bond lengths between the atoms are also modified with Ce doping effect and it leads to increase in the volume of the unit cell.

The method to relate the energy of the incident photon to the band gap was proposed by Wood and Tauc [178]. According to their publication the optical band gap energy (E_g) of GGG:Ce (0.5, 1 and 3 mol%) have been calculated by fitting $(\alpha h\upsilon)^2$ against energy (E_g) from the diffuse reflectance spectroscopy data. The energy gap values of GGG:Ce are presented in Table 11. The band gap value is not in linear trend with cerium dopant. The band gap value decrease then Ce doping concentration is 3 mol%. The electron density distribution is rearranged due to the doping effect in the host system and the mid-bond electron density between the atoms follows non-linearity at 3 mol% of Ce^{3+}. This rearrangement of electron density between the atoms affects band gap value of the chosen system.

Table 11. Energy gap values of GGG:Ce

Composition of Ce (mol%)	Estimated band gap energy (eV)
0.5	5.40
1	5.43
3	5.39

3.1.4. Mixed-Metal Garnets Doped with Chromium

The best photoluminescence in NIR light range (~730 nm) obtained with Cr^{3+} ion as a luminescence centre in GGG matrix. Consequently, other Cr^{3+}-doped gallium garnets ($Gd_3Sc_2Ga_3O_{12}$ (GSGG), $Y_3Ga_5O_{12}$ (YGG) and

$Lu_3Ga_5O_{12}$ (LuGG)) were also synthesized and investigated [LIST OF AUTHOR'S PUBLICTIONS; Articles in journals; 1. A. Zabiliute et al., Applied Optics, 53 (2014) 907-914]. In this section the results of XRD, SEM, EDX, ICP-OES, PL, decay time and quantum efficiency measurements of Cr^{3+}- doped GSGG, YGG and LuGG samples are presented.

3.1.4.1. Investigation of $Gd_3Sc_2Ga_3O_{12}:Cr^{3+}$ Garnets

The list of $Gd_3Sc_2Ga_3O_{12}$ samples which were synthesized following synthesis III route are given in a Table 12.

Table 12. The $Gd_3Sc_2Ga_3O_{12}$ samples synthesized following synthesis III route.

Amount of Cr^{3+} mol%	$Gd_3Sc_2Ga_3O_{12}$ (GSGG) (heated 1000 °C)	Preparation temperature (°C)	GSGG:Cr8
3	GSGG:Cr3	1000	GSGG:Cr8
5	GSGG:Cr5		
8	GSGG:Cr8	1300	1300GSGG:Cr8
10	GSGG:Cr10		
12	GSGG:Cr12	1400	1400GSGG:Cr8
15	GSGG:Cr15		
20	GSGG:Cr20	1500	1500GSGG:Cr8

The XRD patterns of the GSGG:Cr samples are presented in Fig. 26 (A). As seen, the X-ray diffraction patterns of the GSGG samples doped with a different amount of chromium are very similar and confirm that in all cases the single-phase cubic garnets have been successfully synthesized by sol-gel processing. In order to understand phase formation during the sol-gel synthesis, the reaction products obtained at different temperatures were analysed. The XRD patterns of GSGG:Cr10 samples obtained after every synthesis step are given in Fig. 26 (B). These results show that cubic crystal structure of garnet already begins to form in the self-burning process, and is the dominant or the only obtained phase after heating at 800 °C. The diffraction peaks are broad confirming the poor crystallinity of the product.

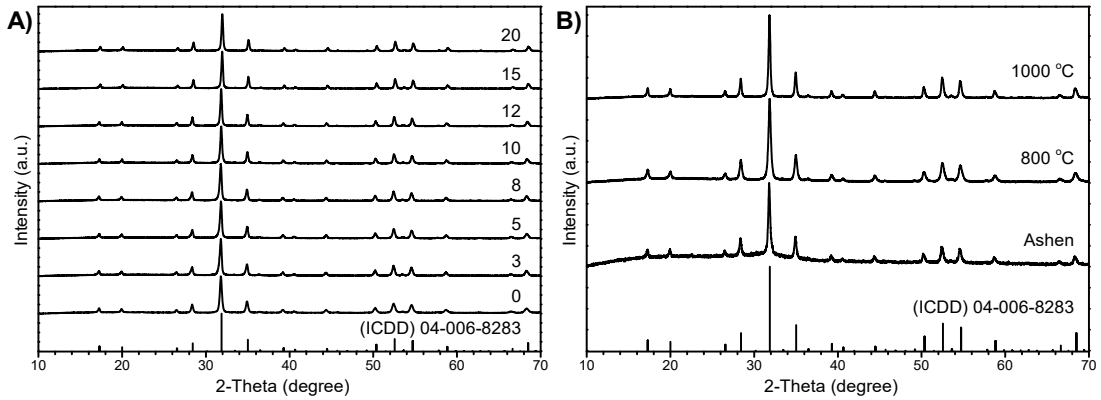

Fig. 26. XRD patterns of GSGG and Cr^{3+} doped GSGG:Cr samples (A) and GSGG:Cr10 samples obtained after every synthesis step (B). Vertical lines represent standard XRD data of GSGG.

Stoichiometry is a very important feature of mixed-metal oxides influencing or sometimes even determining the quality of physical properties of these compounds. Therefore, to know the real stoichiometry of metals in the multinary system is a very important task for materials scientists. When elements are combined resulting in a chemical reaction, the outcome of the reaction can be predicted on the basis of the elements and quantities involved. However, the real stoichiometry of metals which react at the experimental conditions can be different from the nominal stoichiometry. As the dopant element concentration rage were introduced to the GSGG and YGG matrixes are very large, the quantitative relationship between the reactants (calculated and expected) and the obtained products was inspected. The chemical composition of differently Cr^{3+}-doped garnet structure compounds was analysed by ICP-OES and EDX, and compared with the nominal one. The empirical formulas were calculated for garnet series and compared with the theoretical formula. The ICP-OES and EDX analysis data obtained for the GSGG:Cr are summarized in Table 13.

According to the ICP-OES results, the determined experimental molar ratio of metals was found to be Gd:Sc:Ga = 3:2:3 for GSGG. These results are in a very good agreement with the nominal composition of starting metal salts. Moreover, the determined amount of chromium was the same as the desired

concentration of the dopant element. Thus, the theoretical formula of GSGG is the same as the empirical formula of these synthesized garnets.

Table 13. The elemental composition of the sol-gel derived GSGG:Cr garnets determined by ICP-OES (n = 3) and EDX: SEM TM3000 (n = 3) and the High Resolution SEM (HR SEM) (n = 3).

Sample: GSGG:Cr			0	3	5	8	10	12	15	20
ICP-OES	at.%	Gd	3.06	3.08	3.02	3.05	2.93	2.96	3.00	2.98
		Sc	2.00	2.00	2.00	2.00	2.00	2.00	2.00	2.00
		Ga	2.91	2.94	2.90	2.90	2.87	2.91	2.99	2.98
		Cr	–	3.40	5.10	8.0	9.9	12.5	15.1	19.8
SEM TM3000	at.%	Gd	3.04	3.15	3.05	3.18	3.02	2.97	2.97	2.95
		Sc	2.00	2.00	2.00	2.00	2.00	2.00	2.00	2.00
		Ga	2.94	3.03	3.00	2.99	2.89	2.98	3.06	2.97
		Cr	–	3.3	5.0	8.4	10.1	12.3	15.5	19.9
HR SEM	at.%	Gd	3.03	2.98	2.96	3.07	3.00	2.95	3.02	2.93
		Sc	2.00	2.00	2.00	2.00	2.00	2.00	2.00	2.00
		Ga	3.20	3.14	3.16	3.02	3.01	2.97	2.94	2.99
		Cr	–	3.0	4.9	8.0	10.3	11.8	15.2	20.0

As seen from the EDX results obtained for the GSGG:Cr specimens, the both scanning electron microscopes give comparable results with a high accuracy. Thus, the relevance of the EDX method for the determination of the chemical composition of the solid-state inert matrix and the dopant element is evident. We can conclude that sol-gel processing allowed us to perform a successful synthesis of GSGG with an exact amount of chromium dopant.

The excitation (λ_{em} = 750 nm) and emission (λ_{ex} = 450 nm) spectra of chromium doped GSGG samples are presented at Fig. 27. The PL spectra of differently chromium doped GSGG samples exhibit emission in NIR region (peak maximum at 750 nm). These phosphors have a broad PL band correspondent to the $^4T_2 \rightarrow {}^4A_2$ transition. As is seen from excitation and emission spectra GSGG:Cr8 shows the highest emission intensity.

Luminescence properties were further investigated by dopant-dependent luminescence life time measurements. The recorded PL decay curves of

GSGG:Cr samples as a function of Cr^{3+} concentration are given in Fig. 28. In order to calculate the PL decay lifetimes the decay curves for 450 nm excitation and 750 nm emission were fitted to bi-exponential function:

$$I(t) = A + B_1 e^{-t/\tau 1} + B_2 e^{-t/\tau 2} \quad \text{(Eq. 5)}$$

Here $I(t)$ is PL intensity at a given time t; A is background; B_1 and B_2 are constants; and τ_1 and τ_2 are PL decay lifetimes. The obtained values are given in Table 14, as well calculated average PL lifetime values $\bar{\tau}$ are included.

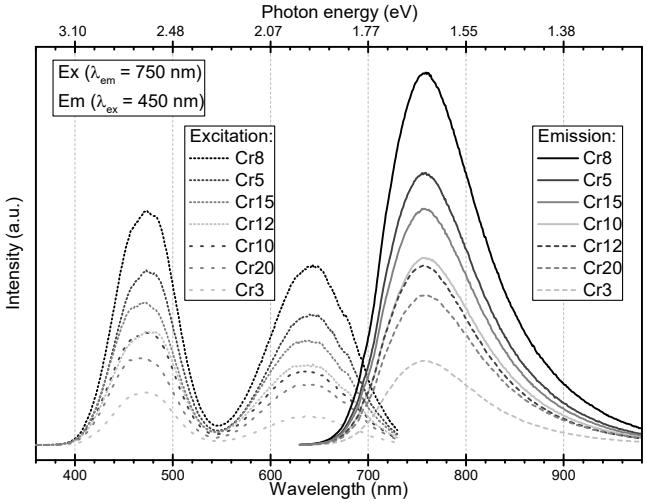

Fig. 27. Excitation and emission spectra of GSGG:Cr.

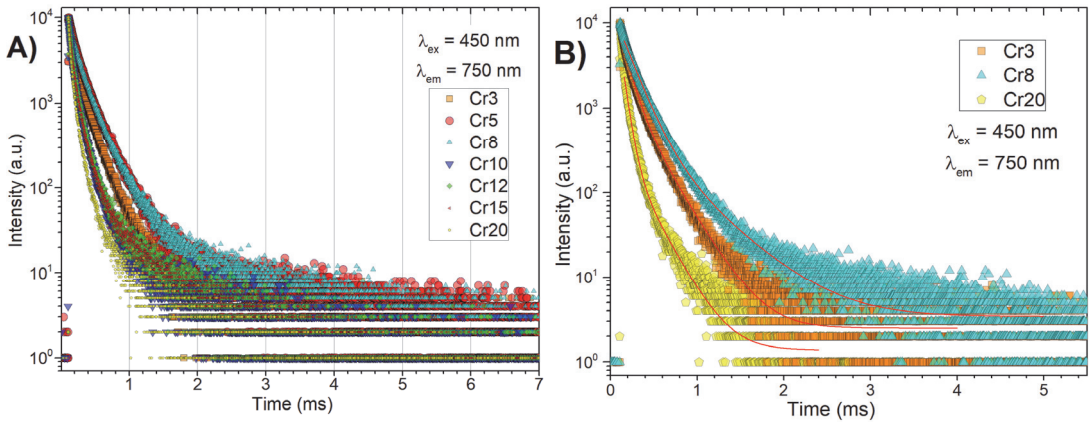

Fig. 28. PL decay curves of GSGG:Cr samples as a function of Cr^{3+} concentration (A). PL decay curves of GSGG:Cr with 3, 5 and 20 mol% samples, where solid red lines correspond to the bi-exponential fits (B).

It is seen from Fig. 28 that the curves are steeper (decay process is faster) when Cr^{3+} concentrations are high, but the decrease in not coherent. The PL decay times for GSGG:Cr were found to be in the microsecond range and

are comparable to the results obtained for crystalline samples [179]. The results of PL lifetime correlate with PL intensities for GSGG:Cr8 ($\bar{\tau}$ = 299.89 μs), GSGG:Cr5 ($\bar{\tau}$ = 265.83 μs) and GSGG:Cr15 ($\bar{\tau}$ = 257.9 μs) samples.

Table 14. The results of bi-exponential fitting calculation form PL decay curves of GSGG:Cr.

Sample name	**τ_1 (μs)**	τ_1 (%)	**τ_2 (μs)**	τ_2 (%)	**$\bar{\tau}$, (μs)**	A	χ^2
GSGG:Cr3	99.13	52.07	256.41	47.93	209.89	2.500	1.403
GSGG:Cr5	138.01	60.97	345.57	39.03	265.83	3.523	1.568
GSGG:Cr8	158.86	78.06	469.62	21.94	299.89	3.414	1.576
GSGG:Cr10	83.65	77.92	334.43	22.08	216.85	2.047	1.419
GSGG:Cr12	84.17	76.58	371.65	23.42	249.34	1.925	1.467
GSGG:Cr15	80.20	76.05	377.71	23.95	257.90	1.592	1.428
GSGG:Cr20	57.29	67.78	227.53	32.22	168.58	1.379	1.218

The values of QE and optical properties are given in Table 15. For GSGG:Cr samples the PL intensity and the value of QE increased with the increase of amount of Cr^{3+}, till it reached 8 mol%. This is expected, since the concentration of activator ions in the lattice is increased. However, at higher concentrations the PL intensities are decreasing, which might be caused by the concentration quenching.

Table 15. Values of the QE of the GSGG:Cr powder samples.

GSGG:Cr	3 mol%	5 mol%	8 mol%
Internal QE (%), λ_{ex} = 445 nm	0.6	1.3	1.6
λ_{ex} (nm)	470	473	474
λ_{em} (nm)	757	758	759

The influence of powder preparation temperature on the PL properties was analysed by synthesizing GSGG:Cr8 (the best value of QE from other samples prepared at 1000 °C) at higher, 1300, 1400 and 1500 °C, temperatures. The XRD patterns of GSGG:Cr8 samples synthesized at different temperatures are presented in Fig. 29. The Table 16 presents Full Weight at Half Maximum (FWHM) for the most intensive XRD peaks for correspondent [h; k; l] plane reflections of cubic GSGG:Cr8.

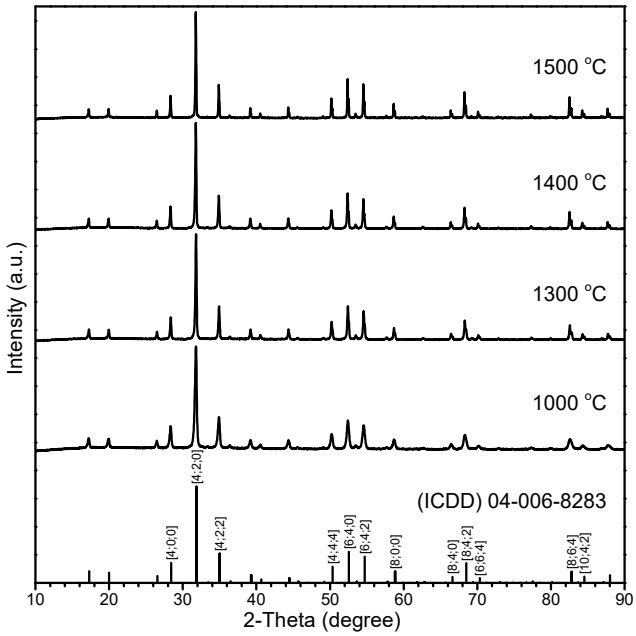

Fig. 29. XRD patterns of GSGG:Cr8 samples sintered at 1000 – 1500 °C temperatures. Vertical lines represent standard XRD data of GSGG.

Table 16. Counted FWHM for most intensive XRD peaks of sintered GSGG:Cr8 powder samples.

(ICDD) 04-006-8283		FWHM			
2-Theta (degree)	[h;k;l]	1000 °C	1300 °C	1400 °C	1500 °C
28.44	[4;0;0]	0.2506	0.1589	0.1549	0.1263
31.88	[4;2;0]	0.2691	0.1665	0.1610	0.1291
35.02	[4;2;2]	0.2739	0.1683	0.1659	0.1334
50.36	[4;4;4]	0.3097	0.1997	0.1914	0.1439
52.56	[6;4;0]	0.3300	0.2042	0.1911	0.1468
54.72	[6;4;2]	0.3377	0.2125	0.1600	0.1494
58.84	[8;0;0]	0.3401	0.2235	0.2020	0.1502
66.64	[8;4;0]	0.3876	0.2444	0.1600	0.1411
68.5	[8;4;2]	0.4006	0.2423	0.1600	0.1322
70.34	[6;6;4]	0.3910	0.2550	0.3463	0.1283
82.82	[8;6;4]	0.4658	0.2537	0.1600	0.1262
84.54	[10;4;2]	0.5882	0.2649	0.1600	0.1213

Since the reflections are narrower, the crystallinity of the samples increases with increasing temperature. The values of FWHM of Bragg's peak are largest for the sample heated at 1000 °C, and the values monotonically decrease by the increase of sintering temperature. By increasing sintering

temperature the particle size increases as well (Fig. 30). The average size of particles obtained at 1300 °C is ~237 nm, at 1400 °C – ~742 nm and at 1500 °C – ~1.63 μm.

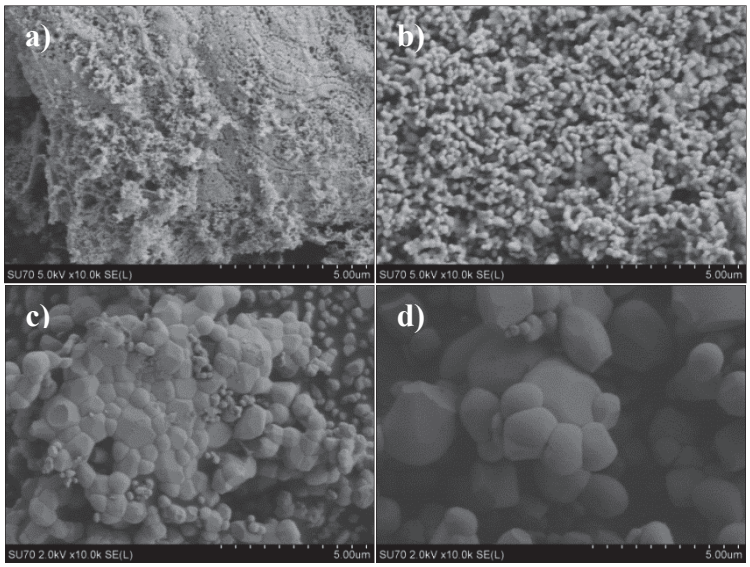

Fig. 30. SEM micrographs of GSGG:Cr8 powders obtained at 1000 °C (a), 1300 °C (b), 1400 °C (c) and 1500 °C (d).

Excitation and emission spectra of GSGG:Cr8 heated at higher temperatures are presented in Fig. 31.

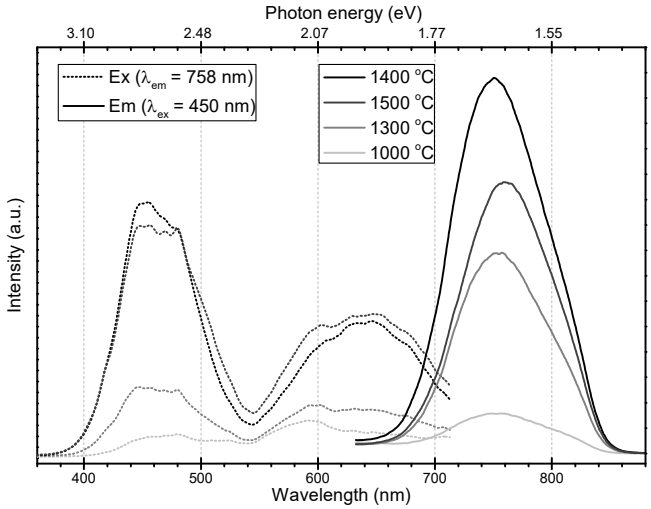

Fig. 31. Excitation and emission spectra of GSGG:Cr8 powders obtained at different temperatures.

It is seen that the intensity of excitation and emission spectra's increases with increasing the temperatures till 1400 °C. However, the phosphor prepared at 1500 °C shows smaller PL. More uniform crystallites with a better lattice

quality are obtained at higher temperatures, but dopants might cause defects in the crystalline lattice, which creates non-radiative transitions.

The values of QE and maximums of excitation and emission spectra are given in Table 17. The values of QE of GSGG:Cr8 synthesized at different temperatures correlate with photoluminescence intensity.

Table 17. Optical properties of the GSGG:Cr8 powder samples.

GSGG:Cr8	1000 °C	1300 °C	1400 °C	1500 °C
Internal QE (%), λ_{ex} = 445 nm	1.6	19	21	19
λ_{ex}, nm	548.5	450	457	448
λ_{em}, nm	736.5	750	759	756

3.1.4.2. Investigation of $Y_3Ga_5O_{12}:Cr^{3+}$ Garnets

The list of investigated Cr^{3+} doped $Y_3Ga_5O_{12}$ samples is given in a Table 18.

Table 18. The $Y_3Ga_5O_{12}$ samples synthesized following synthesis III route.

Amount of Cr^{3+} mol%	$Y_3Ga_5O_{12}$ (YGG) (heated 1000 °C)	Preparation temperature (°C)	YGG:Cr8 powder	YGG:Cr8.7 pellet
3	YGG:Cr3			
5	YGG:Cr5	1000	YGG:Cr8	YGG:Cr8.7
8	YGG:Cr8	1100	-	1100YGG:Cr8.7
10	YGG:Cr10	1200	-	1200YGG:Cr8.7
12	YGG:Cr12	1300	1300YGG:Cr8	1300YGG:Cr8.7
15	YGG:Cr15	1400	1400YGG:Cr8	1400YGG:Cr8.7
20	YGG:Cr20	1500	1500YGG:Cr8	-

The XRD patterns of synthesized YGG samples are shown in Fig. 32. As seen, the XRD patterns of the samples doped with a different amount of chromium agree with (ICDD) 00-043-0512 standardized data of $Y_3Ga_5O_{12}$ cubic garnet phase (s.g. no. 230). The beginning of garnet phase formation is in very early stage, i.e. already at self-propagating combustion process.

The chemical composition of differently Cr^{3+}-doped YGG has been investigated by ICP-OES and EDX techniques. According to the obtained results (Table 19), the determined molar ratio of metals in the synthesized

YGG garnets was found to be Y:Ga = 3:5. These results are in a good agreement with the nominal composition of precursors.

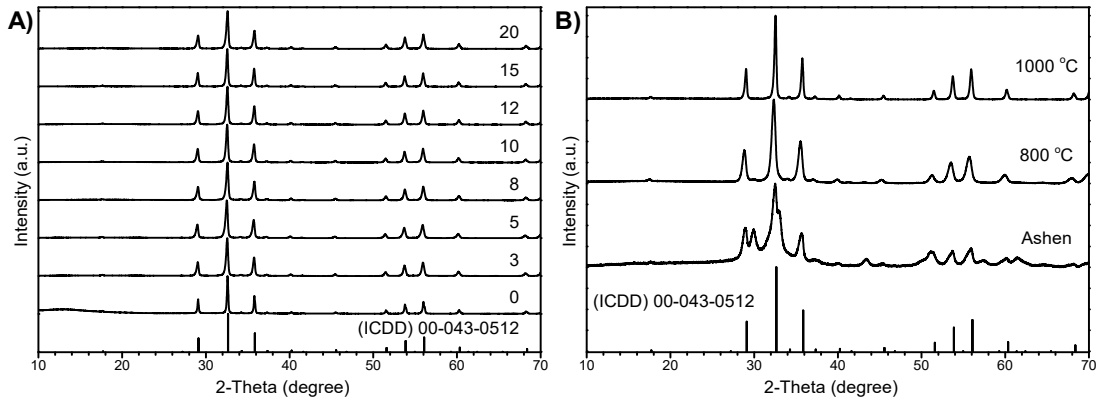

Fig. 32. XRD patterns of YGG and Cr^{3+} doped YGG:Cr samples (A) and YGG:Cr3 samples after every synthesis step (B). Vertical lines represent standard XRD data of YGG.

Table 19. The elemental composition of the sol-gel derived YGG:Cr garnets determined by ICP-OES (n = 3) and EDX: SEM TM300 (n = 3) and the High Resolution SEM (HR SEM) (n = 3).

Sample: YGG:Cr			0	3	5	8	10	12	15	20
ICP-OES	at.%	Y	3.00	3.00	3.00	3.00	3.00	3.00	3.00	3.00
		Ga	4.79	4.80	4.83	4.88	4.82	4.83	4.86	4.83
		Cr	–	2.9	5.0	8.3	9.8	12.4	15.3	20.2
SEM TM3000	at.%	Y	3.00	3.00	3.00	3.00	3.00	3.00	3.00	3.00
		Ga	4.95	5.05	4.87	4.94	4.96	5.03	5.11	4.99
		Cr	–	3.1	5.4	8.08	10.3	11.7	14.6	19.8
HR SEM	at.%	Y	3.00	3.00	3.00	3.00	3.00	3.00	3.00	3.00
		Ga	4.84	5.18	5.14	5.09	4.93	5.07	4.87	5.19
		Cr	–	3.0	4.8	7.26	10.1	12.1	15.4	19.6

As seen, the both scanning electron microscopes provide analogous EDX results with a high accuracy. Moreover, the determined amount of chromium was the same as the desired concentration of the dopant element. Thus, the theoretical formula of YGG is the same as the empirical formula of these synthesized garnets.

The excitation and emission spectra of differently Cr^{3+} doped YGG samples annealed at 1000 °C are shown in Fig. 33.

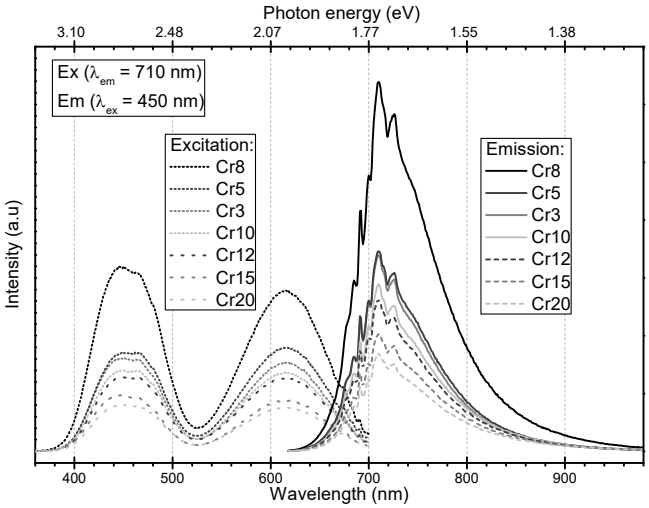

Fig. 33. Excitation and emission spectra of YGG:Cr samples.

Cr-doped materials can exhibit a broad band 4-level system, if a crystal field is low at the Cr site and/or a large Stokes-shift of the $^4T_2$ level yields a $^4A_2 \rightarrow {}^4T_2$ splitting which is similar or even smaller than the $^4A_2 \rightarrow {}^2E$ splitting. Thus, most of the fluorescence is channelled into the broad band $^4T_2 \rightarrow {}^4A_2$ transition [180], like was observed for GGG:Cr and GSGG:Cr samples. In the excitation spectra two broad bands at around 450 nm and 620 nm that correspond to $^4A_2 \rightarrow {}^4T_1$ and $^4A_2 \rightarrow {}^4T_2$ transitions, respectively, are clearly seen. Weak crystal fields lead to broad $^4T_2 \rightarrow {}^4A_2$ fluorescence and when crystal field is strong the lowest excited state is the ^2E-level, and at room-temperature the radiative decay occurs mainly via the sharp $^2E \rightarrow {}^4A_2$ transition (R-lines) [61]. The crystal-field strength mainly depends on the chemical composition of phosphors and on the Cr^{3+}-O distance in a matrix. When the distance is decreasing the crystal-field strength increase [181]. As PL measurements in this study were held at room temperatures the characteristic sharp and intense lines correspondent to the $^2E \rightarrow {}^4A_2$ are not well seen, because the R-lines and their attendant vibronic sideband decrease in intensity and a broad emission band partially overlapping the R-line region [61, 106, 173, 181, 182]. A broad PL band in the far-red region due to the $^2E_2 \rightarrow {}^4A_2$ transition and peaks at around 710 nm is seen for all samples investigated by us. The highest

intensities were observed from YGG:Cr8 samples at both emission and excitation spectra.

The decay kinetics of Cr^{3+} luminescence in YGG polycrystals shows non-single exponential behaviour (Fig. 34).

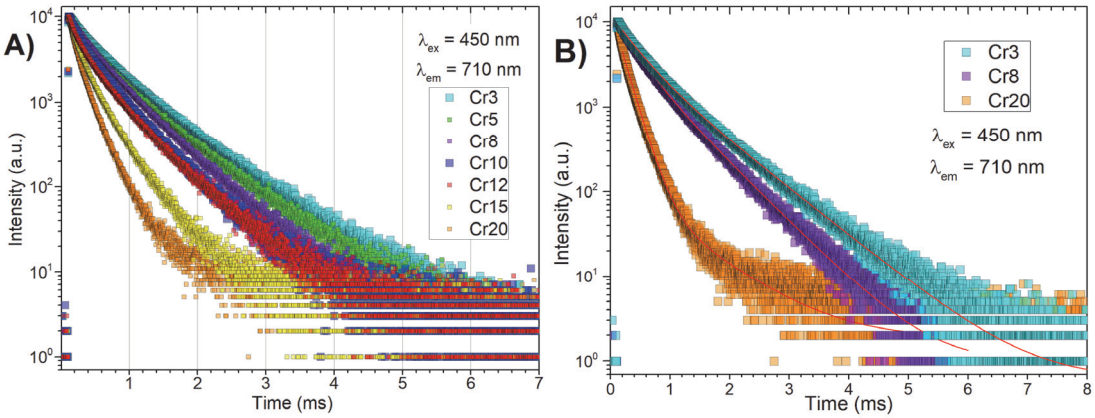

Fig. 34. PL decay curves of YGG:Cr samples as a function of Cr^{3+} concentration (A). PL decay curves of YGG:Cr with 3, 8 and 20 mol% samples (B). Solid red lines correspond to the bi-exponential fits.

Such behaviour is common for the most of Cr^{3+} doped gallium garnets [173, 181]. The decomposition of the respective decay curves in to elementary components demonstrates the existence of two components τ_1 and τ_2 with average decay times $\bar{\tau}$ = 360 – 700 μs. The decays were decomposed into two exponents (Table 20). The average decay constants were calculated and assumed to represent the lifetimes of YGG:Cr. The decrease of the Cr^{3+} ions lifetime in the high concentrated samples under excitation λ_{ex} = 450 nm indicates that the $Cr^{3+} \leftrightarrow Cr^{3+}$ energy transfer occurs.

Table 20. The results of bi-exponential fitting calculation form PL decay curves of YGG:Cr samples.

Sample name	**τ_1 (μs)**	τ_1 (%)	**τ_2 (μs)**	τ_2 (%)	**$\bar{\tau}$, (μs)**	A	χ^2
YGG:Cr3	341.34	31.40	780.94	68.60	707.65	0.618	1.010
YGG:Cr5	304.43	33.54	738.70	66.46	663.93	0.947	1.118
YGG:Cr8	291.73	33.39	626.82	66.61	563.43	0.969	1.075
YGG:Cr10	235.26	32.89	567.96	67.11	511.82	2.068	1.154
YGG:Cr12	231.44	36.99	590.00	63.01	522.88	2.005	1.220
YGG:Cr15	192.63	56.73	455.87	43.27	362.02	2.061	1.227
YGG:Cr20	179.50	90.17	838.29	9.83	401.75	1.852	1.403

The values of QE and optical properties are given in Table 21. As was observed for GSGG:Cr samples, the value of QE and the PL intensity of YGG:Cr increased with the increase the amount of Cr^{3+} till the dopant concentration reached 8 mol%. However the QE values of YGG:Cr8 is more than 10 times larger (18%).

Table 21. The QE values of the 3, 5 and 8 mol% of Cr^{3+} doped YGG powder samples.

YGG:Cr	3 mol%	5 mol%	8 mol%
Internal QE (%),λ_{ex} = 445 nm	13	12	18
λ_{ex} (nm)	444.5	444.5	442
λ_{em} (nm)	711	710	710

The highest QE was obtained from YGG:Cr8 powders synthesized at 1000 °C temperature. The influence of preparation temperature on the PL properties was analysed by synthesizing YGG:Cr8 at higher temperatures (1300, 1400 and 1500 °C). YGG doped with 8.7 mol% of Cr^{3+} pellets were prepared at 1000, 1100, 1200, 1300 and 1400 °C temperatures. The XRD patterns of YGG:Cr8 powders and YGG:Cr8.7 pellets synthesized at different temperatures are presented in Fig. 35. From the presented XRD patterns is seen that powders and pellet samples perfectly fit with standard data of YGG.

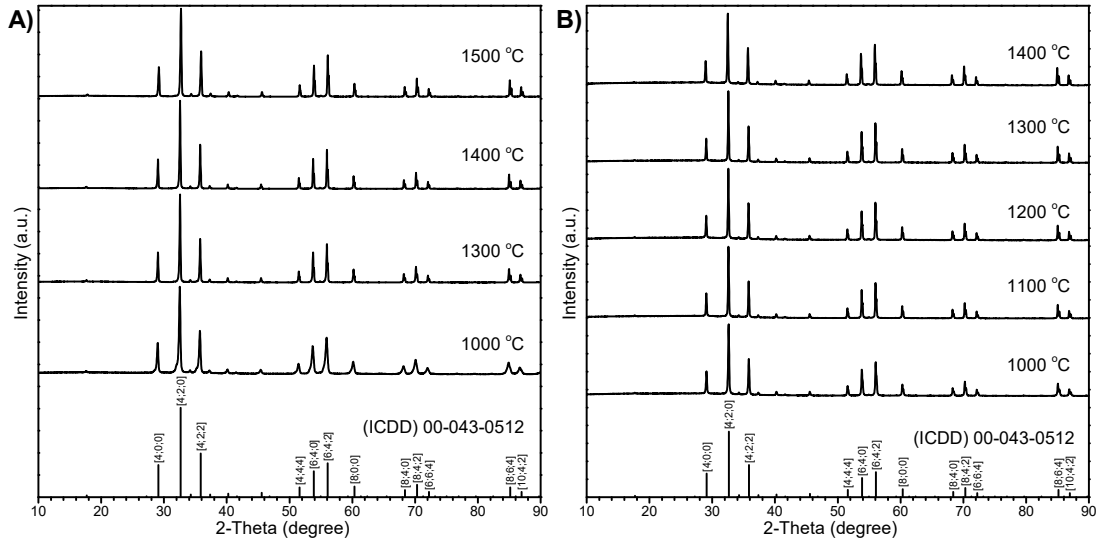

Fig. 35. XRD patterns of YGG:Cr8 powders (A) and YGG:Cr8.7 pellets (B) annealed at 1000 – 1500 °C temperatures. Vertical lines represent standard XRD data of GGG.

The Table 22 summarizes FWHM values of most intensive XRD peaks of YGG:Cr8 powders and YGG:Cr8.7 pellets calculated at different temperatures. The values of FWHM of YGG:Cr8 decrease by increasing temperature from 1000 to 1400 °C. However, FWHM values of 1500YGG:Cr8 are higher than for 1400YGG:Cr8 sample. FWHM values of pelletized samples are notably lower in comparison with powdered samples. However, the trend of decrease by the increasing the temperature is not obtained. The smallest FWHM values were observed for the 1400YGG:Cr8.7 pellets.

Table 22. FWHM for most intensive XRD peaks of YGG:Cr8 powders and YGG:Cr8.7 pellets.

(ICDD) 00-043-0512		FWHM						
		YGG:Cr8 powder X °C				YGG:Cr8.7 pellet X °C		
2-Theta (degree)	[h;k;l]	1000	1300	1400	1500	1000	1300	1400
29.12	[4;0;0]	0.2325	0.1526	0.1445	0.1641	0.1387	0.1526	0.1276
32.64	[4;2;0]	0.2452	0.1594	0.1490	0.1680	0.1442	0.1594	0.1246
35.85	[4;2;2]	0.2569	0.1650	0.1532	0.1694	0.1461	0.1650	0.125
51.60	[4;4;4]	0.3327	0.1915	0.1600	0.1724	0.1391	0.1915	0.1217
53.88	[6;4;0]	0.3458	0.1936	0.1600	0.1747	0.1398	0.1936	0.1177
56.08	[6;4;2]	0.3379	0.1989	0.1600	0.1756	0.1416	0.1989	0.1197
60.34	[8;0;0]	0.3866	0.2001	0.1600	0.1749	0.1407	0.2001	0.1163
68.38	[8;4;0]	0.4238	0.2020	0.1529	0.1547	0.1434	0.2020	0.1139
70.31	[8;4;2]	0.4188	0.2039	0.1459	0.1479	0.1403	0.2039	0.1138
72.22	[6;6;4]	0.3869	0.1969	0.1409	0.1431	0.1412	0.1969	0.1129
85.17	[8;6;4]	0.4944	0.1915	0.1265	0.1223	0.1512	0.1915	0.1143

The morphology of powders was investigated by SEM. The representative SEM micrographs are given in Fig. 36. The particle size of YGG:Cr8 powders increases with increasing temperature. The average size of particles synthesized at 1300 °C was ~705 nm, a 1400 °C – ~1.51 μm and at 1500 °C – ~2.04 μm.

The room temperature excitation and emission spectra of YGG:Cr8 powders annealed at 1000, 1300, 1400 and 1500 °C are shown in Fig. 37. The characteristic sharp and intense lines (the R-lines) correspondent to the $^2E \rightarrow {}^4A_2$ transitions are not well seen and are partially overlapped with a broad

emission band. The highest intensity of PL were observed from YGG:Cr8 powders prepared at 1500 °C, however, the highest intensity of excitation was observed from 1400YGG:Cr8 powders.

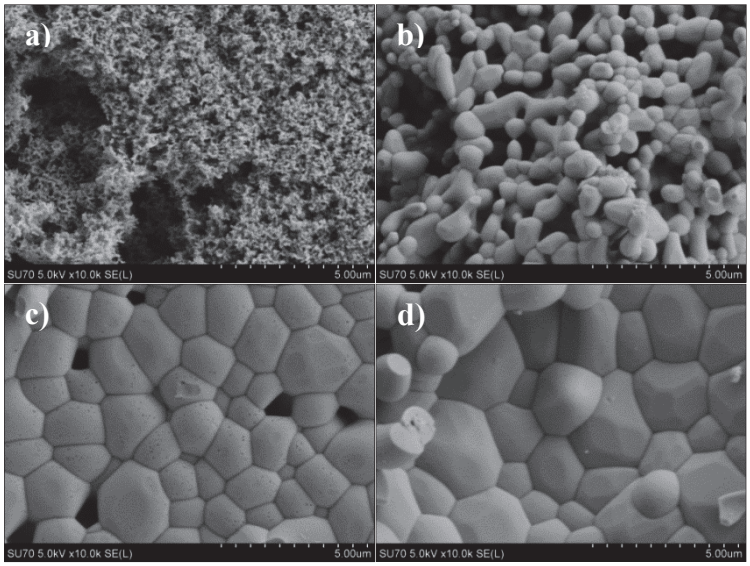

Fig. 36. SEM micrographs of YGG:Cr8 powders synthesized at 1000 °C (a), 1300 °C (b), 1400 °C (c) and 1500 °C (d).

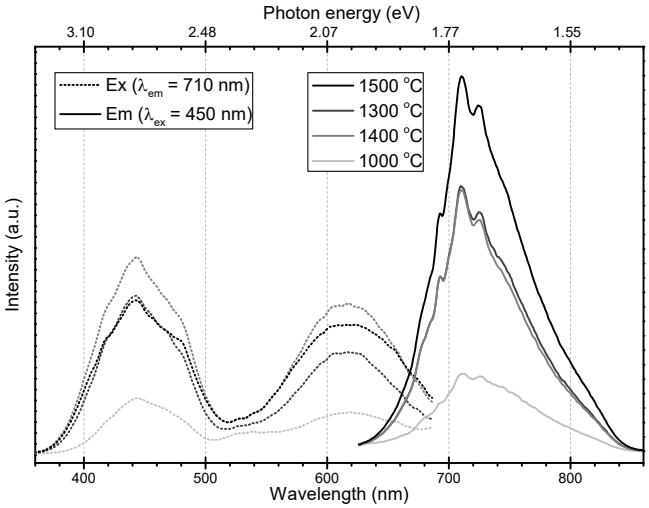

Fig. 37. Excitation and emission spectra of YGG:Cr8 powders annealed at 1000, 1300, 1400 and 1500 °C.

The Table 23 presents values of internal QE of both powders and pellets. The QE values of powder and pellet samples differ drastically despite that doping concentration is different only slightly. The pressing powders in to pellets promote growth of particles and increase crystallinity, which

significantly affects optical properties. The internal QE of YGG:Cr8.7 pellets reaches even 55%.

Table 23. The internal QE (%, λ_{ex} = 445 nm) values of the YGG:Cr8 powders and YGG:Cr8.7 pellets obtained at different temperatures.

Annealing temperature	QE (%) of the YGG:Cr8 powders	QE (%) of the YGG:Cr8.7 pellets
1000 °C	18	23
1100 °C	–	49
1200 °C	–	53
1300 °C	46	55
1400 °C	33	55
1500 °C	32	–

3.1.4.3. Investigation of $Lu_3Ga_5O_{12}:Cr^{3+}$ Garnets

In this section the results of characterization and PL properties of $Lu_3Ga_5O_{12}$ (LuGG) and Cr^{3+} doped LuGG powder samples will be discussed. The list of synthesized materials is given in a Table 24.

Table 24. The $Lu_3Ga_5O_{12}$ samples synthesized following synthesis III route.

Amount of Cr^{3+} mol%	$Lu_3Ga_5O_{12}$ (LuGG) (heated 1000 °C)	Preparation temperature (°C)	LuGG:Cr3
		1000	LuGG:Cr3
3	LuGG:Cr3	1300	1300LuGG:Cr3
5	LuGG:Cr5	1400	1400LuGG:Cr3
8	LuGG:Cr8	1500	1500LuGG:Cr3

XRD patterns of LuGG:Cr samples synthesized at 1000 °C are depicted in Fig. 38. It is clearly seen that XRD patterns of synthesized samples perfectly fit with the standard XRD data of $Lu_3Ga_5O_{12}$. Besides, the introduced amount of Cr^{3+} does not influence the phase purity of garnet.

The excitation and emission of LuGG:Cr were monitored at room temperature and the spectra are presented in Fig. 39. As it is seen the emission spectra of LuGG:Cr show inhomogeneous broad band width, and fluorescence is associated to the $^2E \rightarrow {}^4A_2$ transition. The decrease of the emission at 705 nm (λ_{ex} = 450 nm) intensities for the samples with higher concentration of Cr^{3+}

indicates that the $Cr^{3+} \leftrightarrow Cr^{3+}$ energy transfer occurs, which causes an increase of the nonradiative transition probability.

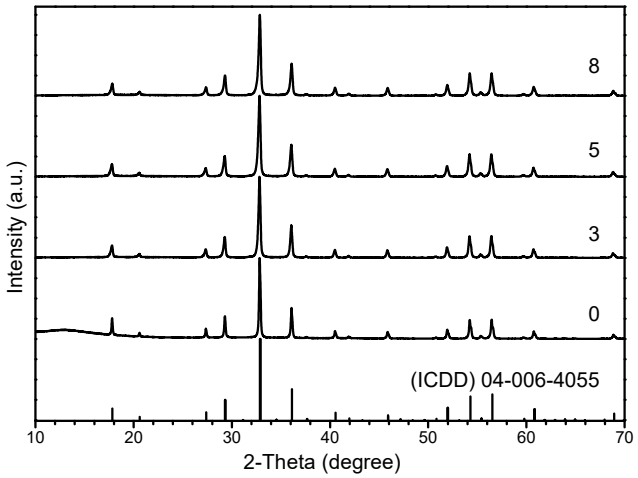

Fig. 38. XRD patterns of LuGG and Cr^{3+} doped LuGG samples. Vertical lines represent standard XRD data of $Lu_3Ga_5O_{12}$.

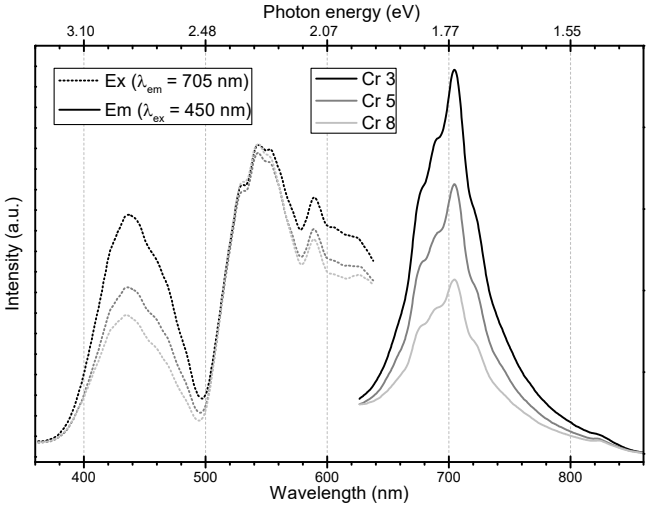

Fig. 39. Excitation and emission spectra of LuGG:Cr samples.

To gain insight of efficiency the internal QE were calculated from results of independently performed measurements in the sphere after 445 nm excitation. The QE results are presented in Table 25. The highest QE value (11%) is obtained for LuGG:Cr3.

Table 25. Values of the QE of the LuGG:Cr powder samples.

LuGG:Cr	3 mol%	5 mol%	8 mol%
Internal QE (%),λ_{ex} = 445 nm	11	6.5	3.6
λ_{ex} (nm)	549	547.5	549.5
λ_{em} (nm)	705	706	706

The LuGG:Cr3 powders were also prepared at 1300, 1400 and 1500 °C temperatures. XRD patterns of obtained samples are given in Fig. 40, and FWHM calculated for the most intensive peaks are listed in Table 26.

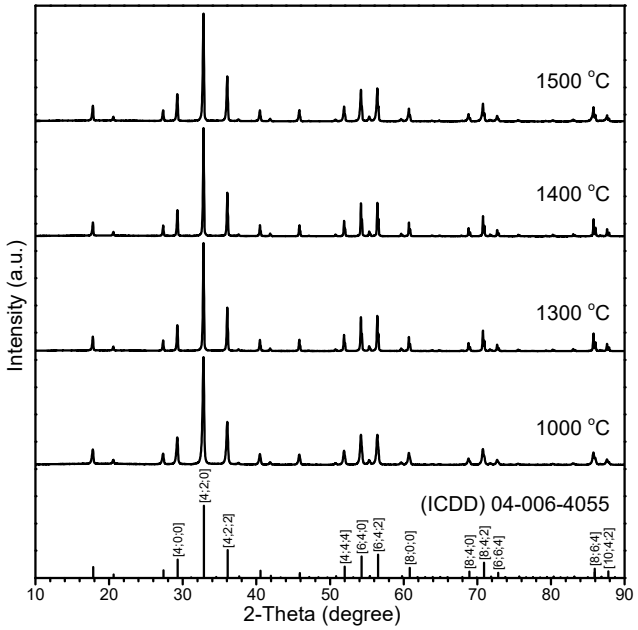

Fig. 40. XRD patterns of LuGG:Cr3 samples annealed at 1000 – 1500 °C temperatures. Vertical lines represent standard XRD data of LuGG.

Table 26. FWHM for most intensive XRD peaks of sintered LuGG:Cr3 powder samples.

(ICDD) 04-006-4055		FWHM			
2-Theta (degree)	[h;k;l]	1000 °C	1300 °C	1400 °C	1500 °C
29.32	[4;0;0]	0.1982	0.1211	0.1182	0.1429
32.88	[4;2;0]	0.2035	0.1205	0.1165	0.1434
36.12	[4;2;2]	0.1979	0.1196	0.1165	0.1472
52	[4;4;4]	0.1998	0.1141	0.1031	0.1487
54.3	[6;4;0]	0.2014	0.1144	0.1024	0.1524
56.54	[6;4;2]	0.2021	0.1145	0.1020	0.1587
60.84	[8;0;0]	0.2085	0.1139	0.1010	0.1548
68.94	[8;4;0]	0.2124	0.1123	0.1004	0.1585

It is seen that the garnet as cubic crystalline phase is determined in all LuGG:Cr3 samples. However, the calculated FWHM demonstrate unexpected increase of peak width for the XRD pattern of 1500LuGG:Cr3 sample. This might be associated with formation of defects, for instance microstrains [174].

The SEM micrographs are presented in Fig. 41. It is clearly seen that with increasing temperature from 1000 °C to 1500 °C the particle size increases drastically. Average size of particles heated at 1300 °C is ~689 nm, at 1400 °C – ~1.42 μm and at 1500 °C – ~1.81 μm.

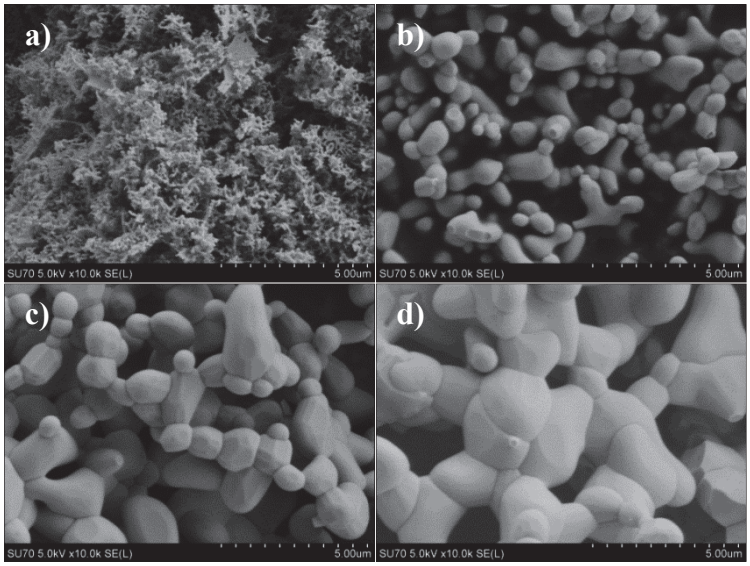

Fig. 41. SEM micrographs of LuGG:Cr3 powders annealed at 1000 °C (a), 1300 °C (b), 1400 °C (c) and 1500 °C (d).

The room temperature excitation and emission spectra of LuGG:Cr3 powders annealed at higher temperatures (1000, 1300, 1400 and 1500 °C) are shown in Fig. 42.

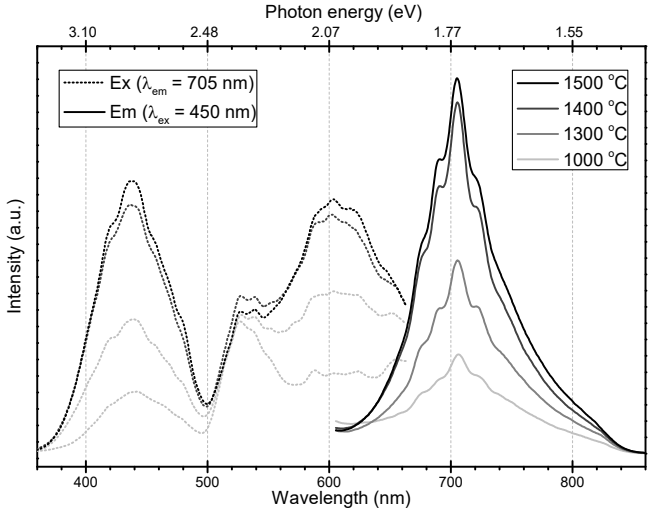

Fig. 42. Excitation and emission spectra of LuGG:Cr3 powder sintered at 1000, 1300, 1400 and 1500 °C temperatures.

Excitation bands with maxima near 450 and 600 nm correspond to the transitions of Cr^{3+} ions from the ground state to the excited levels. The investigated powder samples have a broad PL band in the far-red region due to the $^2E_2 \rightarrow {}^4A_2$ transition. There is a wide band in the spectral region 620 – 820 nm with a maximum at λ = 705 nm in the luminescence spectra of LuGG:Cr3 samples (λ_{ex} = 450 nm). The structure of ^2E level transition is not observed over an intensive luminescence background in a wide band corresponding to $^4T_2$-$^4A_2$ transitions. The notable increase of luminescence band intensity is observed when the sample preparation temperature is increased from 1000 to 1500 °C, possibly, due to the formation of more uniform crystallites with a better lattice quality at high temperature. However, the notable decrease of QE is observed (Table 27) for 1500LuGG:3 powders compared with 1400LuGG:Cr3 and 1300LuGG:Cr3.

Table 27. Optical properties of the LuGG:Cr3 powder samples.

LuGG:Cr3	1000 °C	1300 °C	1400 °C	1500 °C
Internal QE (%), λ_{ex} = 445 nm	11	19	20	17
λ_{ex}, nm	549	438	438	437
λ_{em}, nm	705	706	706	705

3.2. Synthesis and Characterization of Glaserite-Type Structure Compounds

3.2.1. Preparation of $Ca_3MgSi_2O_8$

Merwinite, $Ca_3MgSi_2O_8$ (CMSO), is the most famous member among this group of compounds. In this part of PhD thesis, the results on the sol-gel and solid-state syntheses of $Ca_3MgSi_2O_8$ are presented.

3.2.1.1. Peculiarities of Sol-Gel Processing

The TG-DTA curves of CMSO precursor glycolate gel are shown in Fig. 43.

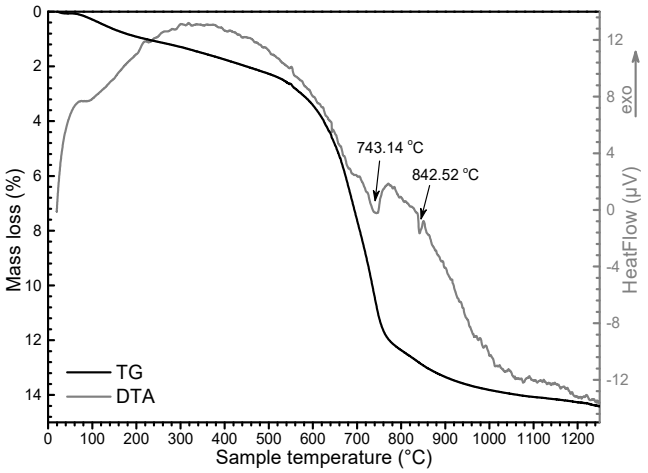

Fig. 43. TG-DTA curves of CMSO precursor gel obtained after heating at 500 °C.

The TG curve shows the monotonical mass loss till ~500 °C. At higher temperature the abrupt mass loss (11.6%) was observed with association of two endothermal processes determined at the 743 and 842 °C in the DTA curve. With further increasing the temperature, again the monotonical mass loss is seen in the TG curve. The total mass loss at 1200 °C is about ~15%. Thus, the heat treatment temperatures (500, 650, 800, 900, 1000, 1100 and 1200 °C) were chosen for the synthesis of CMSO phase.

The XRD patterns of the samples obtained at 500, 650 and 800 °C are presented in Fig. 44.

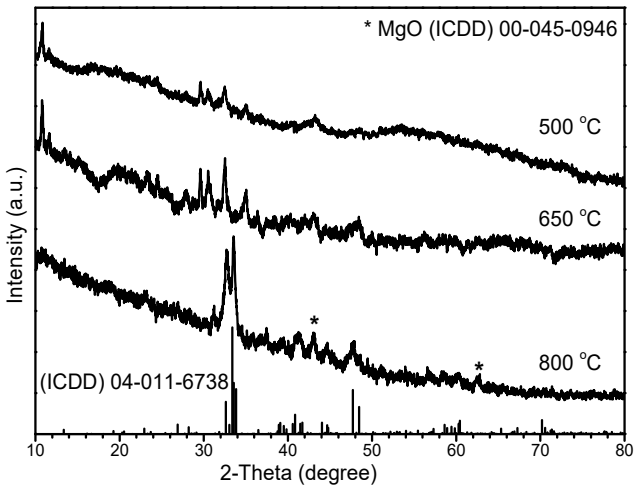

Fig. 44. XRD patterns of CMSO precursor powders heated at 500, 650 and 800 °C. Vertical lines represent standard XRD data of $Ca_3MgSi_2O_8$ (ICDD) 04-011-6738.

As it is seen from the XRD results, the desired monophasic compound is not obtained, however, the XRD pattern of the product heat-treated at 800 °C show intensive peaks attributable to merwinite. The XRD pattern also contains diffraction peaks attributable to the MgO impurity phase (ICDD 00-045-0946). Nevertheless, this temperature (800 °C) was chosen as pre-annealing temperature, because the TG results show the samples mass loss and at higher temperatures. The XRD patterns of the samples obtained at 900, 1000, 1100 and 1200 °C are depicted at Fig. 45.

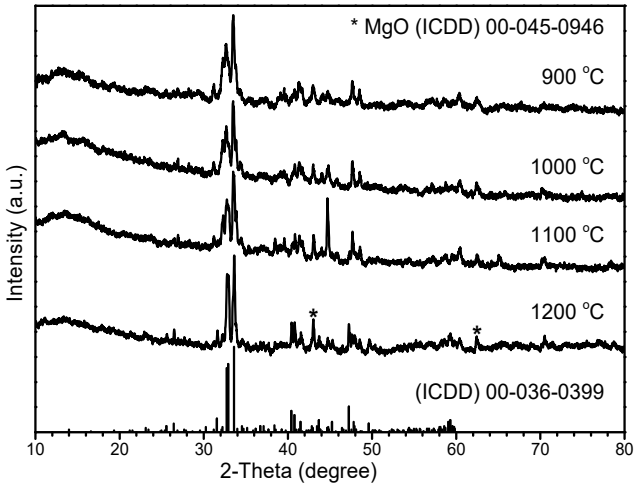

Fig. 45. XRD patterns of CMSO powders heated second time at 900, 1000, 1100 and 1200 °C. Vertical lines represent standard XRD data of $Ca_{14}Mg_2(SiO_4)_8$ (ICDD) 00-036-0399.

As it is seen, the single phase $Ca_3Mg(SiO_4)_2$ is not obtained after second heating at any higher temperature. Moreover, after heating at 1200 °C the more pronounced multiphasic product has formed. The calcium magnesium silicate, bredigite, ($Ca_{14}Mg_2(SiO_4)_8$) has formed as side phase in all of the cases. Orthorhombic $Ca_{14}Mg_2(SiO_4)_8$ (ICDD 00-036-0399) is the main phase of synthesis product prepared at 1200 °C, along with impurity MgO phase. Samples heated at lower temperatures (900 – 1100 °C) are composed from several phases and it is seen that MgO impurity phases is forming as well. After heating at 1000 °C, the XRD pattern of synthesis product fits with merwinite pattern, but the formation of minor amount of MgO phase is also determined.

Sol-gel synthesis of $Ca_3Mg(SiO_4)_2$ using TRIS as complexing agent and a fuel for self-combustion agent required different heating procedure. As self-propagated burning is not completely finished during heating on the hot-plate much slower furnace heating procedure was chosen. The temperature was increased up to 500 °C by 1 °C/min and held for 4 h, then additionally heated for 4 h at 600 °C. The last heating for 4 h was performed at 800 °C. The XRD patterns of resulted powders are presented in Fig. 46. Despite some impurities of MgO and SiO_2, the main phase of merwinite was obtained [119] and (ICDD 00-011-6738). However, the peaks at $2\theta = 30^o$ and 32^o were not attributed to any crystalline phase.

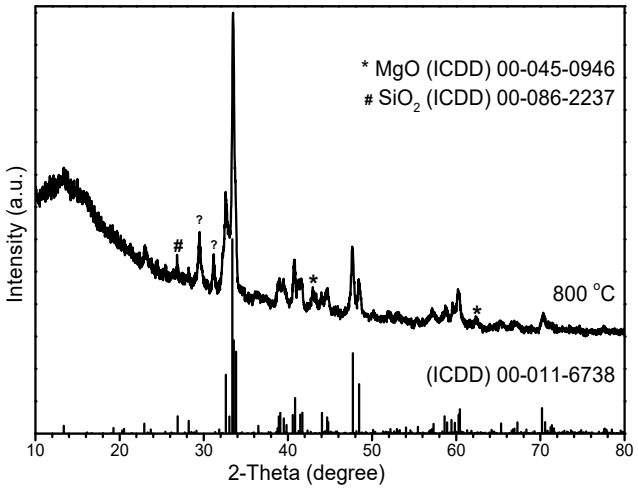

Fig. 46. XRD patterns of sol-gel derived CMSO using TRIS prepared at 800 °C. Vertical lines represent standard XRD data (ICDD) 00-011-6738 of $Ca_3MgSi_2O_8$.

3.2.1.2. Solid-State Reaction Synthetic Approach

In the solid-sate synthesis the necessary amounts of starting materials were mixed by ball mill and dried. The TG-DTA curves of dried precursor mixture are shown in Fig. 47. Five thermal events at ~115, ~237, 379, 583 and 789 °C could be observed in the DTA curve. The slope of TG curve at ~115 °C is related to the dehydration of magnesium precursor. According to literature [183] this process could last till 250 °C. In the temperature range of 250 – 350 °C, the $4MgCO_3 \cdot Mg(OH)_2$ decomposes to $MgCO_3$ and MgO. However,

NH_4Cl, used as a flux, melts in the same temperature range (338 °C). The mass loss observed at highest temperature, ~779 °C, accompanied with very intensive endothermic peak in the DTA curve, is associated to the decomposition of $CaCO_3$. The total mass loss (35.3%) calculated from the TG curve is almost the same as theoretical (37.74%).

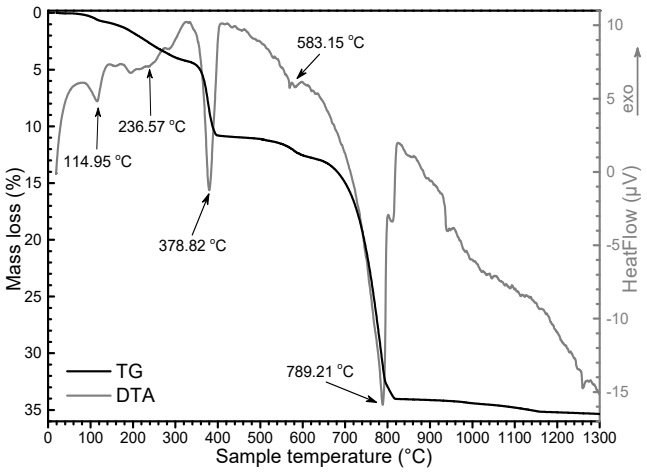

Fig. 47. TG-DTA curves of mixture of starting materials for CMSO after ball milling and drying.

Fig. 48 represents XRD patterns of the synthesis products obtained by heating the precursor mixtures at 1150, 1200 and 1250 °C.

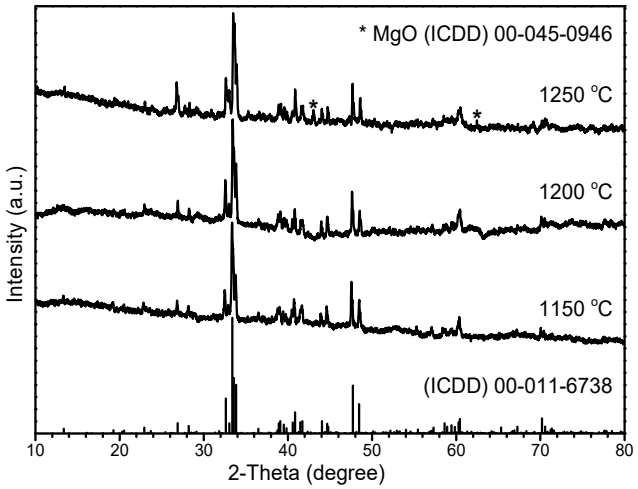

Fig. 48. XRD patterns of CMSO samples prepared by solid-state method at different temperatures. Vertical lines represent standard XRD data of $Ca_3MgSi_2O_8$ (ICDD) 00-011-6738.

As seen from XRD patterns, the monophasic $Ca_3Mg(SiO_4)_2$ was obtained only at 1200 °C. Interestingly, a little variation of temperature (by 50 °C) has strong effect on the phase purity of end product. The both sample, annealed at 1150 and 1250 °C contain MgO impurity phase.

3.2.2. Preparation of $Ba_3CuSi_2O_8$

In this part of PhD thesis, the results on the sol-gel, solid-state syntheses and TSFZM of barium and copper substituted $Ba_3Cu(SiO_4)_2$ (BCSO) compound are presented.

3.2.2.1 Peculiarities of Sol-Gel Processing

The attempt to prepare BCSO compound with glaserite-type structure using sol-gel processing with 1,2-ethylenglycol (1SG-BCSO) or TRIS (2SG-BCSO) was investigated. The samples were prepared according to previously developed sol-gel syntheses methods for the pure $YBa_2Cu_4O_8$ [184, 185] and strontium-substituted $Y(Ba_{1-x}Sr_x)_2Cu_4O_8$ superconductors [186]. Self-burning processes were initiated on hot plate, and remaining powders were analysed using TG-DTA (Fig. 49).

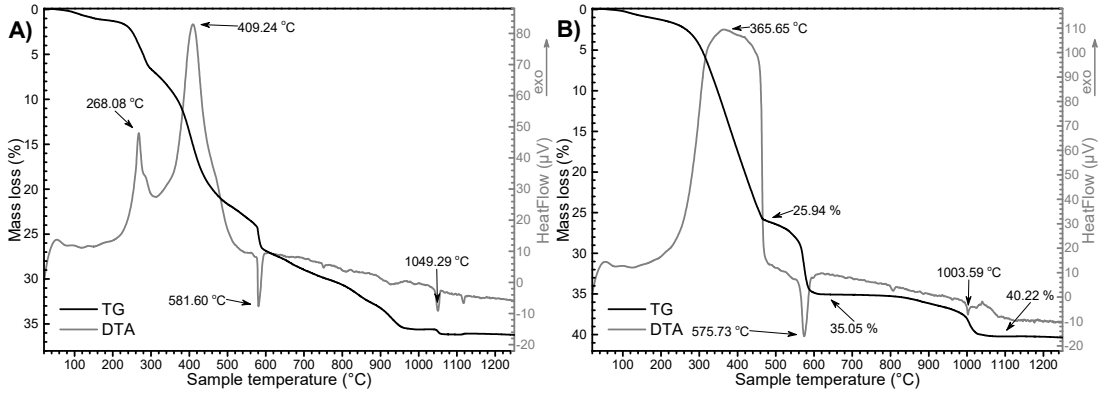

Fig. 49. TG-DTA curves of 1SG-BCSO (A) and of 2SG-BCSO (B) samples after self-burning processes.

From the TG curves we can see that the mass loss for both samples is more than 36% in the measured temperature range. The decomposition of 1SG-BCSO sample occurs via five stages at ~270, ~410, 582, 960 and 1050 °C. While 2SG-BCSO sample decomposes in three stages at 366, 576

and 1004 °C. Thermogravimetric behaviour till ~260 °C is likely similar for both gel samples, however, the main decomposition of gels in the temperature range of 260 – 570 °C differs essentially. The 1SG-BCSO sample decomposes in two stages at 268 °C and 408 °C which are associated with the decomposition of metal coordination compounds with ethylene glycol. This process is related with exothermic process seen in the DTA curve [187]. The exothermic decomposition of 2SG-BCSO sample in the range of 250 – 460 °C is attributed to the decomposition of metal coordination compounds with TRIS (mass loss ~20%). For both analysed samples the endothermic peaks at ~570 – 580 °C in the DTA curves were observed, which could be associated to the decomposition of remaining $Ba(NO_3)_2$. The mass loss in the temperature range of 800 – 1000 °C corresponds to the decomposition of $BaCO_3$. The endothermic peak seen at 1042 °C in the DTA curve of 1SG-BCSO sample could be attributed to the reduction of CuO to Cu_2O [188].

The 1SG-BCSO and 2SG-BCSO samples after self-burning processes were pressed in to pellets and preheated at 500 and 600 °C. As seen from Fig. 50, in the case of 1SG-BCSO samples the desired phase has not formed. The main crystalline phase is $BaCO_3$. However, in the case of 2SG-BSCO, different phases have formed after self-burning process ($BaCO_3$, $Ba(NO_3)_2$, CuO), after heating at 500 °C ($BaCO_3$) and after heating at 600 °C ($BaCO_3$, Ba_2SiO_4).

SEM-EDX analyses were performed for both 1SG-BCSO and 2SG-BCSO samples heated at 600 °C. Obtained results showed that elemental distribution in the samples is homogeneous. However, elemental ratio in the 2SG-BCSO sample (Ba:Cu:Si = 2.5:1.1:1) is different from the desired (Ba:Cu:Si = 3:1:2). Thus, the $Ba_3Cu(SiO_4)_2$ phase was not obtained during both sol-gel processing routes.

The 1SG-BCSO sample after preheating at 600 °C was re-grinded and secondly pressed in to pellet and then heated at 1000 °C for 24 h. XRD pattern of 1SG-BCSO sample calcined at 1000 °C temperature is depicted at Fig. 51. Apparently the mixture of phases (Ba_2SiO_4, CuO and $BaCO_3$) was obtained.

Ba_2SiO_4 is formed as a main phase. Consequently, further heating procedure does not promote the phase formation.

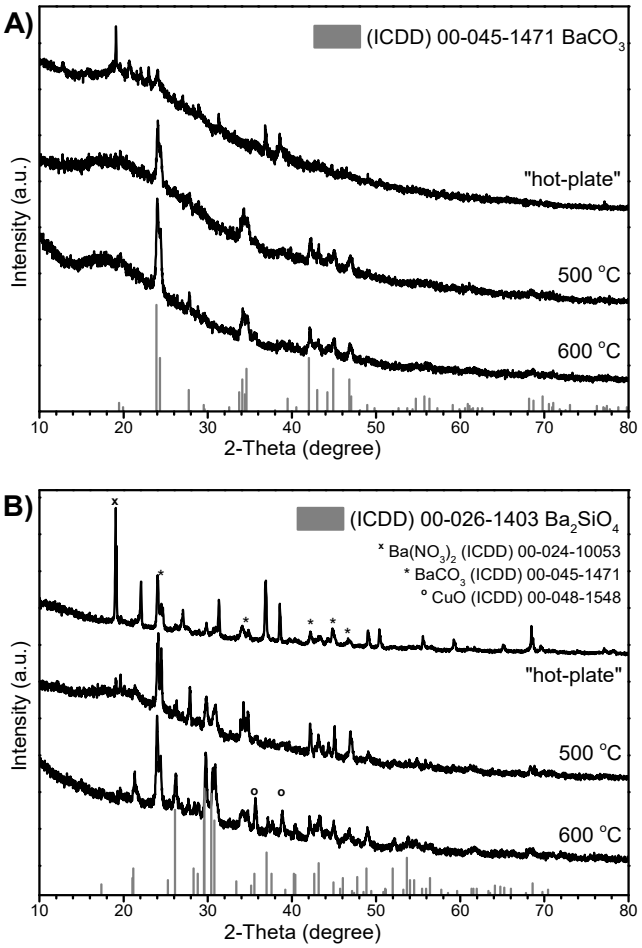

Fig. 50. XRD patterns of 1SG-BCSO (A) and 2SG-BCSO (B) samples, after self-burning processes and heated at 500 °C and 600 °C temperatures. Vertical lines represent standard XRD data.

3.2.2.2. Solid-State Reaction Synthetic Approach

The attempt to prepare $Ba_3CuSi_2O_8$ (BCSO) compound with glaserite-type structure using solid-state reaction from starting materials $BaCO_3$, CuO and SiO_2 was investigated. The sample is named 1SS-BCSO.

The homogenized and dried (1SS-BCSO) precursors were analysed by TG-DTA method (Fig. 52).

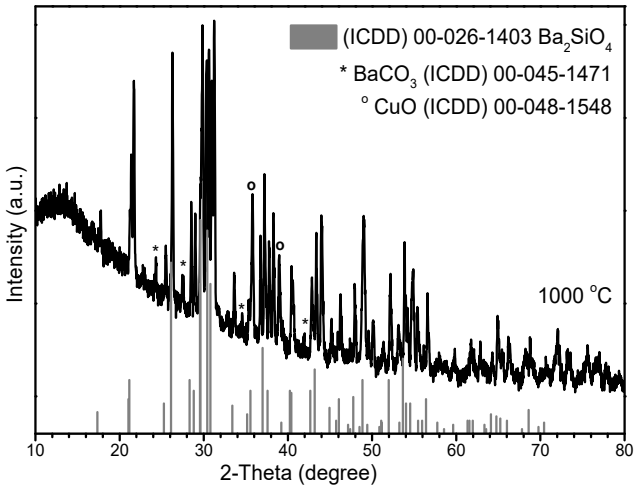

Fig. 51. XRD pattern of 1SG-BCSO sample heated at 1000 °C. Vertical lines represent standard XRD data of Ba_2SiO_4 (ICDD) 00-025-1403.

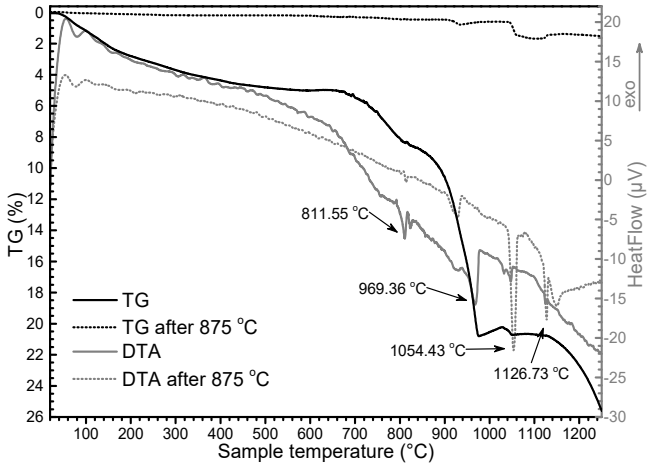

Fig. 52. TG-DTA curves of mixture of starting materials for 1SS-BCSO and preheated mixture at 875 °C samples.

The TG curve of precursor showed that complete mass loss up to 1200 °C is not obtained. Therefore, in order to achieve full decomposition of $BaCO_3$ the prepared mixture of starting materials was pre-heated at 875 °C for 12 h, and the TG-DTA measurement was performed on the pre-heated sample. From both DTA curves is seen that decomposition is accompanied by three endothermic peaks at 812, 963 and 1054 °C, which are assigned to the decomposition of $BaCO_3$, formation of Ba_2SiO_4 phase and CuO reduction to Cu_2O, respectively. The small increase of mass at 1127 °C is obtained only for the pre-heated sample. Thus, the 1SS-BCSO sample was second time annealed

at higher temperature of 1075 ºC for 12 h. Both obtained samples, before and after second annealing, are composed of several phases (Fig. 53).

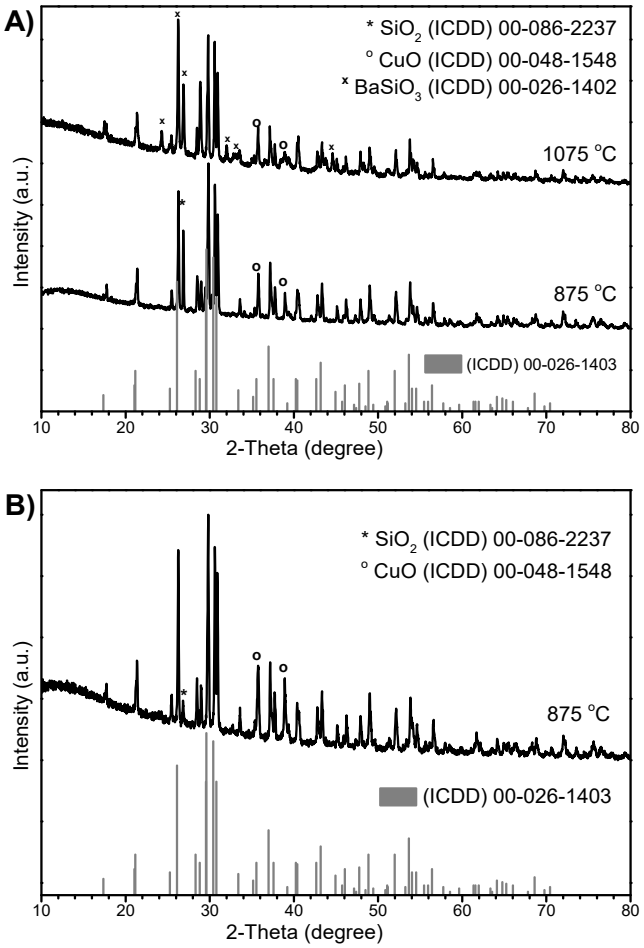

Fig. 53. XRD patterns of 1SS-BCSO samples heated at 875 °C (A) and 1075 °C and 2SS-BCSO sample heated two times at 875 °C (B). Vertical lines represent standard XRD data of Ba_2SiO_4 (ICDD) 00-026-1403.

The 1SS-BCSO sample obtained at 875 °C still contains very small amount of $BaCO_3$. However, the obtained main phase is orthorhombic Ba_2SiO_4 ((ICDD) 00-0260-1403) and minor amount of CuO and $BaCuO_2$ phases also exists. The XRD pattern of the sample obtained at 1075 °C contains reflections of both $BaSiO_3$ and Ba_2SiO_4 phases. The 1SS-BCSO sample heated at 1075 °C has CuO and SiO_2 impurities as well.

In the next step, the BaO_2 was selected as starting Ba source instead of $BaCO_3$. The synthesized sample was named as 2SS-BCSO. The XRD pattern of the 2SS-BCSO sample is given at Fig. 53 (B). Again, the main phase is

orthorhombic Ba_2SiO_4 and no traces of barium copper silicate have formed. The CuO impurity phase is also well seen in the XRD pattern.

According to BaO-SiO_2 phase diagrams published in [189, 190], the Ba_2SiO_4 phase is forming at low temperature and is stable till 1877 °C, and at around 1050 °C, the formation of $Ba_3CuSi_2O_8$ compound could be possible:

$$2BaCO_3 + SiO_2 \rightarrow Ba_2SiO_4 + 2CO_2 \quad (3)$$

$$2Ba_2SiO_4 + 2BaO_2 + 2CuO + 2SiO_2 \rightarrow 2Ba_3CuSi_2O_8 + O_2 \quad (4)$$

Single phase Ba_2SiO_4 powders were obtained after pre-heating at 875 °C and annealing at 1075 °C of mixture of $BaCO_3$ and SiO_2. The obtained monophasic Ba_2SiO_4 powders along with CuO and SiO_2 were mixed and annealed at 1075 °C for 24 h. The TG-DTA analysis of prepared mixture showed endothermic DTA peak at around 1050 °C and sample mass loss less than 2% (1.7%) up to 1250 °C. However, the XRD pattern of product obtained at 1075 °C (Fig. 54) show that Ba_2SiO_4 phase is the main in the sample.

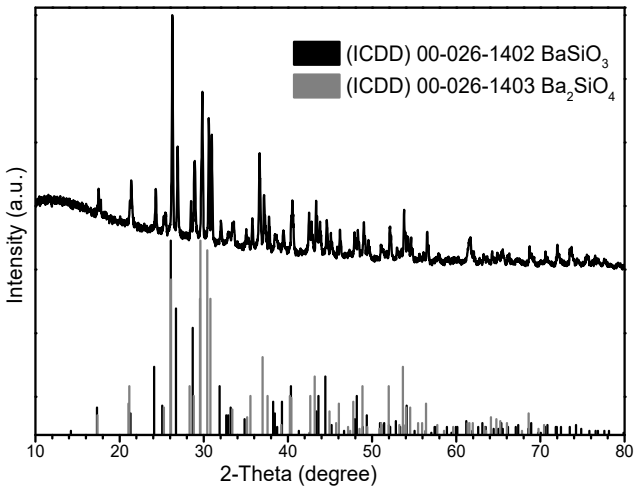

Fig. 54. XRD pattern of Ba_2SiO_4, CuO and SiO_2 mixture heated at 1075 °C. Vertical lines represent standard XRD data.

In conclusion, the suggested synthesis pathways were not fruitful and no trace of $Ba_3CuSi_2O_8$ phase was obtained. For further investigations, as possible route might be used the following reaction:

$$2Ba_2Si_3O_8 + 2Ba_2CuO_3 + BaCuO_2 \rightarrow 3Ba_3CuSi_2O_8 \quad (5)$$

Since the starting materials $BaCuO_2$ (mp 1060 °C), Ba_2CuO_3 (mp 987 °C) and $Ba_2Si_3O_8$ (mp 1447 °C) have comparably low melting

temperatures the reaction (5) could be promising to obtained the desired compound.

3.2.2.3. Travelling Solvent Floating Zone Method

The TSFZM was used for the synthesis of $Ba_3CuSi_2O_4$ single crystal. The cuts of as prepared rods and after processing at TSFZM crystal growth furnace were analysed by XRD and SEM-EDX (Fig. 55-57, Table 28).

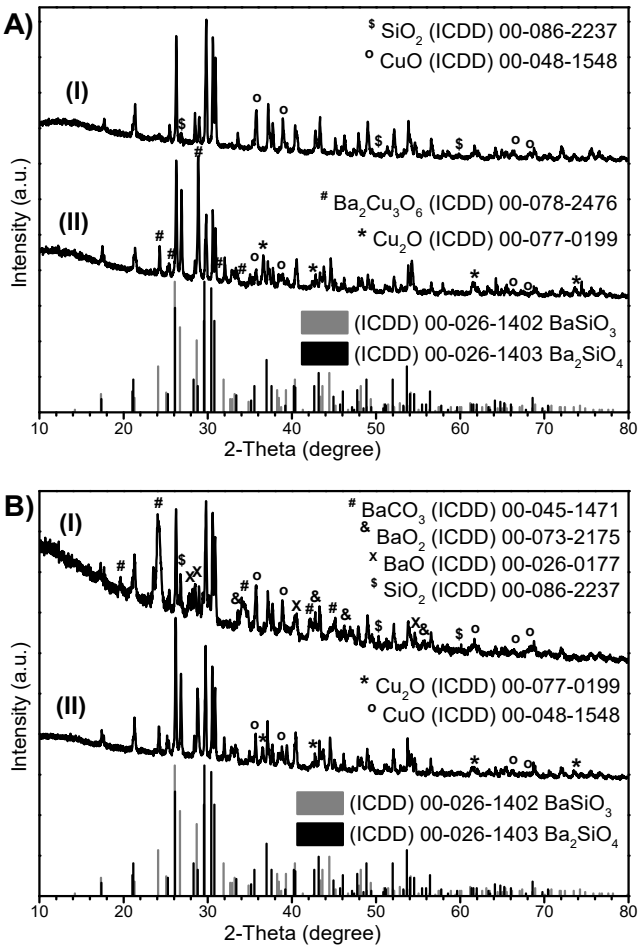

Fig. 55. XRD patterns of prepared rods (I) and middle of product rods (II) after 1I-BCSO (A) and 2I-BCSO (B) processing.

Feed and seed rods were prepared from the mixtures of precursor materials and used for the growth processes. Due to the non-congruently melting of materials in the prepared rods and very large melting temperature difference the unstable melt was caused during the growth, and optimal growth conditions were not found.

The small pieces of the final polycrystalline product were cut by diamond saw from lower and upper parts, which correspond to the beginning and ending of growth, respectively. The XRD patterns show that in the prepared rods there are larger or smaller amounts of Ba_2SiO_4 phase, especially in the case of 1I-BCSO. Besides, the small amount of SiO_2 still remains unreacted. Fast preheating (1 h) at 900 °C of 2I-BCSO rod stimulates formation of $BaCO_3$, Ba_2SiO_4 and $BaSiO_3$ phases with unreacted SiO_2. Moreover, the rod also contains small amount of CuO, BaO and BaO_2 phases. Large amount of $BaCO_3$ was formed in the case of 3I-BCSO as well. However, this phase decomposes during second heating at TSFZ furnace.

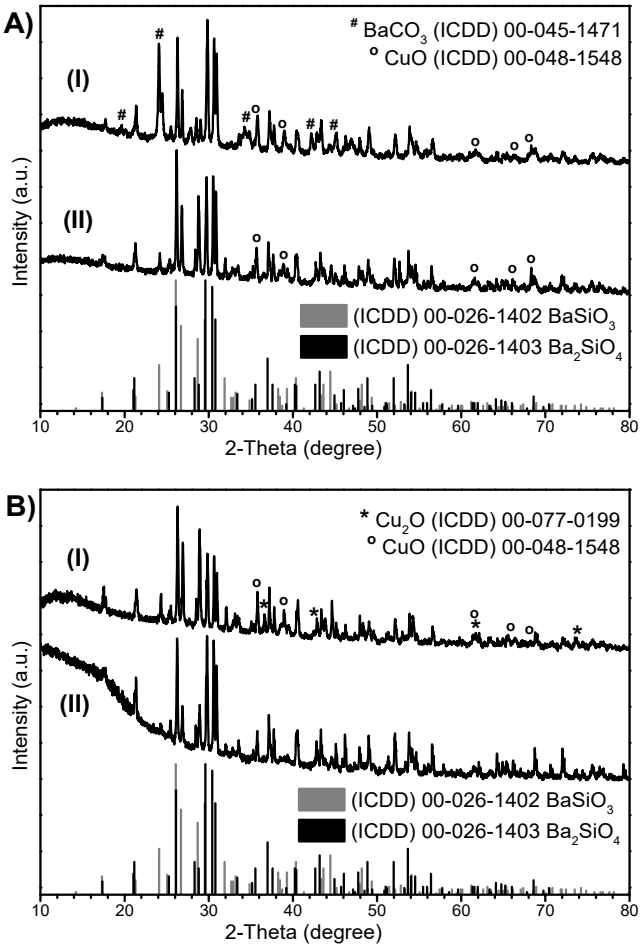

Fig. 56. XRD patterns of prepared rods (A) and cuts from product rod (B) from 3I-BCSO process. XRD pattern of preheated at 750 °C is (I) and pattern (II) of second time heated in the TSFZM furnace (A). XRD pattern (I) is cut from bottom and pattern (II) is cut from top of product after processing at TSFZM (B).

The XRD patterns of samples after processing in TSFZ furnace contain peaks attributable to barium silicates and copper oxides phases, and in some cases barium cuprate phase. The XRD results from cuts of 3I-BCSO product from bottom and upper parts of rod show the formation of $BaSiO_3$ and Ba_2SiO_4 phases. However, a copper oxide does not form at the end of processing. These results imply that compound with copper has lower melting temperature and could be lost during the growth by unstable melt.

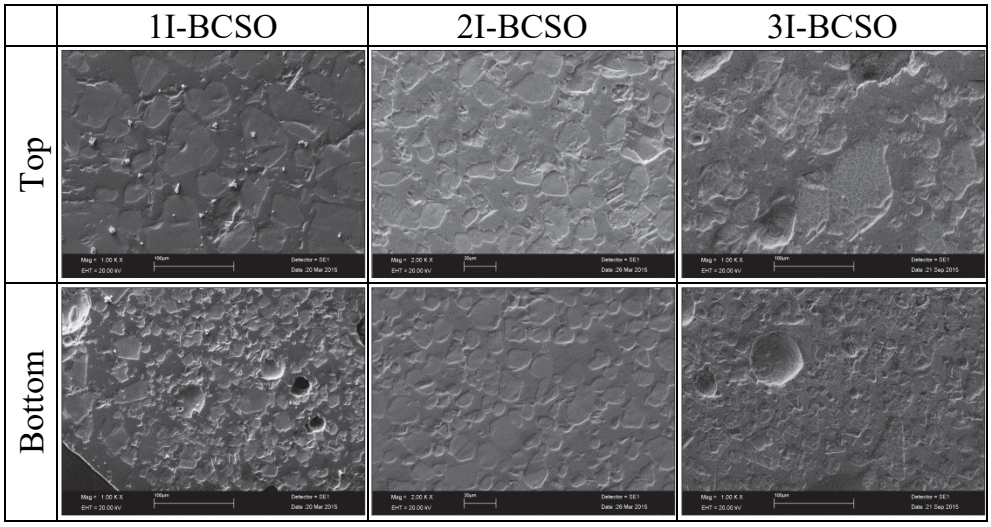

Fig. 57. SEM micrographs of upper (at top) and bottom cut parts from rods after 1I-BCSO, 2I-BCSO and 3I-BCSO TSFZM processing.

Table 28. The elemental composition of the TSFZM derived samples determined by EDX.

Sample		Atom%			Atomic ratio		
		Ba	Cu	Si	Ba : Cu : Si		
1I-BCSO	Top	44.73	11.79	43.48	3.79	1.00	3.69
	Bottom	49.70	7.94	42.35	6.26	1.00	5.33
2I-BCSO	Top	45.28	12.11	42.61	3.74	1.00	3.52
	Bottom	45.32	9.04	45.63	5.01	1.00	5.05
3I-BCSO	Top	40.17	7.26	52.57	5.53	1.00	7.24
	Bottom	37.71	7.99	54.29	4.72	1.00	6.79

The Fig. 57 presents SEM micrographs of cut pieces from 1I-BSCO, 2I-BSCO and 3I-BSCO products. It is seen, that phases are strongly separated and crystals at the upper parts from rods are larger in comparison with cut from bottom parts. The results in the Table 28 represent average elemental

composition at the beginning and at the end of growth process. Surprisingly, the desired elemental ratio of Ba:Cu:Si = 3:1:2 is not achieved in all presented samples.

3.2.3. Preparation of $Ca_3Mg_{1-x}Cu_xSi_2O_8$

There are many of articles about synthesis, structure or properties of compounds when calcium is replaced by barium or strontium in the $Ca_3Mg(SiO_4)_2$. However, in our knowledge, were no publications when magnesium is replaced by other elements like copper or nickel. The attempt to prepare $Ca_3Mg_{1-x}Cu_x(SiO_4)_2$ compound using sol-gel and solid-state reaction methods was aimed in this part of thesis.

3.2.3.1. Peculiarities of Sol-Gel Processing

The XRD patterns of $Ca_3Mg_{0.9}Cu_{0.1}Si_2O_8$ (SG-CMC1SO) and $Ca_3Mg_{0.8}Cu_{0.2}Si_2O_8$ (SG-CMC2SO) samples prepared by sol-gel synthesis are presented at Fig. 58. The XRD patterns of both resulting powders show that samples are composed of few phases (merwinite phase is overlapping with bredigite (formula $Ca_{14}Mg_2(SiO_4)_8$), CuO and MgO). Thus after first heating at 800 °C SG-CMC2SO powder were split in to two parts, from one part pellet were pressed. The second heating performed at 1050 °C. The obtained powdered and pelletized products contain the mixture of merwinite, bredigite and MgO phases. It is clearly seen that pellet sample has better crystallinity with the main bredigite phase.

3.2.3.2. Solid-State Synthesis Approach

The $Ca_3Mg_{0.8}Cu_{0.2}Si_2O_8$ compound was synthesized using the same conditions as for $Ca_3MgSi_2O_8$. The $Cu_2(CO_3)(OH)_2$ (sample 1SS-CMC2SO) and CuO (sample 2SS-CMC2SO) were used as a Cu source. The XRD patterns of the synthesis products obtained at 1200 °C are presented at Fig. 59. The flux (NH_4Cl) was used in this synthesis. The XRD patterns of both samples show that obtained products are not single phase, and mixture of merwinite and bredigite with MgO impurity has formed.

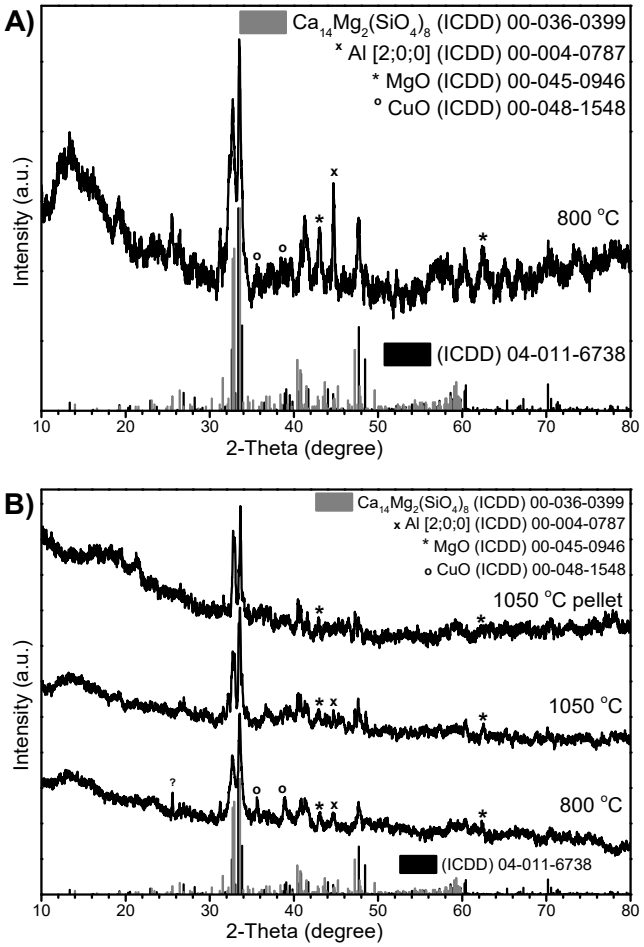

Fig. 58. XRD patterns of SG-CMC1SO (A) and SG-CMC2SO (B) samples heated at 800 and 1050 °C temperatures. Vertical lines represent standard XRD data of $Ca_3MgSi_2O_8$ (ICDD) 04-011-6738.

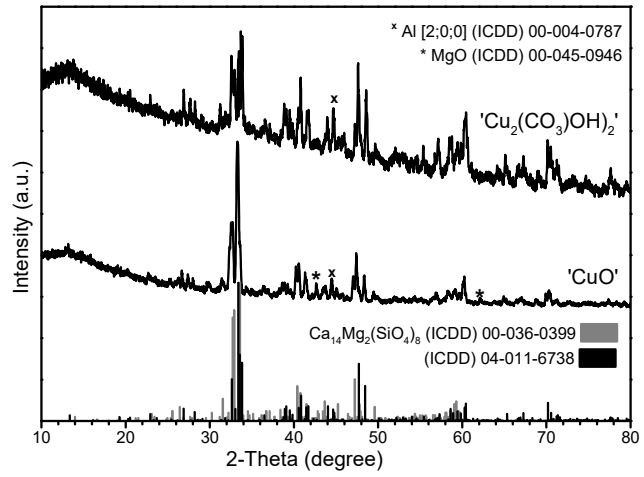

Fig. 59. XRD patterns of 1SS-CMC2SO and 2SS-CMC2SO samples heated at 1200 °C. Vertical lines represent standard XRD data of $Ca_3MgSi_2O_8$ (ICDD) 04-011-6738.

3.2.4. Preparation of $Ba_{3-x}Ca_xCuSi_2O_8$

In order to overcame Ba_2SiO_4 phase formation it was decided to try obtain eutectic point of $CaSiO_3$:$BaSiO_3$ by weight percentage 28:72 (wt%) at 1268 °C according phase diagram [191]. The idea was to get final compound $Ba_{2.166}Ca_{0.833}CuSi_2O_8$ (BCCSO) from homogeneous liquid which should form at higher temperature than 1268 °C by mixing $BaCuO_2$, $BaSiO_3$ and $CaSiO_3$. For this purpose separately $BaSiO_3$, $CaSiO_3$ and $BaCuO_2$ compounds were synthesized by solid-state method (Fig. 60) and mixed together in a ratio following chemical reaction:

$$5CaSiO_3 + 7BaSiO_3 + 6BaCuO_2 \rightarrow 6Ca_{\frac{5}{6}}Ba_{\frac{13}{6}}CuSi_2O_8 \qquad (6)$$

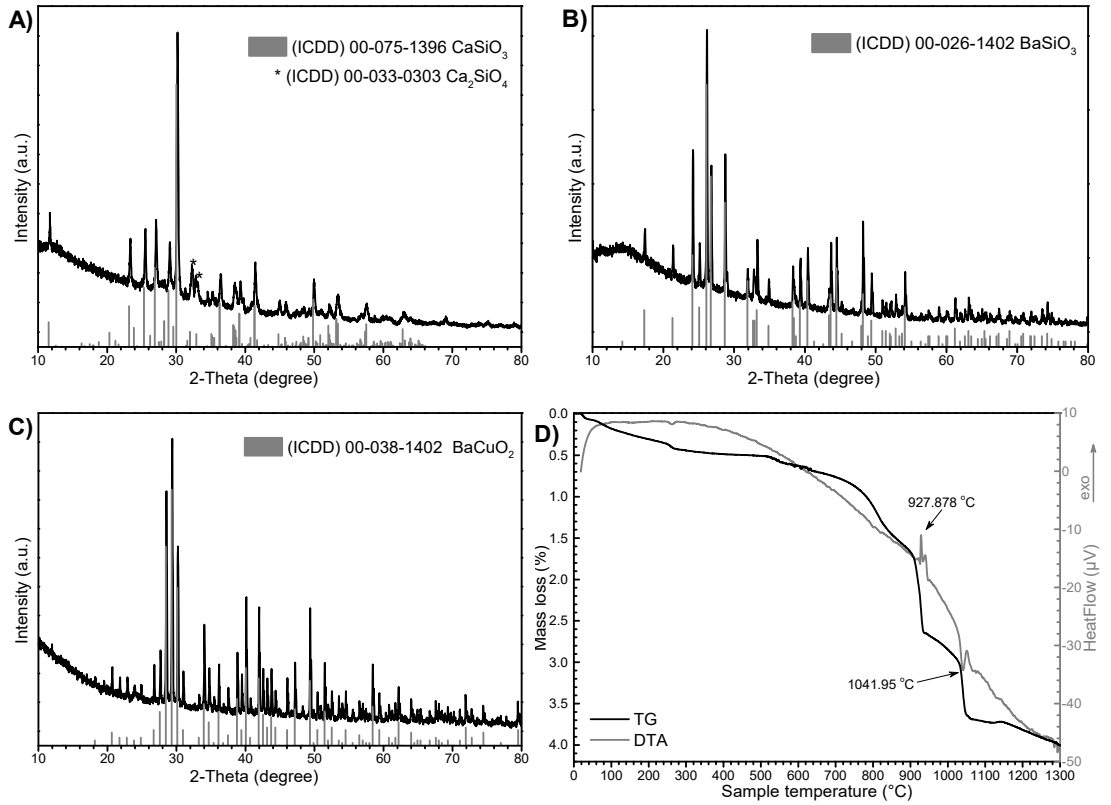

Fig. 60. XRD patterns of synthesized $CaSiO_3$ (A), $BaSiO_3$ (B) and $BaCuO_2$ (C), where vertical lines represent standard XRD data. TG-DTA curves of oxides mixture for $Ba_{2.166}Ca_{0.833}CuSi_2O_8$ (D).

The mixture of starting materials was investigated by simultaneous TG-DTA (Fig. 60, (D)). From the TG curve, the mass loss less than 4% of up to 1300 °C was observed. Thermal decomposition occurs via three stages at 800, 928 and 1040 °C. The mass loss at ~800 °C is accompanied by very weak

exothermic peak in the DTA curve which could be associated to the decomposition of remaining $BaCO_3$ or $CaCO_3$ carbonates. The second mass loss and exothermic process is associated to the transformation of $BaSiO_3$ and $CaSiO_3$ to Ba_2SiO_4 or Ca_2SiO_4 or mixture of them [192]. At 1040 °C the reduction of CuO to Cu_2O, with a weight loss occurs [188]. The eutectic points are not seen as it was expected, because temperatures are at the limit of measuring with this equipment. However, the small mass loss in the TG curve observed at temperatures higher than 1150 °C might be associated with the beginning of melting.

Powder mixture as prepared for the BCCSO compound was pressed in to two pellets. The first pellet (BCCSO1) was heated three times for 24 h with intermediate grindings at 960, 980 and 1000 °C respectively. The second pellet (BCCSO2) was directly heat treated at 1000 °C for 24 h. The XRD patterns of synthesis products are presented in Fig. 61. As seen, the orthosilicates have formed and CuO phase is forming separately.

The SEM-EDX analysis results are presented at Fig. 62 and Fig. 63 and Table 29 and Table 30. As seen, both samples have inhomogeneous elemental distribution. The BCCSO1 sample after three heating steps consists of separate crystalline phases with clearly expressed borders. While SEM micrographs of BCCSO2 do not show the existence of borders separating different phases, however areas which have other elemental content are clearly seen.

The TG-DTA, XRD and SEM-EDX analyses results prove the formation of $Ba_{2-x}Ca_xSiO_4$ phase. As this phase is extremely stable (melting temperature ~1877 °C) there is no reason for further heating. Nevertheless, obtained information is useful for further investigations, because this mixture of compounds possibly could be used for TSFZM.

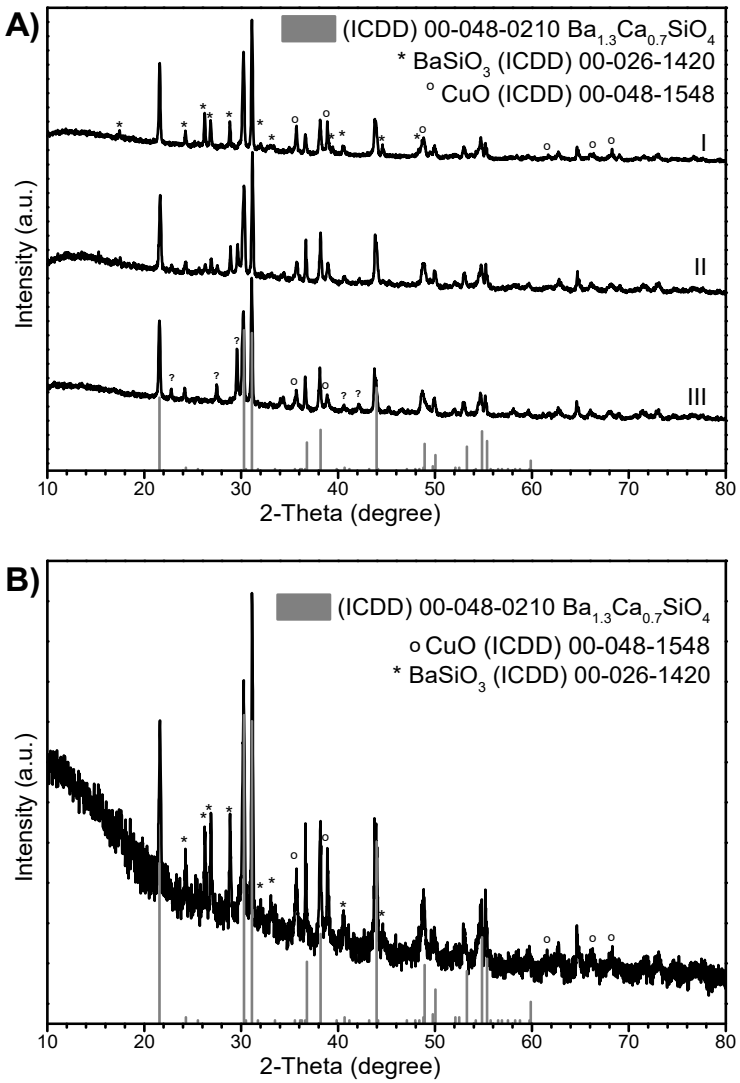

Fig. 61. XRD patterns of BCCSO1 after repeated heating (A) and BCCSO2 (B). Vertical lines represent standard XRD data of $Ba_{1.3}Ca_{0.7}SiO_4$, (ICDD) 00-048-0210.

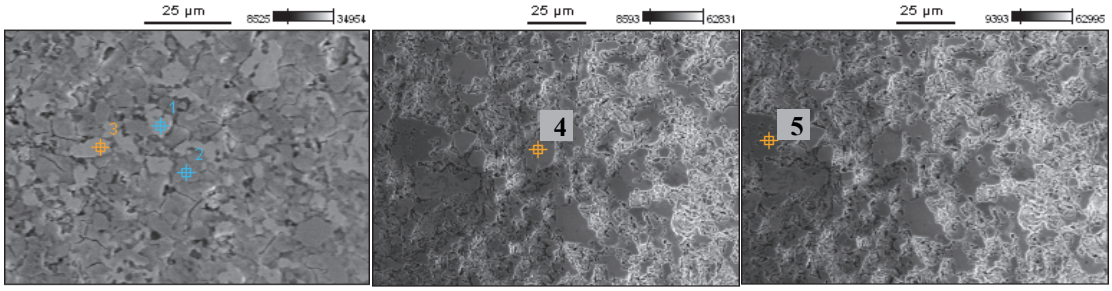

Fig. 62. SEM micrographs of BCCSO1. The spots of EDX analysis are numbered.

Table 29. EDX elemental distribution of sample BCCSO1.

Spot	Atom%				Atomic ratio			
	Ba	Ca	Cu	Si	Ba : Ca : Cu : Si			
1	32.02	3.24	5.82	58.92	9.88	1.00	1.80	18.18
2	8.09	4.53	78.25	9.12	1.79	1.00	17.27	2.01
3	31.61	4.90	8.92	54.57	6.45	1.00	1.82	11.14
4	30.47	2.69	5.66	61.18	11.33	1.00	2.10	22.74
5	–	24.49	14.43	61.08	–	1.70	1.00	4.23

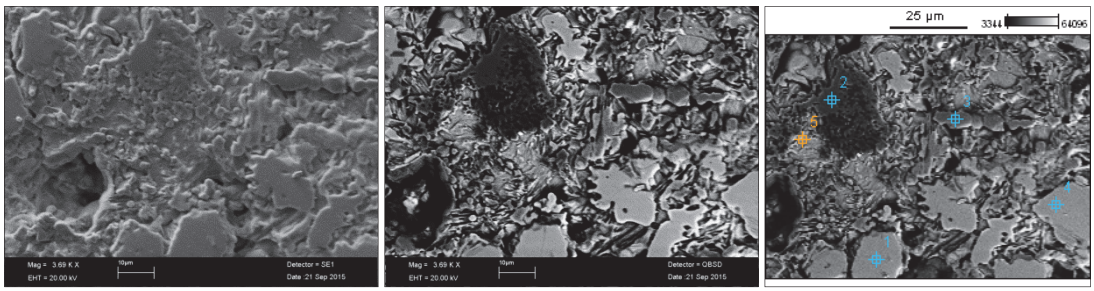

Fig. 63. SEM micrographs of BCCSO2. The spots of EDX analysis are marked.

Table 30. EDX elemental distribution of sample BCCSO2.

Spot	Atom%				Atomic ratio			
	Ba	Ca	Cu	Si	Ba : Ca : Cu : Si			
1	33.80	–	0.30	65.90	112.67	–	1.00	219.67
2	11.27	28.67	–	60.06	1.00	2.54	–	5.33
3	26.37	19.78	8.07	45.78	3.27	2.45	1.00	5.67
4	47.03	14.61	–	38.36	3.22	1.00	–	2.63
5	30.86	29.45	–	39.69	1.05	1.00	–	1.35

CONCLUSIONS

1. Three sol-gel synthesis routes were developed for the synthesis of single phase $Gd_3Sc_2Ga_3O_{12}$ (GSGG) garnet. It was demonstrated that the synthesis using TRIS as a complexing agent in the sol-gel processing ensure the formation of particles with narrow particle size distribution.
2. The developed aqueous sol-gel synthesis method was successfully applied for the preparation of monophasic gallium containing garnets, namely $Gd_3Ga_5O_{12}$ (GGG), $Y_3Ga_5O_{12}$ (YGG) and $Lu_3Ga_5O_{12}$ (LuGG) at 1000 °C.
3. The Fe^{3+}, Ce^{3+}, Cr^{3+} doping and Ce^{3+}/Cr^{3+}-co-doping effects were investigated in GGG samples with different concentrations of dopants (0.25; 0.5; 1; 3; 5 and 10 mol%). The results obtained illustrated the great iron quenching effect on the possible lanthanide-ion emission in the garnet matrixes. The increase of cerium amount in garnet matrix has led to weaker emission, however, the decrease was not monotonous. In the case of GGG:Ce^{3+},Cr^{3+} phosphors the highest intensity of the emission at ~730 nm was observed for the samples containing 3 mol% of dopants (1.5 mol% Ce^{3+} and 1.5 mol% Cr^{3+}).
4. Sol-gel derived gallium garnets doped with Cr^{3+} were characterized by a broad PL band in the far-red region (700 – 760 nm). This emission meets the needs of photomorphogenesis in plants. The optical properties of phosphors were found to strongly depend on doping concentration and annealing temperature. The strongest PL of the samples was observed for the highest annealing temperatures, since in this case the most uniform and crystalline materials were obtained. The values of QE also increased for higher annealing temperatures.

5. The most promising materials for the photomorphogenetic LEDs, combining these materials with blue InGaN-based LEDs, could be based on YGG:Cr^{3+} and GGG:Cr^{3+}, since they exhibited the most suitable PL spectra and were characterized by the relatively high values of QE (55% and 30%, respectively).
6. The quantitative measurement of charge density and the change of cell parameter with lanthanide doping due to the difference in size revealed the inclusion of trivalent Ce^{3+} dopant on the host lattice. The 5*d* Ce orbitals participate in the chemical bonding and thus influence the charge density distributions reducing the band gap energy which may be the prominent key factor for the luminescence properties and the quantum efficiency of the non-linear optical material.
7. The real chemical composition of different Cr-doped garnet structure compounds was determined and compared for the first time by ICP-OES and EDX methods. These results were in a good agreement with the nominal composition, giving the same empirical formula of these synthesized garnets as theoretical formula of GSGG and YGG. In conclusion, the ICP-OES and two scanning electron microscopes gave comparable analysis results with a high accuracy and could be successfully used for the elemental analysis of such type of compounds.
8. Merwinite structure compound ($Ca_3Mg(SiO_4)_2$, CMSO) was successfully synthesized by novel aqueous sol-gel synthesis route and conventional well known solid-state reaction method. In the sol-gel processing the TRIS as complexing agent was successfully used for the first time to fabricate almost monophasic CMSO.
9. The attempts to synthesize $Ba_3Cu(SiO_4)_2$ and $Ca_3Mg_{1-x}Cu_x(SiO_4)_2$ compounds with structure similar to $M_3MgSi_2O_8$ by aqueous sol-gel, solid-state reaction and TSFZM methods were not successful. In all of the case, multiphasic reaction products have been obtained. The suggestions to improve synthetic approach to fabricate these compounds were provided.

LIST OF PUBLICTIONS

Articles in journals

1. A. Zabiliute, S. Butkute, A. Zukauskas, P. Vitta, A. Kareiva. Sol-gel synthesized far-red chromium-doped garnet phosphors for phosphor-conversion light-emitting diodes that meet the photomorphogenetic needs of plants. *Applied Optics*, 53 (2014) 907-914.
2. S. Butkute, A. Zabiliute, R. Skaudzius, P. Vitta, A. Beganskiene, A. Zukauskas, A. Kareiva. Sol-gel synthesis, characterization and study of substitution effects in different gallium-containing garnets. *Journal of Sol-Gel Science and Technology*, 76 (2015) 210-219.
3. T. K. Thirumalaisamy, S. Saravanakumar, S. Butkute, A. Kareiva, R. Saravanan. Structure and charge density of Ce doped gadolinium gallium garnet (GGG). *Journal of Materials Science: Materials in Electronics*. 27 (2016) 1920-1928.
4. S. Butkutė, T. Kübra, A. Žarkov, E. Kontrimavičiūtė, S. Tautkus, R. Ramanauskas, A. Kareiva. Investigation of distribution of metals in Cr^{3+}-doped $Y_3Ga_5O_{12}$ and $Gd_3Sc_2Ga_3O_{12}$ using ICP-OES and EDX. *Chemija*, 28 (2017) 154-159.
5. S. Butkute, E. Gaigalas, A. Beganskiene, F. Ivanauskas, R. Ramanauskas, A. Kareiva. Sol-gel combustion synthesis of high-quality chromium-doped mixed-metal garnets $Y_3Ga_5O_{12}$ and $Gd_3Sc_2Ga_3O_{12}$. *Journal of Alloys and Cmpounds*, 739 (2018) 504-509.

Articles not included in the thesis

1. A. Zarkov, A. Stanulis, J. Sakaliuniene, S. Butkute, B. Abakeviciene, T. Salkus, S. Tautkus, A. F. Orliukas, S. Tamulevicius, A. Kareiva. On the synthesis of yttria-stabilized zirconia: a comparative study. *Journal of Sol-Gel Science and Technology*, 76 (2015) 309-319.

Published contributions to academic conferences

1. S. Butkutė, A. Zabiliūtė. Sol-gel synthesis of garnet structure far-red phosphors for their possible application in greenhouses farming lighting. Nanochemistry and nanomaterials: international conference of young chemists, Palanga, Lithuania, 7 – 9 December (2012).
2. A. Zabiliūtė, S. Butkutė. Investigation of phosphors for far-red conversion light-emitting diodes. Open readings 2012: 55th scientific conference for young students of physics and natural sciences, Vilnius, Lithuania, 28 – 31 March (2012).
3. S. Butkutė, A. Beganskienė, A. Kareiva. Sol-gel combustion synthesis and characterization of differently doped $Gd_3Ga_5O_{12}$ garnets. Chemistry and chemical technology of inorganic materials, Kaunas, Lithuania (2013).
4. S. Butkutė, Ch. J. Fruhner, A. Adam, A. Beganskienė, A. Kareiva. Sol-gel combustion synthesis and characterization of Cr^{3+}-doped $Y_3Ga_5O_{12}$ garnets. MC11: 11th international conference on materials chemistry, UK, 8 – 11 July (2013).
5. S. Butkutė, A. Beganskienė, A. Kareiva. Characterization of $Gd_3Ga_5O_{12}$, $Gd_3Sc_2Ga_3O_{12}$, $Y_3Ga_5O_{12}$ and $Lu_3Ga_5O_{12}$ garnets doped with Cr^{3+} metal ions synthesized via sol-gel combustion method. EcoBalt 2013: 18th international scientific conference, Vilnius, Lithuania, 25 – 27 October.
6. A. Zabiliūtė, S. Butkutė, A. Žukauskas, P. Vitta, A. Kareiva. Far-red Cr-doped garnets for the control of photomorphogenesis in plants using phosphor-conversion LEDs. LEDIA 14: conference on LED and its industrial application, Pacifico Yokohama, Japan, 22 – 24 April (2014).
7. A. Zabiliūtė, S. Butkutė, A. Žukauskas, P. Vitta, A. Kareiva. Far-red Cr-doped garnet phosphors for phosphor-conversion LEDs that meet the photomorphogenetic needs of plants. Advanced materials and technologies, 16-th international conference-school, Palanga, Lithuania, 27 – 31 August (2014).

8. R. P. Petrauskas, S. Butkutė, A. Kareiva. Formation peculiarities of Cr^{3+}-doped $Y_3Ga_5O_{12}$. Chemistry and chemical technology 2015: international conference of Lithuanian Chemical Society, dedicated to Professor Vitas Daukšas on his 80th birth anniversary, Vilnius, Lithuania, 23 of January (2015).
9. H. Dapkus, A. Zabiliūtė-Karaliūnė, R. P. Petrauskas, S. Butkutė, A. Žukauskas, A. Kareiva. Cr^{3+} Legiruotas itrio ir galio granato fosforas skirtas konversijos fosfore puslaidininkiniams šviesos diodams (Cr^{3+} Doped Yttrium Gallium Garnet Phosphor for Phosphor-Conversion Light Emitting Diodes). 41-oji Lietuvos nacionalinė fizikos konferencija, Vilnius, birželio 17 – 19 d. (2015).
10. S. Butkutė, E. Giannini, Ch. Rüegg, A. Kareiva. Synthesis of merwinite structure compounds. Nanochemistry and nanomaterials 2015: 2nd international conference of chemist, Vilnius, Lithuania, 22 – 24 of October (2015).
11. S. Butkutė, K. Turan, A. Zarkov, R. Ramanauskas, A. Kareiva. On the Determination of Cr^{3+} Content in Doped $Y_3Ga_5O_{12}$:Cr and $Gd_3Sc_2Ga_3O_{12}$:Cr Garnets by ICP-OES and EDX Methods. Inovatyvioji ir tvarioji chemija, Puvočiai, Lithuania, 9 – 10 of December (2016).

ACKNOWLEDGEMENTS

First and foremost, I would like to thank my research supervisor, Prof. Habil. Dr. Aivaras Kareiva, without your assistance and dedicated involvement in every step throughout my studies, this thesis would have never been accomplished. I would like to thank you very much for your supervision, teaching and understanding over these past years.

I would like specially thank Prof. Dr. Christian Rüegg and Dr. Enrico Giannini for the supervision and given opportunity join your research groups and learning from you. It was fantastic to have the opportunity to work with you. Thanks to all people at Paul Scherrer Institut and University of Geneva the year during my internship was so pleasant.

I give my sincere gratitude to Dr. Jens-Erik Jørgensen's for the structural introduction to of Rietveld refinement using FullProf software and valuable comments of crystallography.

I am thankful to Akvilė Zabiliūtė-Karaliūnė for very productive and pleasing collaboration. I thank Dr. Aleksej Žarkov, Danas Sakalauskas, Dr. Martynas Misevičius, Olga Opuchovič for assistance with ICP-OES, SEM-EDX and TG-DSC measurements, as well Dr. Artūras Katelnikovas for assistance on measuring and shearing your knowledge on photo-luminescence properties, all of your help greatly improved this thesis.

Dear community, Institute of Chemistry from Faculty of Chemistry and Geosciences, I am indebted for your personal and professional unwavering support during the time I spent at the University. Getting through my studies required more than academic support and I have many, many people and friends to thank for their time, support, advices and ideas they shared with me. Thank you all for having to tolerate me over the past few years.

I want to express my appreciation to Research Council of Lithuania and also Sciex-NMSch for fellowships and providing the funding for the internships.

Most importantly, I am grateful to my beloved parents, Raimondas and my family for their love, support, understanding and patience. You have provided me with enough of support for this dissertation to become true.

REFERENCES

[1] M. Iranmanesh, J. Hulliger, Progress in Solid State Chemistry, 44 (2016), pp. 123-130.

[2] W. Araki, K. Takeda, Y. Arai, Journal of the European Ceramic Society, 36 (2016), pp. 4089-4094.

[3] N. Arjun, T.C.K. Yang, G.-T. Pan, Y.-L. Yang, A. Kareiva, Journal of the Taiwan Institute of Chemical Engineers, 69 (2016), pp. 151-155.

[4] D. Li, Y. Fan, Y. Ding, X. Wei, Y. Xiao, Catalysis Communications, 88 (2017), pp. 60-63.

[5] A. Zarkov, A. Stanulis, L. Mikoliunaite, A. Katelnikovas, V. Jasulaitiene, R. Ramanauskas, S. Tautkus, A. Kareiva, Ceram Int, 43 (2017), pp. 4280-4287.

[6] A. KAREIVA, MATERIALS SCIENCE (MEDŽIAGOTYRA), 17 (2011), pp. 428-437.

[7] N.G. Shimpi, S. Jain, N. Karmakar, A. Shah, D.C. Kothari, S. Mishra, Applied Surface Science, 390 (2016), pp. 17-24.

[8] X. Peng, K. Peng, J. Huang, J Alloy Compd, 691 (2017), pp. 165-170.

[9] O. Opuchovic, A. Kareiva, K. Mazeika, D. Baltrunas, J Magn Magn Mater, 422 (2017), pp. 425-433.

[10] E.L. Fertman, A.V. Fedorchenko, D.D. Khalyavin, A.N. Salak, A. Baran, V.A. Desnenko, O.V. Kotlyar, E. Čižmár, A. Feher, E.S. Syrkin, A.I. Vaisburd, N.M. Olekhnovich, A.V. Pushkarev, Y.V. Radyush, A. Stanulis, A. Kareiva, J Magn Magn Mater, 429 (2017), pp. 177-181.

[11] G.W. Scherer, C.J. Brinker, Sol-Gel Science, Sol-Gel Science, Academic Press, San Diego, 1990, pp. 1-908.

[12] A. Katelnikovas, J. Plewa, D. Dutczak, S. Moller, D. Enseling, H. Winkler, A. Kareiva, T. Justel, Opt Mater, 34 (2012), pp. 1195-1201.

[13] M. Mackevičius, F. Ivanauskas, A. Kareiva, D. Jasaitis, Journal of Mathematical Chemistry, 50 (2012), pp. 2291-2302.

[14] N. Dubnikova, E. Garskaite, R. Raudonis, A. Kareiva, Mater Chem Phys, 137 (2012), pp. 660-664.

[15] A. Katelnikovas, S. Sakirzanovas, D. Dutczak, J. Plewa, D. Enseling, H. Winkler, A. Kareiva, T. Justel, J Lumin, 136 (2013), pp. 17-25.

[16] R. Skaudžius, D. Enseling, M. Skapas, A. Selskis, E. Pomjakushina, T. Jüstel, A. Kareiva, C. Rüegg, Opt Mater, 60 (2016), pp. 467-473.

[17] R. Skaudzius, T. Juestel, A. Kareiva, Mater Chem Phys, 170 (2016), pp. 229-238.

[18] J.F.C. Carreira, N.B. Sedrine, T. Monteiro, L. Rino, J Lumin, 183 (2017), pp. 251-258.

[19] Y. Katayama, A. Hashimoto, J. Xu, J. Ueda, S. Tanabe, J Lumin, 183 (2017), pp. 355-359.

[20] G.W. Blasse, W. L.; Ter Vrugt, J. W.; Bril, A., Philips Research Reports, 23 (1968), pp. 189-200.

[21] S. Kareiva, V. Klimavicius, A. Momot, J. Kausteklis, A. Prichodko, L. Dagys, F. Ivanauskas, S. Sakirzanovas, V. Balevicius, A. Kareiva, Journal of Molecular Structure, 1119 (2016), pp. 1-11.

[22] J.B. A. Laurikėnas, A. Kareiva, Advances in Science and Technology, 98 (2017), pp. 70-74.

[23] R.H. Nobes, E.V. Akhmatskaya, V. Milman, B. Winkler, C.J. Pickard, Comp Mater Sci, 17 (2000), pp. 141-145.

[24] G. Menzer, XX. Die Kristallstruktur der Granate, Zeitschrift für Kristallographie - Crystalline Materials1929, pp. 300.

[25] S. Geller, Crystal chemistry of the garnets, Zeitschrift für Kristallographie - Crystalline Materials1967, pp. 1.

[26] Z.C. Huang, J. Feng, W. Pan, Solid State Sci, 14 (2012), pp. 1327-1332.

[27] J.E. Geusic, H.M. Marcos, L.G.V. Uitert, Applied Physics Letters, 4 (1964), pp. 182-184.

[28] S. Mathur, H. Shen, A. Leleckaite, A. Beganskiene, A. Kareiva, Mater Res Bull, 40 (2005), pp. 439-446.

[29] J.D. French, J. Zhao, M.P. Harmer, H.M. Chan, G.A. Miller, Journal of the American Ceramic Society, 77 (1994), pp. 2857-2865.

[30] S. Deng, J Mater Sci, 31 (1996), pp. 6077-6083.

[31] F.D. Patel, E.C. Honea, J. Speth, S.A. Payne, R. Hutcheson, R. Equall, IEEE Journal of Quantum Electronics, 37 (2001), pp. 135-144.

[32] E.S. Grew, A.J. Locock, S.J. Mills, I.O. Galuskina, E.V. Galuskin, U. Hålenius, Am Mineral, 98 (2013), pp. 785-811.

[33] F. Euler, J.A. Bruce, Acta Crystallogr, 19 (1965), pp. 971-&.

[34] E.S. Grew, J.H. Marsh, M.G. Yates, B. Lazic, T. Armbruster, A. Locock, S.W. Bell, M.D. Dyar, H.J. Bernhardt, O. Medenbach, Can Mineral, 48 (2010), pp. 1171-1193.

[35] A. Bosenick, M.T. Dove, C.A. Geiger, Physics and Chemistry of Minerals, 27 (2000), pp. 398-418.

[36] V.F. Kitaeva, E.V. Zharikov, I.L. Chistyi, physica status solidi (a), 92 (1985), pp. 475-488.

[37] E. Anticfidancev, J. Holsa, J.C. Krupa, M. Lemaitreblaise, P. Porcher, J Phys-Condens Mat, 4 (1992), pp. 8321-8330.

[38] H. Sawada, J Solid State Chem, 142 (1999), pp. 273-278.

[39] A. Nakatsuka, A. Yoshiasa, T. Yamanaka, Acta Crystallographica Section B, 55 (1999), pp. 266-272.

[40] A. Nakatsuka, A. Yoshiasa, S. Takeno, Acta Crystallographica Section B, 51 (1995), pp. 737-745.

[41] T. Armbruster, C.A. Geiger, G.A. Lager, Am Mineral, 77 (1992), pp. 512-521.

[42] A.M. Antyukhov, A.A. Sidorov, I.A. Ivanov, A.V. Antonov, Inorg. Mater. (Engl. Transl.); (United States), (1987), pp. Medium: X; Size: Pages: 632-634.

[43] J. Carda, G. Monros, V. Esteve, J.M. Amigo, J Solid State Chem, 108 (1994), pp. 24-28.

[44] H. Sawada, J Solid State Chem, 132 (1997), pp. 300-307.

[45] G. Ottonello, M. Bokreta, P.F. Sciuto, Am Mineral, 81 (1996), pp. 429-447.

[46] S. Naka, Y. Takeda, M. Sone, Y. Suwa, Chem Lett, 4 (1975), pp. 653-654.

[47] M. Kestigian, A.B. Smith, W.R. Bekebrede, J Appl Phys, 50 (1979), pp. 2161-2166.

[48] S. Geller, J.A. Cape, G.P. Espinosa, D.H. Leslie, Physical Review, 148 (1966), pp. 522-524.

[49] G.P. Espinosa, The Journal of Chemical Physics, 37 (1962), pp. 2344-2347.

[50] Y. Tanabe, S. Sugano, Journal of the Physical Society of Japan, 9 (1954), pp. 766-779.

[51] Y. Tanabe, S. Sugano, Journal of the Physical Society of Japan, 9 (1954), pp. 753-766.

[52] A.M. Srivastava, M.G. Brik, Opt Mater, 35 (2012), pp. 196-200.

[53] B. Wang, H. Lin, J. Xu, H. Chen, Y. Wang, ACS Applied Materials & Interfaces, 6 (2014), pp. 22905-22913.
[54] G. Racah, Physical Review, 63 (1943), pp. 367-382.
[55] G. Racah, Physical Review, 76 (1949), pp. 1352-1365.
[56] G. Blasse, B.C. Grabmaier, Luminescent materials, Springer-Verlag, Berlin ; New York, 1994.
[57] G. Blasse, Mater Chem Phys, 25 (1990), pp. 393-397.
[58] A.M. Srivastava, J Lumin, 129 (2009), pp. 1000-1002.
[59] F. Rodríguez, M. Moreno, The Journal of Chemical Physics, 84 (1986), pp. 692-697.
[60] A.M. Srivastava, Opt Mater, 31 (2009), pp. 881-885.
[61] B. Struve, G. Huber, Applied Physics B, 36 (1985), pp. 195-201.
[62] R. Skaudzius, J. Pinkas, R. Raudonis, A. Selskis, R. Juskenas, A. Kareiva, Mater Chem Phys, 135 (2012), pp. 479-485.
[63] L. Pavasaryte, A. Katelnikovas, V. Klimavicius, V. Balevicius, A. Krajnc, G. Mali, J. Plavec, A. Kareiva, Physical Chemistry Chemical Physics, 19 (2017), pp. 3729-3737.
[64] F.F.Y. Wang, Treatise on Materials Science & Technology, 2 (1973), pp. 279-384.
[65] C.D. Brandle, A.J. Valentino, J Cryst Growth, 12 (1972), pp. 3-8.
[66] C.D. Brandle, J Appl Phys, 49 (1978), pp. 1855-1858.
[67] F.P. Yu, D.R. Yuan, X.L. Duan, S.Y. Guo, X.Q. Wang, X.F. Cheng, L.M. Kong, J Alloy Compd, 465 (2008), pp. 567-570.
[68] Z. Chen, L. Yang, Y. Hang, X.Y. Wang, J Solid State Chem, 233 (2016), pp. 277-281.
[69] Z. Chen, L. Yang, Y. Hang, X. Wang, J Alloy Compd, 661 (2016), pp. 62-65.
[70] A.A. Setlur, The Electrochemical Society Interface, 18 (2009), pp. 32-36.
[71] A. Katelnikovas, A. Kareiva, Mater Lett, 62 (2008), pp. 1655-1658.
[72] A. Speghini, F. Piccinelli, M. Bettinelli, Opt Mater, 33 (2011), pp. 247-257.
[73] S. Yassaei, H. Aghili, A. Hosseinzadeh Firouzabadi, h. meshkani, 2017, 8 (2017), p. 5.

[74] D.O. Ignatyeva, P.O. Kapralov, G.A. Knyazev, S.K. Sekatskii, G. Dietler, M. Nur-E-Alam, M. Vasiliev, K. Alameh, V.I. Belotelov, JETP Letters, 104 (2016), pp. 679-684.

[75] J.-F. Wu, W.K. Pang, V.K. Peterson, L. Wei, X. Guo, ACS Applied Materials & Interfaces, 9 (2017), pp. 12461-12468.

[76] E. Popova, A. Shengelaya, D. Daraselia, D. Japaridze, S. Cherifi-Hertel, L. Bocher, A. Gloter, O. Stéphan, Y. Dumont, N. Keller, Applied Physics Letters, 110 (2017), p. 142404.

[77] F. Piccinelli, A. Speghini, G. Mariotto, L. Bovo, M. Bettinelli, Journal of Rare Earths, 27 (2009), pp. 555-559.

[78] R. Galindo, M. Llusar, M.A. Tena, G. Monrós, J.A. Badenes, Journal of the European Ceramic Society, 27 (2007), pp. 199-205.

[79] R. Galindo, J.A. Badenes, M. Llusar, M.A. Tena, G. Monrós, Mater Res Bull, 42 (2007), pp. 437-445.

[80] J. Xu, J. Ueda, K. Kuroishi, S. Tanabe, Scripta Materialia, 102 (2015), pp. 47-50.

[81] H. Cao, B. Lu, H. Xin, Q. Qiu, B. Yu, R. Ma, B. Lin, J. Chen, Science of Advanced Materials, 9 (2017), pp. 541-545.

[82] M. Daldosso, D. Falcomer, A. Speghini, P. Ghigna, M. Bettinelli, Opt Mater, 30 (2008), pp. 1162-1167.

[83] M. Bazzoni, M. Bettinelli, M. Daldosso, S. Enzo, F. Serra, A. Speghini, J Solid State Chem, 178 (2005), pp. 2301-2305.

[84] G. Wang, X. Li, Y. Geng, J Alloy Compd, 505 (2010), pp. 213-216.

[85] D. Hreniak, W. Stręk, P. Mazur, R. Pazik, M. Ząbkowska-Wacławek, Opt Mater, 26 (2004), pp. 117-121.

[86] D. Hreniak, W. Strek, P. Gluchowski, M. Bettinelli, A. Speghini, Appl Phys B-Lasers O, 91 (2008), pp. 89-93.

[87] V. Venkatramu, S.F.L. Luis, A.D. Lozano-Gorrin, L. Jyothi, P. Babu, U.R. Rodriguez-Mendoza, C.K. Jayasankar, J.E. Munoz-Santiuste, V. Lavin, Journal of Nanoscience and Nanotechnology, 12 (2012), pp. 4495-4501.

[88] O. Opuchovic, A. Beganskiene, A. Kareiva, J Alloy Compd, 647 (2015), pp. 189-197.

[89] F. Vetrone, J.-C. Boyer, J.A. Capobianco, A. Speghini, M. Bettinelli, The Journal of Physical Chemistry B, 107 (2003), pp. 10747-10752.

[90] Y.B. Chen, J. Wang, M.L. Gong, Q. Su, J.X. Shi, Chem Lett, 36 (2007), pp. 760-761.

[91] R. Mann, K. Laishram, N. Malhan, Journal of Rare Earths, 30 (2012), pp. 545-547.

[92] A. Katelnikovas, T. Bareika, P. Vitta, T. Justel, H. Winkler, A. Kareiva, A. Zukauskas, G. Tamulaitis, Opt Mater, 32 (2010), pp. 1261-1265.

[93] L. Pavasaryte, B.J. López, A. Kareiva, Mendeleev Commun, 25 (2015), pp. 384-385.

[94] G. Shirinyan, K.L. Ovanesyan, A. Eganyan, A.G. Petrosyan, C. Pedrini, C. Dujardin, I. Kamenskikh, N. Guerassimova, Nuclear Instruments and Methods in Physics Research Section A: Accelerators, Spectrometers, Detectors and Associated Equipment, 537 (2005), pp. 134-138.

[95] C.D. Brandle, R.L. Barns, J Cryst Growth, 26 (1974), pp. 169-170.

[96] S. Guo, D. Yuan, X. Cheng, H. Yu, S. Sun, F. Yu, H. Zhang, H. Xia, X. Tao, J Cryst Growth, 310 (2008), pp. 4685-4688.

[97] Z. Chen, L. Yang, X. Wang, J. Wang, Y. Hang, Mater Lett, 161 (2015), pp. 93-95.

[98] Z. Chen, L. Yang, Y. Hang, X. Wang, Opt Mater, 47 (2015), pp. 39-43.

[99] Z. Chen, L. yang, X. Wang, J. Wang, Y. Hang, Opt Mater, 46 (2015), pp. 12-15.

[100] L. Tian, S. Wang, K. Wu, B. Wang, H. Yu, H. Zhang, H. Cai, H. Huang, Opt Mater, 36 (2013), pp. 521-528.

[101] X. Xu, T.-C. Chong, G. Zhang, M. Li, L.H. Soo, W. Xu, B. Freeman, J Cryst Growth, 250 (2003), pp. 62-66.

[102] S. Kurosawa, A. Suzuki, A. Yamaji, K. Kamada, J. Pejchal, Y. Ohashi, Y. Yokota, V.I. Chani, A. Yoshikawa, J Cryst Growth, 452 (2016), pp. 95-100.

[103] K. Mazur, J. Sarnecki, J. Borysiuk, W. Wierzchowski, K. Wieteska, A. Turos, Thin Solid Films, 519 (2011), pp. 2111-2115.

[104] V. Gorbenko, Y. Zorenko, T. Zorenko, T. Voznyak, K. Paprocki, K. Fabisiak, A. Fedorov, P. Bilski, A. Twardak, G. Zhusupkalieva, Radiat Meas, 90 (2016), pp. 183-187.

[105] W.R. Eppler, M.H. Kryder, Journal of Physics and Chemistry of Solids, 56 (1995), pp. 1479-1490.

[106] M. Yamaga, A. Marshall, K.P. O'Donnell, B. Henderson, Y. Miyazaki, J Lumin, 39 (1988), pp. 335-341.

[107] M. Pang, J. Lin, J Cryst Growth, 284 (2005), pp. 262-269.

[108] S. Yao, R. Kamakura, S. Murai, K. Fujita, K. Tanaka, J Magn Magn Mater, 422 (2017), pp. 100-104.

[109] E. Garskaite, M. Lindgren, M.-A. Einarsrud, T. Grande, Journal of the European Ceramic Society, 30 (2010), pp. 1707-1715.

[110] R. Praveena, K. Balasubrahmanyam, L. Jyothi, G. Venkataiah, C. Basavapoornima, C.K. Jayasankar, J Lumin, 170, Part 1 (2016), pp. 262-270.

[111] M.G. Brik, A.M. Srivastava, N.M. Avram, Opt Mater, 33 (2011), pp. 1671-1676.

[112] A. Katelnikovas, J.M. Ogieglo, H. Winkler, A. Kareiva, T. Justel, J Sol-Gel Sci Techn, 59 (2011), pp. 311-314.

[113] A. Katelnikovas, H. Winkler, A. Kareiva, T. Justel, Opt Mater, 33 (2011), pp. 992-995.

[114] A. Katelnikovas, H. Bettentrup, D. Dutczak, A. Kareiva, T. Justel, J Lumin, 131 (2011), pp. 2754-2761.

[115] R. Skaudzius, A. Katelnikovas, D. Enseling, A. Kareiva, T. Justel, J Lumin, 147 (2014), pp. 290-294.

[116] Q.-f. Lu, J. Li, D.-J. Wang, ECS Solid State Letters, 1 (2012), pp. R24-R26.

[117] G.B. Nair, S.J. Dhoble, Luminescence, 30 (2015), pp. 1167-1175.

[118] Y. Yonesaki, T. Takei, N. Kumada, N. Kinomura, J Solid State Chem, 182 (2009), pp. 547-554.

[119] P.B. Moore, T. Araki, Am Mineral, 57 (1972), pp. 1355-&.

[120] C.H. Park, S.T. Hong, D.A. Keszler, J Solid State Chem, 182 (2009), pp. 496-501.

[121] Y. Yonesaki, Q. Dong, N.S.B. Mohamad, A. Miura, T. Takei, J. Yamanaka, N. Kumada, N. Kinomura, J Alloy Compd, 509 (2011), pp. 8738-8741.

[122] Y. Yonesaki, J Solid State Chem, 201 (2013), pp. 324-329.

[123] Y. Yonezaki, Powder Diffraction, 30 (2015), pp. 40-51.

[124] C.-H. Park, T.-H. Kim, Y. Yonesaki, N. Kumada, J Solid State Chem, 184 (2011), pp. 1566-1570.

[125] T.L. Barry, J Electrochem Soc, 115 (1968), pp. 733-&.

[126] T.L. Barry, J Electrochem Soc, 115 (1968), pp. 1181-1184.

[127] Y. Yonesaki, T. Takei, N. Kumada, N. Kinomura, J Lumin, 128 (2008), pp. 1507-1514.

[128] Y.H. Lin, Z.L. Tang, Z.T. Zhang, C.W. Nan, J Alloy Compd, 348 (2003), pp. 76-79.

[129] A.A.S. Alvani, F. Moztarzadeh, A.A. Sarabi, J Lumin, 114 (2005), pp. 131-136.

[130] H.-K. Jung, K.S. Seo, Opt Mater, 28 (2006), pp. 602-605.

[131] W. Pan, G. Ning, Sensors and Actuators A: Physical, 139 (2007), pp. 318-322.

[132] W. Pan, G.-L. Ning, J.-H. Wang, Y. Lin, Chinese J Chem, 25 (2007), pp. 605-608.

[133] L. Ma, D.-j. Wang, Z.-y. Mao, Q.-f. Lu, Z.-h. Yuan, Applied Physics Letters, 93 (2008), p. 144101.

[134] L. Ma, D.-J. Wang, H.-m. Zhang, T.-c. Gu, Z.-h. Yuan, Electrochemical and Solid-State Letters, 11 (2008), pp. E1-E4.

[135] T. Aitasalo, A. Hietikko, J. Holsa, M. Lastusaari, J. Niittykoski, T. Piispanen, Z Kristallogr, (2007), pp. 461-466.

[136] Y. Yonesaki, C. Matsuda, J Solid State Chem, 184 (2011), pp. 3247-3252.

[137] J.K. Han, A. Piqutte, M.E. Hannah, G.A. Hirata, J.B. Talbot, K.C. Mishra, J. McKittrick, J Lumin, 148 (2014), pp. 1-5.

[138] G. Blasse, W.L. Wanmaker, J.W. ter Vrugt, J Electrochem Soc, 115 (1968), p. 673.

[139] S. Okamoto, Y. Nanba, T. Honma, H. Yamamoto, Electrochemical and Solid-State Letters, 11 (2008), pp. J47-J49.

[140] K.Y. Jung, K.H. Han, H.-K. Jung, J Electrochem Soc, 156 (2009), pp. J129-J133.

[141] P. Zhang, X. Chen, Z. Zhang, M. Fei, L. Chen, J Lumin, 169, Part B (2016), pp. 733-738.

[142] Y. Yonezaki, S. Takei, K. Ogawa, J Lumin, 188 (2017), pp. 12-17.

[143] J.S. Kim, P.E. Jeon, J.C. Choi, H.L. Park, S.I. Mho, G.C. Kim, Applied Physics Letters, 84 (2004), pp. 2931-2933.

[144] Z. Mao, J. Chen, J. Li, D. Wang, Chemical Engineering Journal, 284 (2016), pp. 1003-1007.

[145] Q.-f. Lu, J. Li, D.-j. Wang, Current Applied Physics, 13 (2013), pp. 1506-1511.

[146] A. Birkel, N.A. DeCino, C. Cozzan, A.A. Mikhailovsky, B.-C. Hong, R. Seshadri, Solid State Sci, 48 (2015), pp. 82-89.

[147] Y. Chen, B. Zhou, Q. Sun, Y. Wang, B. Yan, Superlattices and Microstructures, 100 (2016), pp. 158-167.

[148] Y. Yonesaki, T. Takei, N. Kumada, N. Kinomura, J Solid State Chem, 183 (2010), pp. 1303-1308.

[149] Y. Lin, Z. Zhang, Z. Tang, X. Wang, J. Zhang, Z. Zheng, Journal of the European Ceramic Society, 21 (2001), pp. 683-685.

[150] Y. Gong, Y. Wang, X. Xu, Y. Li, S. Xin, L. Shi, Opt Mater, 33 (2011), pp. 1781-1785.

[151] B. Mróz, H. Kiefte, M.J. Clouter, J.A. Tuszyński, Phys Rev B, 43 (1991), pp. 641-648.

[152] J. Díaz-Hernández, J.L. Mañes, M.J. Tello, A. López-Echarri, T. Breczewski, I. Ruiz-Larrea, Phys Rev B, 53 (1996), pp. 14097-14102.

[153] K. Karmakar, M. Skoulatos, G. Prando, B. Roessli, U. Stuhr, F. Hammerath, C. Rüegg, S. Singh, Phys Rev Lett, 118 (2017), p. 107201.

[154] B. Huang, G. Clark, E. Navarro-Moratalla, D.R. Klein, R. Cheng, K.L. Seyler, D. Zhong, E. Schmidgall, M.A. McGuire, D.H. Cobden, W. Yao, D. Xiao, P. Jarillo-Herrero, X. Xu, Nature, 546 (2017), pp. 270-273.

[155] K. Karmakar, A. Singh, S. Singh, A. Poole, C. Rüegg, Crystal Growth & Design, 14 (2014), pp. 1184-1192.

[156] T. Giamarchi, C. Ruegg, O. Tchernyshyov, Nat Phys, 4 (2008), pp. 198-204.

[157] N. van Well, P. Puphal, B. Wehinger, M. Kubus, J. Schefer, C. Rüegg, F. Ritter, C. Krellner, W. Assmus, Crystal Growth & Design, 16 (2016), pp. 3416-3424.

[158] P. Puphal, D. Sheptyakov, N. van Well, L. Postulka, I. Heinmaa, F. Ritter, W. Assmus, B. Wolf, M. Lang, H.O. Jeschke, R. Valentí, R. Stern, C. Rüegg, C. Krellner, Phys Rev B, 93 (2016), p. 174121.

[159] W. Ahn, J.H. Park, Y.J. Kim, Ceram Int, 41, Supplement 1 (2015), pp. S744-S749.

[160] L. Wang, Q. Lu, J. Li, C. Lin, L. Cao, D. Wang, Journal of Rare Earths, 31 (2013), pp. 541-545.

[161] J.C. de Mello, H.F. Wittmann, R.H. Friend, Advanced Materials, 9 (1997), pp. 230-232.

[162] V. Petříček, M. Dušek, L. Palatinus, Crystallographic Computing System JANA2006: General features, Zeitschrift für Kristallographie - Crystalline Materials2014, pp. 345.

[163] N. Dubnikova, E. Garskaite, J. Pinkas, P. Bezdicka, A. Beganskiene, A. Kareiva, J Sol-Gel Sci Techn, 55 (2010), pp. 213-219.

[164] G. Walker, T.J. Glynn, J Lumin, 54 (1992), pp. 131-137.

[165] R. Heitz, P. Maxim, L. Eckey, P. Thurian, A. Hoffmann, I. Broser, K. Pressel, B.K. Meyer, Phys Rev B, 55 (1997), pp. 4382-4387.

[166] L.P. Sosman, T. Abritta, M.R. Amaral, N. Cella, H. Vargas, Solid State Commun, 105 (1998), pp. 135-138.

[167] Z. Bryknar, Z. Potůček, H.J. Schulz, Radiation Effects and Defects in Solids, 149 (1999), pp. 51-54.

[168] V. Bondarenko, N. Kazuchits, S. Volchek, L. Dolgyi, V. Petrovich, V. Yakovtseva, P. Gaiduk, M. Balucani, G. Lamedica, A. Ferrari, physica status solidi (a), 197 (2003), pp. 441-445.

[169] T. Arakawa, M. Akamine, Sensors and Actuators B: Chemical, 91 (2003), pp. 252-255.

[170] K.-i. Machida, J Ceram Soc Jpn, 111 (2003), pp. 162-167.

[171] A. Katelnikovas, J. Jurkevicius, K. Kazlauskas, P. Vitta, T. Justel, A. Kareiva, A. Zukauskas, G. Tamulaitis, J Alloy Compd, 509 (2011), pp. 6247-6251.

[172] A. Katelnikovas, T. Justel, D. Uhlich, J.E. Jorgensen, S. Sakirzanovas, A. Kareiva, Chem Eng Commun, 195 (2008), pp. 758-769.

[173] L. Kostyk, A. Luchechko, Y. Zakharko, O. Tsvetkova, B. Kuklinski, J Lumin, 129 (2009), pp. 312-316.

[174] Vitalij K. Pecharsky, P.Y. Zavalij, Fundamentals of Diffraction, Fundamentals of Powder Diffraction and Structural Characterization of Materials, Springer US, Boston, MA, 2009, pp. 133-149.

[175] H. Rietveld, Journal of Applied Crystallography, 2 (1969), pp. 65-71.

[176] D.M. Collins, Nature, 298 (1982), pp. 49-51.

[177] T.J.B. Holland, S.A.T. Redfern, Mineralogical Magazine, 61 (1997), pp. 65-77.

[178] D.L. Wood, J. Tauc, Phys Rev B, 5 (1972), pp. 3144-3151.

[179] H. Orucu, G. Ozen, J. Collins, B. Di Bartolo, Opt Mater, 31 (2009), pp. 1065-1070.

[180] B. Struve, G. Huber, V.V. Laptev, I.A. Shcherbakov, E.V. Zharikov, Applied Physics B, 30 (1983), pp. 117-120.

[181] S. Mahlik, B. Kuklinski, M. Grinberg, L. Kostyk, O. Tsvetkova, Acta Phys Pol A, 117 (2010), pp. 117-121.

[182] Z. Mazurak, Opt Mater, 3 (1994), pp. 89-93.

[183] C. Unluer, A. Al-Tabbaa, J Therm Anal Calorim, 115 (2014), pp. 595-607.

[184] M.K. Van Bael, A. Kareiva, G. Vanhoyland, J. D'Haen, M. D'Olieslaeger, D. Franco, C. Quaeyhaegens, J. Yperman, J. Mullens, L.C. Van Poucke, Physica C: Superconductivity, 307 (1998), pp. 209-220.

[185] A. Kareiva, M. Karppinen, L. Niinisto, J Mater Chem, 4 (1994), pp. 1267-1270.

[186] S. Mathur, H. Shen, N. Lecerf, M.H. Jilavi, V. Cauniene, J.-E. Jørgensen, A. Kareiva, J Sol-Gel Sci Techn, 24 (2002), pp. 57-68.

[187] D.S. Todorovsky, M.M. Getsova, M.A. Vasileva, J Mater Sci, 37 (2002), pp. 4029-4039.

[188] M.A. de la Rubia, J.J. Reinosa, P. Leret, J.J. Romero, J. de Frutos, J.F. Fernández, Journal of the European Ceramic Society, 32 (2012), pp. 71-76.

[189] M.E. Huntelaar, E.H.P. Cordfunke, Journal of Nuclear Materials, 201 (1993), pp. 250-253.

[190] V.M. Ust'yantsev, L.P. Sudakova, A.F. Bessonov, Russian Journal of Inorganic Chemistry, 11 (1966), pp. 1177-1182.

[191] P. Eskola, Am J Sci, Series 5 Vol. 4 (1922), pp. 331-375.

[192] A. Kato, Y. Suyama, J Therm Anal Calorim, 7 (1975), pp. 149-158.